

AFIT/DS/ENP/97-07

Experimental Investigation of Nonlinear Dynamics in Single Mode Semiconductor  
Laser Diodes with Phase Conjugate Feedback

DISSERTATION  
Gordon Thomas Hengst  
Major

AFIT/DS/ENP/97-07

Approved for public release; distribution unlimited

19970924 046

AFIT/DS/ENP/97-07

Experimental Investigation of Nonlinear Dynamics in Single Mode  
Semiconductor Laser Diodes with Phase Conjugate Feedback

DISSERTATION

Presented to the Faculty of the School of Engineering  
of the Air Force Institute of Technology

Air University

In Partial Fulfillment of the  
Requirements for the Degree of  
Doctor of Philosophy

Gordon Thomas Hengst, B.S., M.S.

Major

August, 1997

Approved for public release; distribution unlimited

AFIT/DS/ENP/97-07

Experimental Investigation of Nonlinear Dynamics in Single Mode  
Semiconductor Laser Diodes with Phase Conjugate Feedback

Gordon Thomas Hengst, B.S., M.S.

Major

Approved:

<u>Don B. Roh</u>	<u>Aug 11, 97</u>
<u>Craig C. Lytt</u>	<u>8/11/97</u>
<u>Will P. Boh</u>	<u>Aug 11, 97</u>
<u>J. Griselde</u>	<u>8/11/97</u>
<u>Christophe D. Hall</u>	<u>Aug 11, 97</u>



Robert A. Calico, Jr.

Dean

## *Acknowledgements*

The study of nonlinear dynamics in a laser diode with phase conjugate feedback can truly be “*chaotic*” at times. As with any experimental project, the outcome is always uncertain but the success of this research was a product of team work. Although I cannot possibly mention everyone involved, a few people deserve special recognition for their contributions to this program. I wish to thank my committee for their invaluable insight and guidance around the technical hurdles that real experiments can throw at you. I especially thank Dr Roh, my advisor, for challenging me on the subject of chaos and nonlinear dynamics; through his questioning I learned more about chaotic systems than a text book could offer. I also thank Dr Gavrielides, from the Air Force Research Laboratory, who developed the two computer models used extensively in this research. His technical guidance, extensive knowledge of nonlinear systems and experience with chaotic systems was invaluable. I also want to thank Jim Reynolds, Rick Patton, and the rest of the Engineering Physics Department technician staff who reliably were able to find that *one* piece of equipment I always needed. A special recognition goes to my wife, Brigid, who had to endure yet a second school assignment to AFIT which absorbed every hour of my day. I also thank my fellow students for contributing to the boost in moral when the battle with the lab seemed to be lost. And last, but not least, I wish to thank my stepfather, William H. Shook Jr., who always inspired me throughout my youth and adulthood to explore the realm of physics.

Gordon Thomas Hengst

## *Table of Contents*

	Page
Acknowledgements . . . . .	iii
List of Figures . . . . .	vi
List of Tables . . . . .	xi
List of Symbols . . . . .	xii
Abstract . . . . .	xiv
I. Introduction . . . . .	1
1.1 Overview . . . . .	1
1.2 Introduction to Chaos . . . . .	2
1.3 Phase Conjugating Mirrors (PCM) . . . . .	13
II. Theory of Nonlinear Dynamics for Phase Conjugate Feedback in Laser Diodes . . . . .	18
2.1 Development of Rate Equations Without Feedback . . . . .	20
2.2 Rate Equations with Phase Conjugate Feedback . . . . .	27
2.3 Regions of Laser Operation . . . . .	28
III. Mathematical Analysis . . . . .	31
3.1 Scaling . . . . .	31
3.2 Steady State Solutions . . . . .	32
3.3 Steady State Stability . . . . .	35
IV. Computer Modeling of the Phase Conjugate Feedback . . . . .	40
4.1 Bifurcation Model . . . . .	40
4.2 Spectrum Model . . . . .	44

	Page
V. Experimental Descriptions and Results . . . . .	51
5.1 Solitary Laser Characterization . . . . .	51
5.2 Self-Pumped Phase Conjugate Feedback . . . . .	54
5.2.1 Single Mode Operation with Phase Conjugate Feed- back . . . . .	61
5.2.2 CAT Phase Conjugate Mirror Time Response . .	63
5.2.3 External Cavity Length and Frequency Dependency	67
5.2.4 External Cavity Resonance and Frequency Locking	69
5.2.5 Verification of the Conjugate Signal . . . . .	72
5.3 Double Phase Conjugate Mirror Measurements . . . . .	81
VI. Experimental and Modeling Results . . . . .	86
6.1 Gain Saturation Improvement . . . . .	86
6.2 External Cavity . . . . .	88
6.3 Relaxation Oscillation and Locking Ratio . . . . .	90
6.4 Feedback Resonance . . . . .	96
6.5 Bifurcation Diagram . . . . .	98
VII. Conclusions and Recommendations . . . . .	102
Appendix A. MathCad Templates . . . . .	105
Appendix B. LKCONBI2.C Source Code . . . . .	110
Appendix C. LKCON2.C Source Code . . . . .	123
Bibliography . . . . .	138
Vita . . . . .	141

## List of Figures

Figure	Page
1. A typical bifurcation diagram showing the sudden abrupt changes in the behavior of a fictitious system as the feedback is increased. The shaded area denotes the area of chaotic behavior. The output axis can be any measurable change in the laser diode system such as output power, bias voltage, bias current, etc. The letters correspond to spectrums shown in Figure 2 . . . . .	4
2. Frequency spectrum of the fictitious system shown in Figure 1. (A) Stable, solitary output at $\omega_1$ , (B) New stable lasing frequency $\omega_2$ , (C) Periodic output where the relaxation frequency has undamped and period doubling, (D) Chaotic output after an infinite number of period doublings. . . . .	5
3. Phase plots of trajectories of a simple harmonic damped system which has a complex conjugate pair of Lyapunov exponents. The fixed point for this system is shown by a '+' and the direction of increasing time is shown by the arrow. (a) periodic behavior for a real part = 0, (b) attracting behavior towards the fixed point when the real part < 0, and (c) the trajectory repels away from the fixed point out to the limit cycle or spirals into the limit cycle when the real part > 0 . . . . .	8
4. Simple two-level laser system showing the pumping $R_p$ to level 2, spontaneous emission rate, $A_{21}$ , stimulated emission, $B_{21}$ , and stimulated absorption, $B_{12}$ . . . . .	10
5. Graphical depiction of the time evolution of the Nd-YAG two-level laser system showing the spiraling convergence to a limit cycle around fixed point #2. Initial conditions are $BP/A_{21} = 0.1$ and $B\Delta N/\gamma = 1$ . . . . .	12
6. The reflected beam of a phase conjugate mirror retraces its original path, self-correcting any distortions caused by optics. The lower trace shows a beam reflected from a normal dielectric mirror which further distorts the wave-front after being reflected. . . . .	14
7. Two different methods of establishing a phase conjugating mirror used in this research. (a) Self-pumped CAT geometry. (b) Double-phase conjugating mirror (DPCM). . . . .	15

Figure	Page
8. Diagram of the optical fields in the laser diode and an external phase conjugating mirror. . . . .	19
9. (a) Graphical solution of Eq. (57) showing the stable ( $\times$ ) and unstable ( $\circ$ ) solutions. (b) For a given solution of $(\eta, \hat{\omega})$ , the fold bifurcation lines can be found as a function of feedback, $\eta$ . PL is the phase locked region and the area below the fold bifurcation line represents unstable periodic solutions. . . . .	34
10. Plots of Eqs. (69) and (70) showing the resonance in $\eta_H$ and $\Omega_H$ for typical experimental external cavity lengths. . . . .	39
11. Bifurcation diagrams created using the LKCONBIF.C model. (a) Short external cavity with $\tau = 16$ , ext_length = 1.0 cm, (b) Long external cavity with $\tau = 640$ , ext_length = 40 cm. . . . .	43
12. (a) Bifurcation diagram from Figure 11b. (b) RF spectrum of the bifurcation diagram in using the LKCON2.C model with a feedback rate of $\eta_{inject} = 0.0065$ . The fundamental $\nu_{ext}$ is at 180 MHz, with spacings at 185 and 375 MHz. (c) FM spectrum for the same feedback rate. $\nu_R$ appears at $\pm 4.7$ GHz along with modulations from the RF. . . . .	46
13. Model predictions (squares) of the external cavity frequency spacing as a function of the external cavity length. The theoretical $c/(2L)$ line is provided as a reference. . . . .	48
14. Model predictions for the changes in the relaxation oscillation frequency as a function of external cavity length. . . . .	49
15. Model predictions of the locking ratio between the relaxation oscillation frequency and external cavity frequency. . . . .	50
16. Experimental setups to measure the solitary laser parameters. . . . .	52
17. Solitary laser light-curve data. The lasing threshold is found to be about 15 mA with a slope of .93 mW/mA. . . . .	53
18. Optical spectrum of the solitary laser at bias current 30 mA. The center wavelength is 804.4 nm with small peaks surrounding the main lobe. These small peaks are easily excited with feedback causing the laser to operate multi-mode. Operating the laser with a bias current $> 40$ mA ensures a single mode output. . . . .	55

Figure	Page
19. Optical spectrum of the solitary laser at bias current 40 mA. . . . .	56
20. Optical spectrum of the solitary laser at bias current 50 mA. . . . .	57
21. Fabry-Perot output of the solitary laser biased at 30 mA. The linewidth of the laser line is measured to be 130 MHz. The center lobe of the scan is rough due to low frequency noise in the power supply and temperature instabilities in the T-E cooler. The smaller peaks at -1.5 GHz and -2.2 GHz are other frequencies that exist at low bias currents.	58
22. Diagram of the setup used in the CAT experiments . . . . .	59
23. OMA scans during the onset of chaos. (a) The laser is biased at 30 mA and the feedback was set so that the relaxation and external cavity frequencies were undamped. Multiple laser modes have started to lase due to the feedback. (b) The laser is biased at 40 mA and the feedback is increased to place the laser near the chaotic state. Even at this strong feedback, the laser remains single mode. . . . .	62
24. RF spectra of the feedback signal from a normal mirror (above) and the laser output (below). Both signals contain the same frequency information indicating that there is no filtering being done by the normal mirror. The speed of a normal mirror can be considered instantaneous.	65
25. The correlation between the two PIN diodes sampling the laser output and normal feedback signal shows a peak at a delay of 11 ns. This delay corresponds exactly to the optical and electrical path differences between the two detectors. . . . .	66
26. RF spectra of the feedback signal from the CAT PCM mirror and the laser output. Both signals contain the same frequency information indicating that there is no filtering being done by the CAT mirror. .	68
27. Correlation function of the CAT PCM signal with the direct laser output . . . . .	69
28. Plot of experimentally measured external cavity frequency using a degenerate CAT PCM. The solid line represents the theoretical value of $c/(2L_{ext})$ for a cavity bounded by a degenerate phase conjugate mirror.	70
29. Plot of experimentally measured external cavity frequencies versus cavity length using a normal mirror. The solid line represents the theoretical value of $c/(2L_{ext})$ for an external cavity with a normal mirror.	71

Figure	Page
30. Experimental setup used to capture the feedback resonance peaks and frequency locking from the CAT PCM. The Klinger translation stage was used to extend the cavity in a span of 8 cm in 1 mm increments.	73
31. Experimental data showing the frequency locking (top curve, right axis) of the external cavity and relaxation frequencies from the CAT PCM. The bottom curve shows the resonance of the feedback power at the first Hopf bifurcation. . . . .	74
32. Experimental data showing the frequency locking (top curve, right axis) of the external cavity and relaxation frequencies from the CAT PCM. The bottom curve shows the changes in the relaxation oscillation as the external cavity is varied. The solitary relaxation frequency of 3.7 GHz falls halfway between the maximum and minimum values. .	75
33. Profile of the beam entering the BaTiO <sub>3</sub> crystal. . . . .	76
34. Phase conjugate intensity profiles captured using BeamCode as chaos develops. (a) Relaxation oscillations are undamped, (b) external cavity frequency undamped, (c) several external cavity frequencies undamped, (d) full chaos behavior. . . . .	77
35. Normal mirror profiles captured using BeamCode as chaos develops. (a) Relaxation oscillations are undamped, (b) external cavity frequency has undamped, (c) full chaos.. . . .	79
36. Phase conjugate signal (a) and normal signal (b) with a phase distorting medium placed in the beam entering the BaTiO <sub>3</sub> crystal. In both cases the relaxation and external cavity frequencies have undamped.	80
37. Experimental configuration used in the double phase conjugate mirror experiments. . . . .	82
38. Plot of experimentally measured external cavity frequencies versus cavity length using a DPCM mirror. The solid line represents the theoretical mode spacing value of $c/L_{ring}$ for a degenerate PCM. . . . .	83
39. RF spectra of the feedback signal from the DPCM mirror and the laser output. Both signals contain the same frequency information indicating that there is no filtering being done by the DPCM mirror	84

Figure	Page
40. Comparison between the model (open diamond) and experimental (dotted line) data for the external cavity frequency, $\nu_{ext}$ , as a function of the external cavity length, $L_{ext}$ . . . . .	88
41. Comparison between experimental and LKCON2.C model data for the changes in the relaxation oscillation frequency. . . . .	91
42. Diagram of a F-P display showing an 8 GHz FSR between adjacent F-P modes and two frequencies. From the F-P display it is not possible to determine if the two frequencies are at 3.72 GHz or 4.28 GHz. . .	92
43. Comparison between experimental and model data for the changes in the relaxation oscillation frequency using the increased value of $\alpha$ in the model and reinterpretation of the experimentally measured $\nu_R$ . .	94
44. Comparison between experimental (dotted line) and model (open diamond) data for the locking ratio. . . . .	95
45. Comparison between the experimental cavity resonance data taken with the Klinger translation stage and Eq. (69). . . . .	97
46. Plot of experimental cavity resonance data taken with the manual micrometer translation stage. . . . .	99
47. Bifurcation map created by the LKCONBI2.C model for $L_{ext} = 20$ cm overlaid with points from the experimentally observed bifurcations (closed diamonds). The experimental bifurcation points were obtained by watching the RF or F-P spectra and noting the conjugate feedback power as frequencies emerged. . . . .	100

*List of Tables*

Table		Page
1.	Summary of the behavior of trajectories due to different eigenvalues.	7
2.	Examples of typical parameters for a Nd-YAG laser system. . . . .	11
3.	Listing of the two different phase conjugate mirrors and their controlling parameters used in the research. . . . .	17
4.	The absorption coefficients ( $cm^{-1}$ ) in an externally pumped FP-resonator consisting of an active medium confined between mirrors (27:98). $\chi''_o$ and $\chi''_p$ are the two elements of the total scalar susceptibility in an isotropic material due to unpumped background material losses and losses due to external pumping, respectively. . . . .	23
5.	With increasing feedback, the laser output can be categorized into five different levels of chaotic development. . . . .	29
6.	Input parameters contained in a separate ASCii file for the LKCONBI2 model. . . . .	41
7.	Summary of the solitary laser characteristics. . . . .	54
8.	Identification of key bifurcation events shown in Figure 47. . . . .	101

## *List of Symbols*

Symbol	Page
$P$ Number of photons . . . . .	9
$\Delta N$ Population difference between lasing levels 1 and 2 . . . . .	9
$B_{12}$ Stimulated emission coefficient . . . . .	9
$\bar{N}$ Unsaturated population of level 2 without stimulated emission . . . . .	9
$R_{PCM}$ Reflectivity of the phase conjugate mirror . . . . .	16
$\vec{E}^*(t)$ Complex conjugate amplitude of the e-field leaving the PCM . . . . .	16
$\omega$ Lasing angular optical frequency of the solitary laser . . . . .	16
$\phi_{PCM}$ Phase shift of the conjugate beam relative to the probe beam . . . . .	16
$N(t)$ Electron-hole pair number . . . . .	20
$\vec{E}(t)$ Optical field . . . . .	20
$D$ Diffusion coefficient of the laser diode medium . . . . .	20
$d$ Length of laser diode active region . . . . .	20
$J$ Applied pumping current density . . . . .	20
$\mathcal{R}(N)$ Lump sum rate of all loss mechanisms of electron-hole pairs . . . . .	20
$\tau_N$ Electron-hole carrier lifetime . . . . .	20
$R_{st}(N, P)$ Stimulated radiation rate . . . . .	20
$v_g$ Group velocity of the longitudinal mode inside the laser cavity . . . . .	21
$g(N)$ Electron-hole dependent gain coefficient . . . . .	21
$g(N_{th})$ Threshold gain coefficient . . . . .	21
$N_{th}$ Number of electron-hole pairs at threshold . . . . .	21
$g_{opt}$ Optical gain of the laser cavity . . . . .	21
$\Gamma$ Fraction of photons that interact in the gain region of the laser . . . . .	21
$\Gamma_o$ Total loss rate of photons in the laser cavity . . . . .	22
$\tau_p^{-1}$ Inverse photon lifetime . . . . .	22
$\xi$ Differential gain rate . . . . .	22

Symbol	Page
$p$	Ratio of carriers created by the pumping current to carriers lost . . . 22
$\mathcal{G}$	Round trip amplitude gain in the laser cavity . . . . . 23
$n(N, \omega)$	Carrier and frequency dependent refractive index of the laser gain medium . . . . . 23
$n_g$	Group refractive index for the longitudinal mode of the laser cavity 24
$\mathcal{G}_1$	Frequency independent round trip amplitude gain . . . . . 24
$\mathcal{G}_\omega$	Frequency dependent round trip amplitude gain . . . . . 24
$\tau_{in}$	Laser cavity round trip time . . . . . 24
$\alpha$	Line-width enhancement factor . . . . . 27
$L_{ext}$	External cavity length . . . . . 27
$\kappa$	Feedback rate . . . . . 28
$\eta_c$	Coupling loss term . . . . . 28
$s$	Normalized time . . . . . 31
$\eta$	Normalized feedback rate . . . . . 31
$T$	Normalized carrier decay time . . . . . 31
$\hat{N}$	Normalized carrier density . . . . . 31
$\mathcal{P}$	Amount of pumping above threshold . . . . . 32
$\hat{\omega}$	Angular frequency of the laser measured relative to the solitary frequency . . . . . 32
$G$	Normalized threshold gain of the laser . . . . . 35
$\Omega$	Angular frequency of the periodic solution at the Hopf point . . . . 36
$\omega_{ext}$	External cavity frequency . . . . . 37
$\omega_R$	Scaled relaxation frequency of the solitary laser . . . . . 38
$L_{ring}$	Total optical path length of the external cavity in the DPCM geometry . . . . . 83
$Y$	Small signal gain saturation term . . . . . 86

*Abstract*

The semiconductor laser diode offers a unique system to investigate nonlinear dynamics when optical feedback is applied. Although there is extensive research of laser diodes with optical feedback from normal dielectric mirrors, very little has been done experimentally to analyze the effects of degenerate phase conjugate feedback from a BaTiO<sub>3</sub> crystal. This research experimentally investigated the dynamics of a single-mode laser diode with weak phase conjugate feedback using both the self-pumped and double phase conjugate geometries. The experimental results validated a mathematical model which numerically evaluates the Lang-Kobayashi coupled differential equations. The model simulated the nonlinear behavior of a laser diode subject to phase conjugate feedback and produced simulated RF and Fabry-Perot spectra of the laser output. Model and experimental results showed frequency locking between the relaxation oscillation and external cavity frequencies and changes in the relaxation oscillation as a function of cavity length. Resonant behavior in the feedback strength necessary to undamp the relaxation oscillation frequency as a function of the cavity length was also captured experimentally and numerically. Validation of the model and experimental results presented in this research significantly contribute to the understanding of the nonlinear behavior of a laser diode subject to optical feedback.

# Experimental Investigation of Nonlinear Dynamics in Single Mode Semiconductor Laser Diodes with Phase Conjugate Feedback

## *I. Introduction*

Injecting feedback into a stable oscillator is well known for causing the oscillator to behave nonlinearly. In particular, a laser diode's response to feedback has been shown to include highly dynamical and even chaotic behavior in its output. The process by which this nonlinear behavior evolves in the laser is not well understood and is the subject of this research. This dissertation examines a semiconductor laser diode entering into a chaotic state brought about by the application of phase conjugate feedback. The investigation was performed both numerically through computer modeling and experimentally using two different methods of phase conjugate feedback; self-pumped and double phase conjugate geometries. This document starts with a brief discussion of why the Air Force is interested in chaotic laser diodes with phase conjugate feedback and continues with an in-depth description of the theory of phase conjugate feedback along with the analysis of nonlinear behavior used throughout the research. This is followed by a discussion of the computer models used in the research and experimental descriptions of the two different types of phase conjugate geometries investigated. The final section reviews the results of the experimental and model outputs and draws conclusions from the research.

### *1.1 Overview*

In typical optical systems using laser diodes, the laser is optically isolated from the rest of the system to prevent feedback from unwanted optical reflections. Optical feedback, even minute amounts in semiconductor laser diodes, on the order of -40 dB

can easily cause the laser to enter into a chaotic state which alters the single mode, single frequency properties of the laser, thus affecting the precise control of the laser in typical applications such as coherent communications and compact disc players.

In contrast, the Air Force and other agencies are investigating methods of exploiting the output of a laser diode intentionally placed in a chaotic state (14)(21). It is envisioned that the broadband and nearly random, but deterministic, output, characteristic of a laser in chaos, will provide the framework for a new generation of secure communications for air-to-air and ground-to-ground networks. It is this novel application that forms the underlying motivation for this research. A complete understanding of this dynamical process inside the laser diode and the coupling to its external cavity providing the optical feedback must be established in order to fully utilize the chaotic state of a laser diode. Theoretical modeling and experimental work have been conducted by the Air Force and civilian institutions on laser diodes intentionally placed in a chaotic state by optical feedback from conventional dielectric mirrors, commonly referred to as normal feedback (15) or through the use of optical injection (14). Only recently has work been done to understand the role of phase conjugate feedback on chaos (26) (2). Research conducted under this effort provides vital details for understanding the onset of chaos caused by phase conjugate feedback from the self-pumped and double phase conjugate geometries.

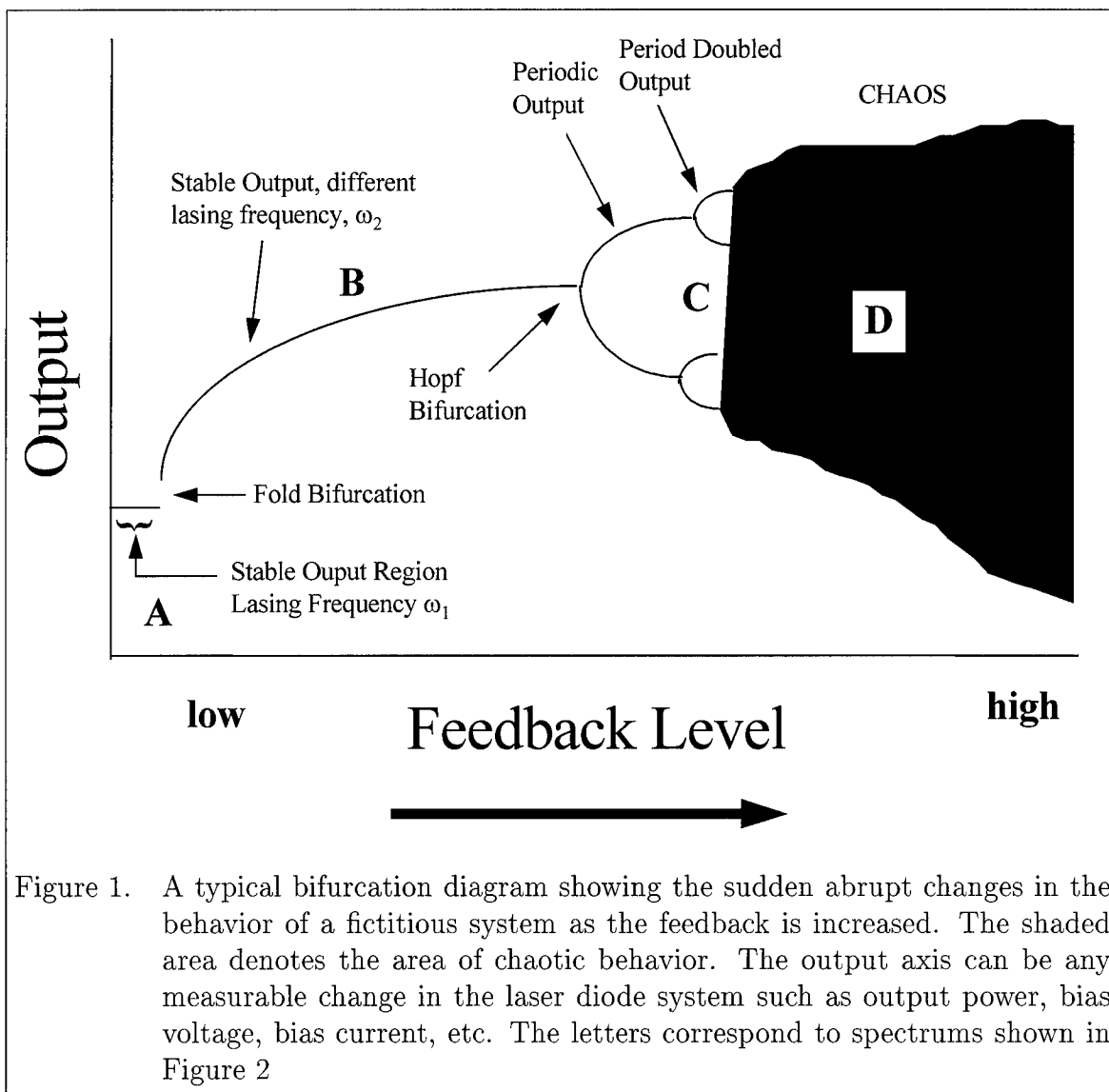
## 1.2 *Introduction to Chaos*

What is *Chaos*? When a system is said to have chaotic behavior, what kind of behavior does this entail? In terms of a system's response, chaos can be defined as aperiodic long-term behavior of a system whose deterministic outcome is highly sensitive to initial conditions (19)(13). In other words, small perturbations to the initial conditions can cause dramatically different outcomes in a chaotic system. The field of study of this complex behavior is called nonlinear dynamics where a nonlinear system is one whose dynamical variables describing the properties of the

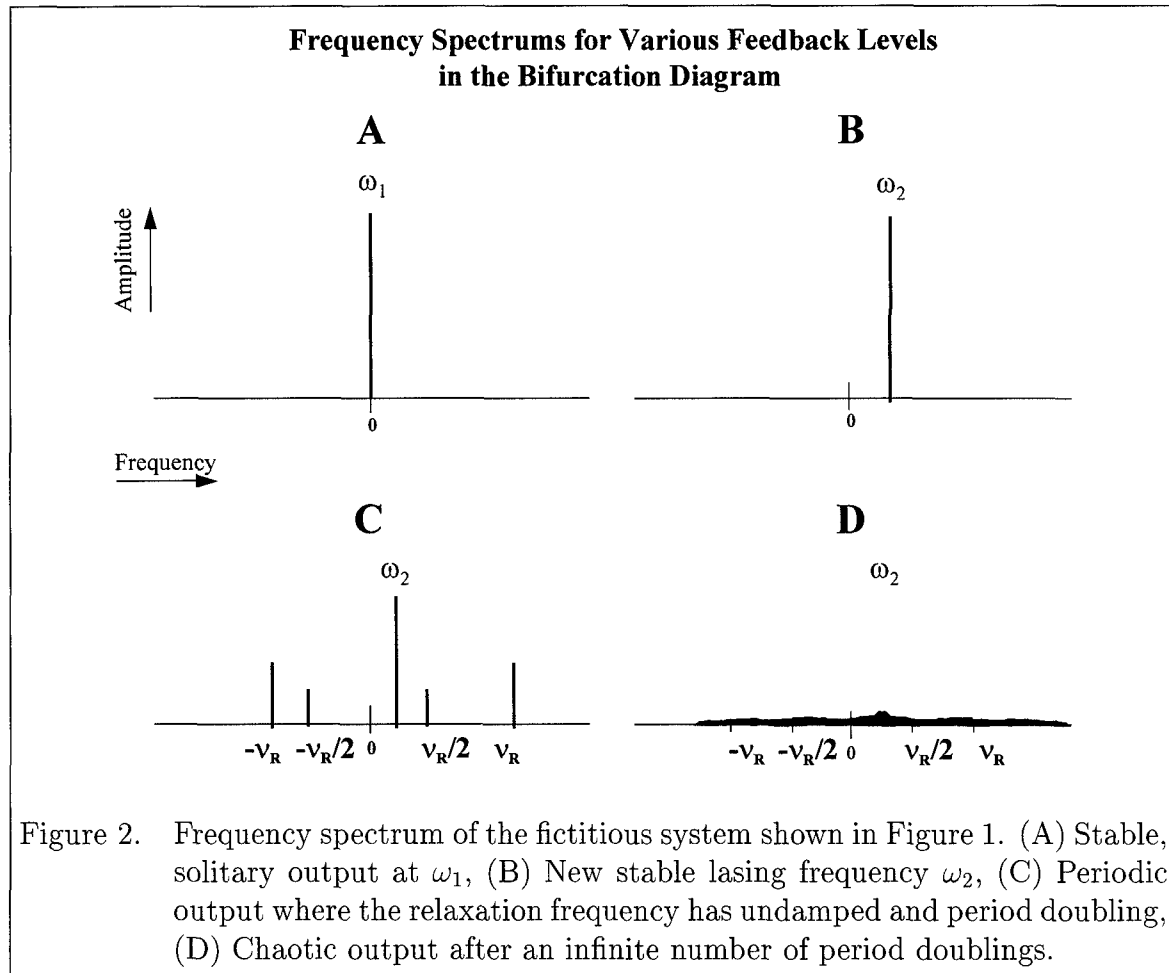
system (position, velocity, acceleration, population, amplitude, etc.) evolve in a nonlinear fashion.

For the laser cavity and specifically for the laser diode, chaos can be achieved by applying optical feedback into the laser cavity. The interference of the interior optical fields with the delayed externally injected fields causes the laser output to go through a series of changes which are dependent on the amplitude and phase of the optical feedback. With extremely small amounts of feedback the laser can overcome the effects of the feedback and its output remains consistent with a solitary laser. However, at a critical level of feedback, the stable laser output will change to a periodic pulsed output and finally to an aperiodic, or chaotic, output. This migration in the output is easily shown in a bifurcation diagram which plots amplitude or intensity output against feedback level.

Figure 1 shows a typical bifurcation diagram of a fictitious system. In this simple example, the output could be the normalized power output of the laser measured at regular time intervals as the feedback is increased. Initially at low feedback levels, the laser output is stable with a solitary lasing frequency  $\omega_1$ . At this point the feedback is too weak to affect the laser and so the output and the system remains stable, area A. As the feedback level is increased, a Fold bifurcation occurs and the laser hops to another external cavity mode. The laser continues to remain stable, however, it now lases at a slightly different frequency  $\omega_2$ . The effect of increasing the feedback in region B now increases the solitary laser output amplitude shown as the increasing solid line for area B. Further increases in feedback eventually causing a Hopf bifurcation to occur and the output amplitude begins to oscillate between two values as shown in area C. In this region the relaxation oscillation frequency of the system is undamped and the output is pulsating at this frequency. Further increasing the feedback causes the output to go through another Hopf bifurcation creating two additional branches. Additional increases in the feedback cause more bifurcations as the period of oscillation doubles (commonly called period doubling).



Finally, after an infinite number of period doubling bifurcations, the output becomes chaotic, denoted by the shaded region in area D of Figure 1. The frequencies created by the period doubling bifurcations can easily be seen in the system's output spectrum. Figure 2 shows how the spectrum of this fictitious system changes as the feedback is increased.



In this particular example the process leading to chaos is described as a period-doubling route because the period of oscillation doubles after each bifurcation. The period doubling route is common in semiconductor laser diode experiments with optical feedback and extremely short external cavities ( $<1$  cm). However, other quasi-periodic routes have also been seen (18). Quasi-periodic behavior describes

the condition when a second frequency emerges from the Hopf bifurcation and the ratio of this new frequency to the previous frequency is not rational.

To illustrate a few of the key terms associated with chaos, consider a simple one-dimensional system  $dX/dt = f(X)$ . Fixed Points for a system are values  $X$  such that  $f(X_o) = 0$ . To examine the behavior of the system, we apply a Taylor series expansion to the equation of motion around the fixed point  $X = X_o$ .

$$f(X) = f(X_o) + (X - X_o)\frac{df}{dX} + \frac{1}{2}(X - X_o)^2\frac{d^2f}{dX^2} + \frac{1}{6}(X - X_o)^3\frac{d^3f}{dX^3} + \dots \quad (1)$$

where the derivatives have all been evaluated at the fixed point  $X = X_o$ . If we let  $x = X - X_o$  and by definition  $f(X_o) = 0$  and keep only the first term of the expansion (a valid assumption of a well-behaved linear system), Eq. (1) can be rewritten as

$$f(X) = \left. \frac{df}{dX} \right|_{X_o} x \quad (2)$$

$$\frac{dx}{dt} = \frac{df(X_o)}{dX} x \quad (3)$$

for which the solution is

$$x(t) = x(0)e^{\lambda t} \quad (4)$$

where

$$\lambda = \frac{df(X_o)}{dX} \quad (5)$$

is the Lyapunov exponent or characteristic value of the fixed point. It is the Lyapunov exponent that determines the behavior of the system. For this system,  $\lambda$  has three possible values (13:79):

1.  $\lambda < 0$ ; The fixed point is a *node* and attracts nearby trajectories (stable).
2.  $\lambda > 0$ ; The fixed point is a *repellor* which repels nearby trajectories (unstable).

3.  $\lambda = 0$ ; The fixed point could be a node, repellor or *saddle point*. It is necessary to look at both the first and second derivatives of  $x(t)$  at the fixed point to determine which case is applicable. For a node, the second derivative changes from positive to negative. The opposite occurs for a repellor for  $\lambda = 0$ . Saddle points require the second derivative of  $x(t)$  to be the same sign on both sides of the fixed point.

In two dimensional (and higher) systems, i.e., systems with two or more independent variables, the eigenvalues can include a complex conjugate pair of eigenvalues  $\lambda_{1,2} = R \pm i\Omega$ , where both  $R$  and  $\Omega$  are real. When  $\lambda$  is complex, Eq. (4) can be rewritten to see the effect of the real and imaginary parts of the eigenvalue

$$x(t) = x(0)e^{Rt}\Re\{e^{\pm i\Omega t}\} \quad (6)$$

$$= x(0)e^{Rt} \cos(\Omega t) \quad (7)$$

We see that the trajectory oscillates at frequency  $\Omega$  and is either damped or amplified, depending on the sign of  $R$ . For  $R > 0$ , the trajectory is repelled and is unstable and when  $R < 0$ , the trajectory is attracted to the fixed point and is stable. When the real part of the eigenvalue is 0, the system becomes purely periodic which results in a trajectory that forms closed loops, or cycles, around the fixed point. Figure 3 is a phase plot of a simple harmonic damped oscillator created by plotting  $x(t)$  versus the velocity,  $dx/dt$ , to show the behavior of the trajectories when  $\lambda$  is complex. Table 1 summarizes the behavior of the system for the different eigenvalue possibilities.

Table 1. Summary of the behavior of trajectories due to different eigenvalues.

Eigenvalue, $\lambda$	Behavior
Real, Negative	Stable Node
Real, Positive	Unstable Repellor
Complex, Negative real part	Spiral, attracting stable focus
Complex, Positive real part	Spiral, repelling unstable focus
Complex, Real Part = 0	Limit Cycle

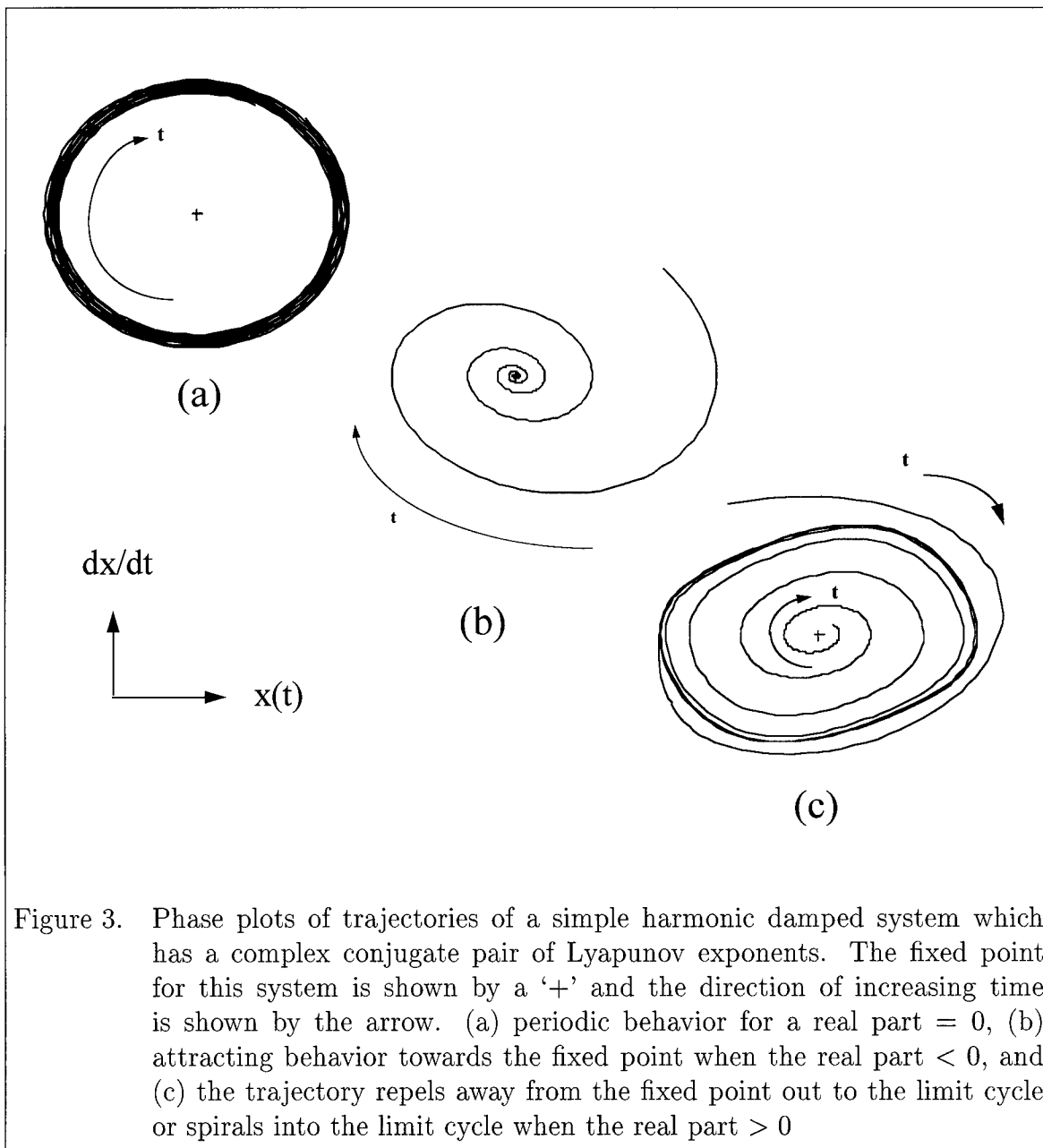


Figure 3. Phase plots of trajectories of a simple harmonic damped system which has a complex conjugate pair of Lyapunov exponents. The fixed point for this system is shown by a '+' and the direction of increasing time is shown by the arrow. (a) periodic behavior for a real part = 0, (b) attracting behavior towards the fixed point when the real part < 0, and (c) the trajectory repels away from the fixed point out to the limit cycle or spirals into the limit cycle when the real part > 0

According to the Poincaré-Bendixson Theorem, there are only two possible outcomes for the trajectory of a two-dimensional system with complex eigenvalues (13:104):

- The trajectory approaches a fixed point of the system as  $t \rightarrow \infty$ . (Figure 3b)
- The trajectory approaches a limit cycle as  $t \rightarrow \infty$ . (Figure 3a, c)

The impact of this theorem is that in order to have chaotic behavior, the system must be of dimension three or higher since the outcome of two-dimensional behavior is determined by the Poincaré-Bendixson theorem (13).

An excellent example of a two dimensional system is the solitary Class B laser (one without feedback). This system can be modeled as a simple two-level system, as shown in Figure 4, with the usual pumping rate,  $R_p$ , stimulated transition coefficients,  $B_{21}$  and  $B_{12}$ , and the spontaneous transition rate,  $A_{21}$ . The populations of levels 1 and 2 are  $N_1$  and  $N_2$ , respectively, and  $P$  is the number of photons. The set of coupled differential equations describing the population difference between levels 1 and 2,  $\Delta N = N_2 - N_1$  are

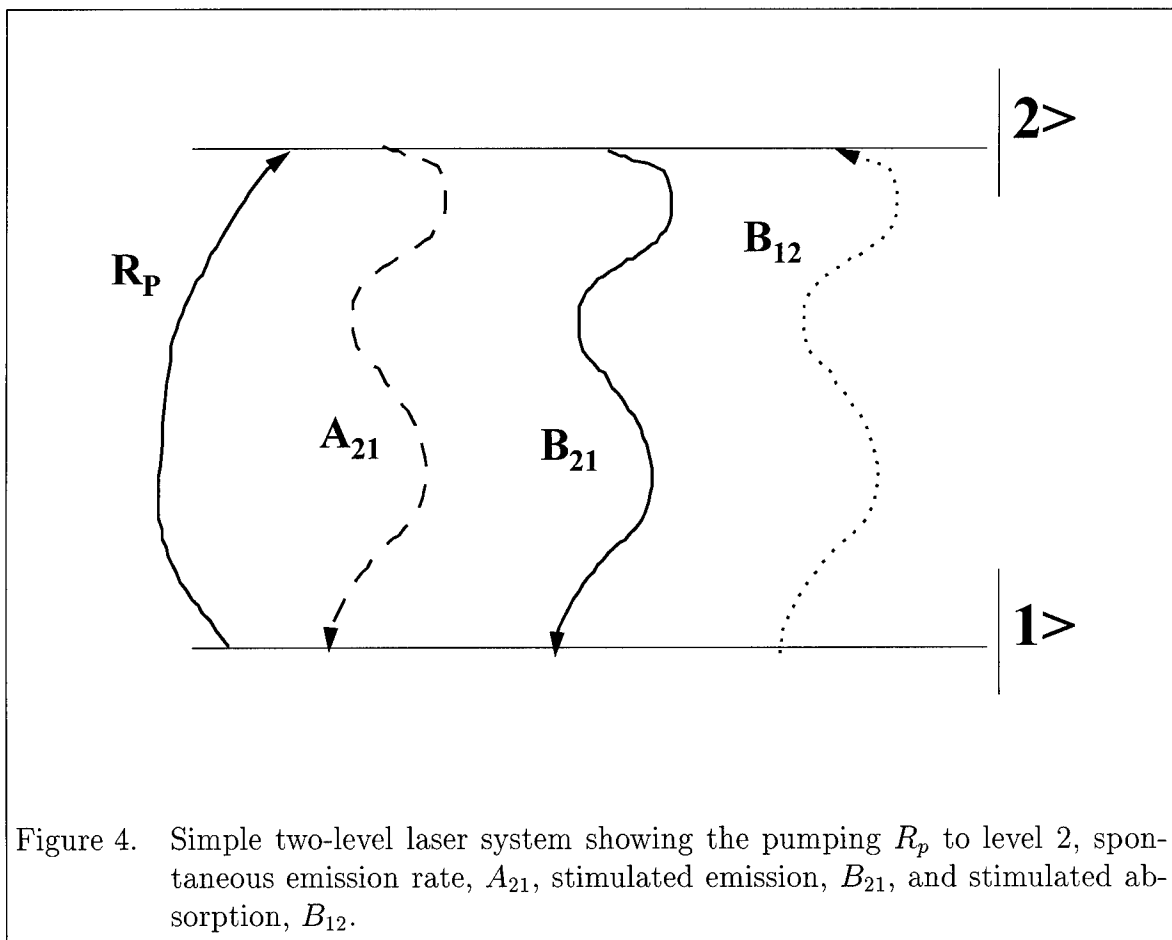
$$\frac{d\Delta N}{dt} = -2B\Delta NP + 2A_{21}(\bar{N} - \Delta N) \quad (8)$$

$$\frac{dP}{dt} = BP\Delta N - \gamma P \quad (9)$$

where  $B_{12} \approx B_{21} = B$ ,  $\bar{N} = (R_p/A_{21} - 1) N_1$  is the unsaturated population of level 2 without stimulated emission ( $P = 0$ ) and  $\gamma$  is a net loss of photons in the cavity due to various loss mechanisms such as absorption and scattering.

At the steady state condition we find that there are two fixed points:

$$\begin{aligned} \#1: \quad \Delta N &= \bar{N} \quad , \quad P = 0 \\ \#2: \quad \Delta N &= \gamma/B \quad , \quad P = A_{21}(\bar{N}/\gamma - 1/B) \end{aligned}$$



and the associated Jacobian matrix for the eigenvalues is

$$J = \begin{pmatrix} -2A_{21} - BP & -2B\Delta N \\ BP & B\Delta N - \gamma \end{pmatrix} \quad (10)$$

When the Jacobian is evaluated at fixed point #1, two eigenvalues can be found

$$\lambda_1 = -2A_{21}$$

$$\lambda_2 = B\bar{N} - \gamma$$

Since  $A_{21}$  is never negative, the first eigenvalue is always negative. Because we have no emission from the laser at  $P = 0$ , the losses,  $\gamma$ , are greater than the stimulated

emission. Thus the second eigenvalue is also always negative for this fixed point. Since both eigenvalues are negative and real, fixed point #1 is a stable node and describes the trivial case of the laser operating below threshold. However, as the laser approaches the threshold condition,  $\lambda_2$  becomes less negative and equals zero precisely at threshold since at this point the gain equals the losses. At this precise condition, fixed point #1 actually becomes unstable as the laser crosses the threshold condition. As we shall see, this unstable condition is counteracted by fixed point #2 which becomes stable as the threshold condition is reached and the laser operates in a continuous-wave (c-w) mode, as will be shown below.

Evaluating the Jacobian at the second fixed point, we find a complex conjugate pair of eigenvalues

$$\lambda_{\pm} = \frac{-B\hat{N}}{\gamma} \pm \sqrt{\frac{B^2\bar{N}^2}{\gamma^2} - \frac{2\gamma}{A_{21}} \left( \frac{B\bar{N}}{\gamma} - 1 \right)} \quad (11)$$

Taking the Nd-YAG laser system as an example, Table 2 lists typical values for the parameters. From the table, it is easily shown that  $(2\gamma)/(A_{21}) (B\bar{N}/\gamma - 1) \gg B^2\bar{N}^2/\gamma^2$  so the eigenvalues can be simplified to

$$\lambda_{\pm} = \frac{-B\bar{N}}{\gamma} \pm i\sqrt{\frac{2\gamma}{A_{21}} \left( \frac{B\bar{N}}{\gamma} - 1 \right)} \quad (12)$$

For lasing, the gain is always larger than the losses,  $B\bar{N} > \gamma$ , so the term under the radical is positive. Thus for this case, fixed point #2 is a stable spiral node since the two eigenvalues have negative real parts and non-zero imaginary parts. Figure 5 shows a graphical view of this fixed point.

Table 2. Examples of typical parameters for a Nd-YAG laser system.

$A_{21} = 10^{-4} \text{ sec}^{-1}$
$\bar{N} = 7.33 * 10^{18} / \text{cm}^3$
$\gamma = 0.99 \text{ cm}^{-1}$
$B = 2.7 - 8.8 * 10^{-19} \text{ cm}^2 / \text{sec}$

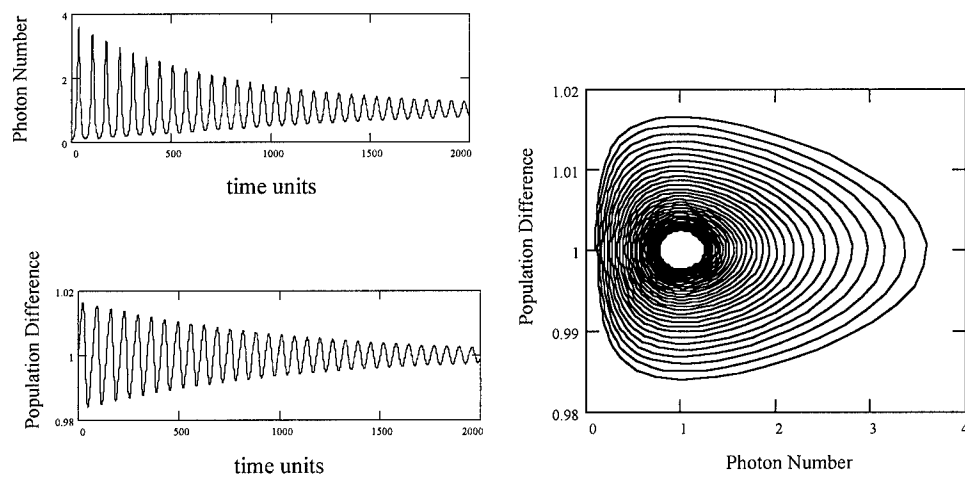


Figure 5. Graphical depiction of the time evolution of the Nd-YAG two-level laser system showing the spiraling convergence to a limit cycle around fixed point #2. Initial conditions are  $BP/A_{21} = 0.1$  and  $B\Delta N/\gamma = 1$ .

As seen in this figure, the damped periodic behavior towards the steady state output value is the relaxation oscillations. It is clear from this simple example that a system with only two degrees of freedom cannot reach chaos since the relaxation oscillations are always damped and no mechanism exists to cause them to become undamped. Therefore a third degree of freedom is necessary, such as optical feedback, for chaotic behavior to develop as stated previously by the Poincaré-Bendixson Theorem.

### *1.3 Phase Conjugating Mirrors (PCM)*

To provide the required third degree of freedom, feedback can be applied to a laser diode by several different methods including electrical modulation of the bias current and injecting optical feedback into the laser cavity. In particular, for this research a phase conjugating mirror is used in order to examine the unique effects of the external cavity formed by the laser diode and the feedback mirror. PCMs are unique in that they reflect (produce) a phase conjugate beam which retraces the exact path and phase front of the input beam. Distortions and changes induced by optics in the path are “un-done” by the conjugate beam as demonstrated by Figure 6. Therefore at any point along the optical path the phase front of the conjugate beam is identical to that of the original beam. The two types of PCMs used in this research are created by a  $\text{BaTiO}_3$  crystal that is either self pumped or double pumped. Figure 7 shows a schematic view of the two configurations used.

The self-pumped CAT geometry shown in Figure 7 is the easiest configuration for establishing a conjugate signal; however, it has the disadvantage of having the reflectivity depend solely on the intensity of the input beam, S1. So for low feedback levels, the input beam must also be reduced resulting in the reduction in the strength of the holographic grating formed in the crystal. But this slight disadvantage is greatly out-weighed by the fact that this configuration is easy to implement in the lab and has a large range of incident angles that can produce an adequate conjugate

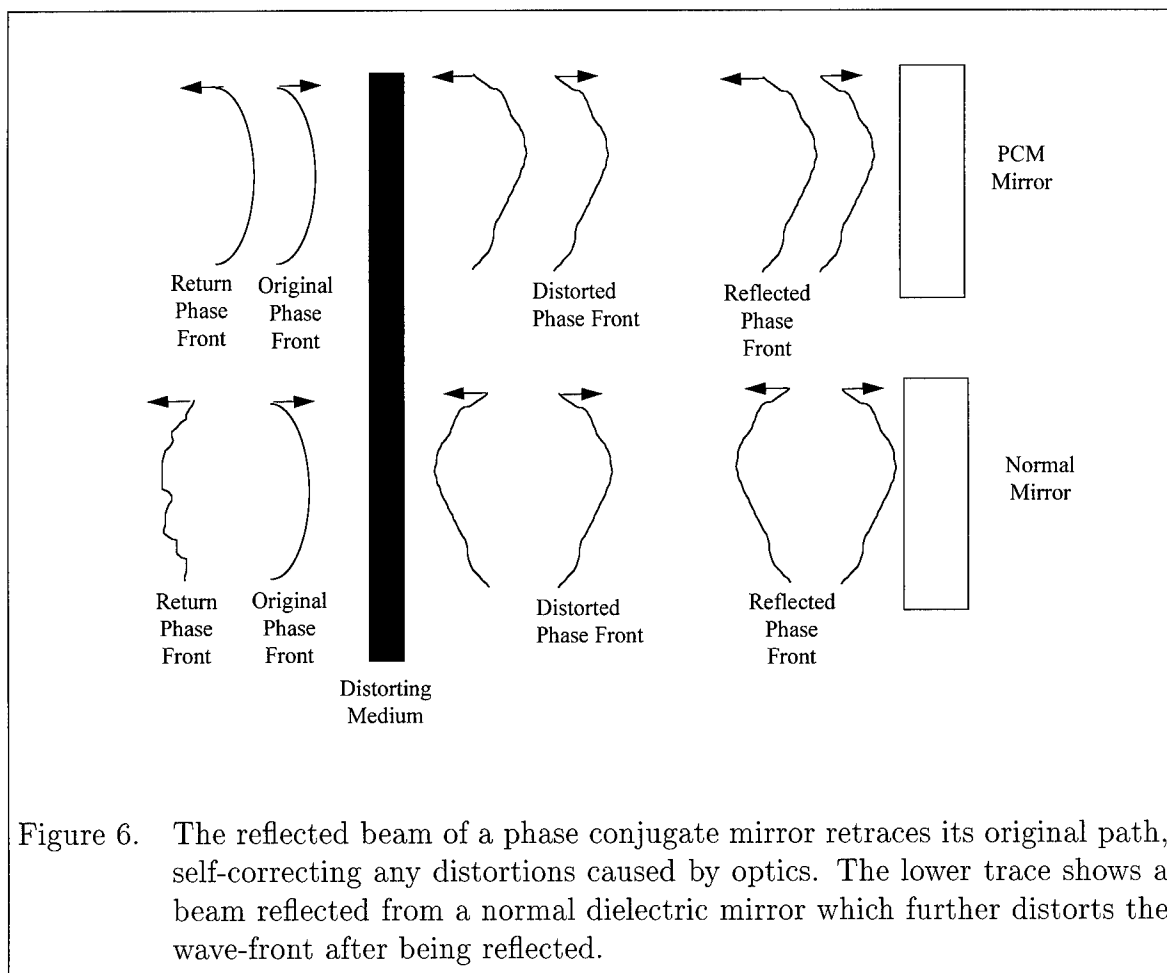


Figure 6. The reflected beam of a phase conjugate mirror retraces its original path, self-correcting any distortions caused by optics. The lower trace shows a beam reflected from a normal dielectric mirror which further distorts the wave-front after being reflected.

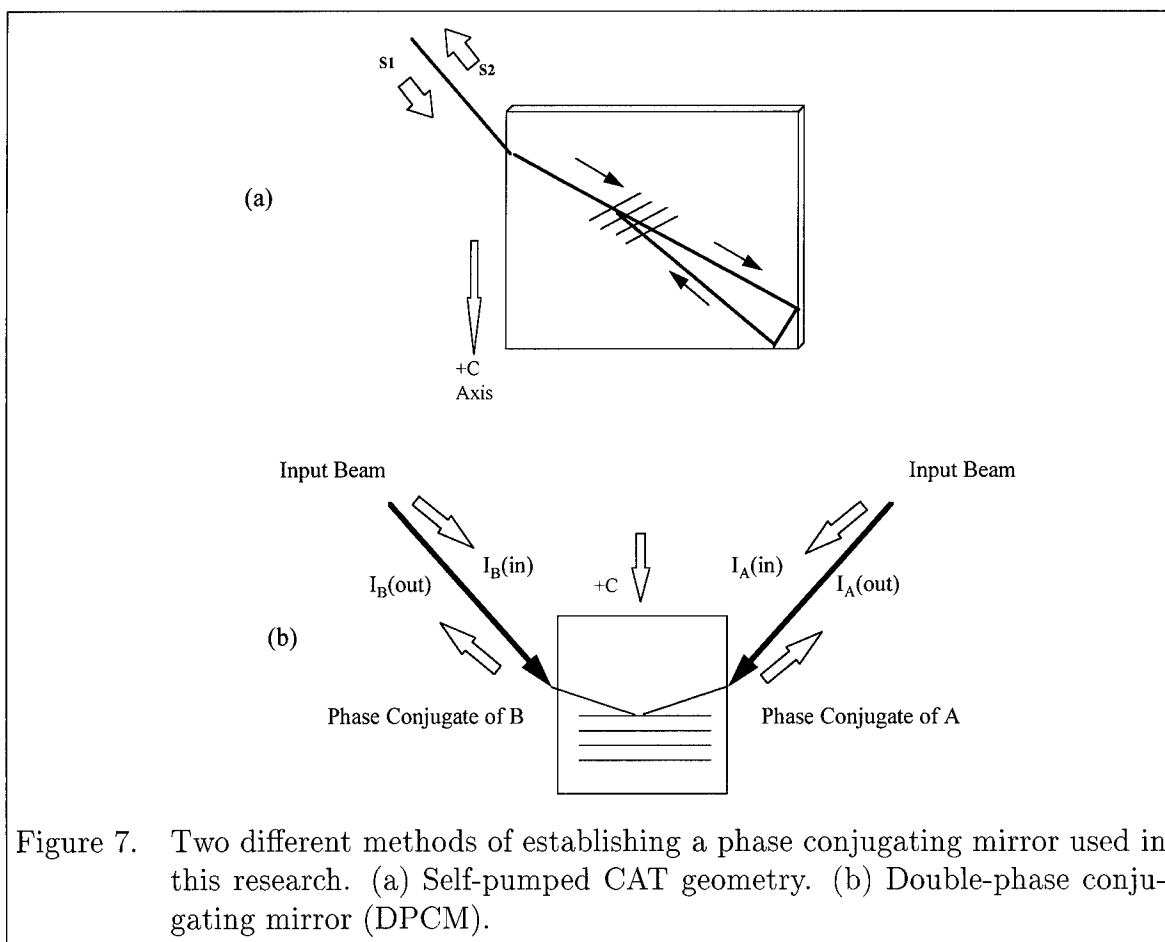


Figure 7. Two different methods of establishing a phase conjugating mirror used in this research. (a) Self-pumped CAT geometry. (b) Double-phase conjugating mirror (DPCM).

signal. Garret *et al* showed that a range of incident angles, with respect to the c-axis, of  $15^\circ - 75^\circ$  can produce reflectivities as high as 40% in  $\text{BaTiO}_3$  at a wavelength of 514 nm with the optimum incident angle of  $29.1^\circ$  (8). The CAT geometry also suffers from a relatively slow rise time for the conjugate signal to reach 90% of its steady state value. Hengst measured this rise time to vary between  $<0.5$  second to tens of seconds, depending on the incident intensity and angle of beam  $S_1$  (12:22). However, the onset time to establish the mirror is not critical for this research. An investigation of the dynamic response time once the mirror is established and its effect on the laser dynamics forms a part of the present investigation.

The transmission grating double phase conjugate mirror (DPCM) configuration in Figure 7b offers the advantage of having two phase conjugate signals to use as a

feedback signal to the laser diode and has a faster onset time than the CAT geometry. When only one conjugate signal is required for feedback, the second beam can be blocked with a high quality optical isolator placed in one of the input legs. Weiss *et al* showed that in BaTiO<sub>3</sub> the ratio of the conjugate intensities is equal to the ratio of input intensities (28)

$$\frac{I_A(out)}{I_B(out)} = \frac{I_B(in)}{I_A(in)} \quad (13)$$

If  $I_A(out)$  is chosen as the feedback signal, this configuration also allows control of the conjugate return without adjusting the input intensity  $I_A(in)$ . Now the reflectivity of the conjugate mirror,  $R_{PCM}$ , defined as the ratio of the output intensity to the input intensity, is proportional to the second input beam,  $R_{PCM} \propto I_B(in)$ . This allows adjustment of the reflectivity without affecting the input beam  $I_A(in)$ . In addition, this conjugate mirror may also be established using a reflection grating DPCM configuration. However, current research shows that the reflection grating configuration is harder to implement, and may not offer the reliable control of the conjugate signal required for the experiments.

Table 3 summarizes the dependencies of  $R_{PCM}$  and the controlling parameters used in the experiments. For each configuration, the resultant “reflected” E-field can be described as a modified conjugate of the input field

$$\vec{E}^*(t) = \sqrt{R_{PCM}} \vec{E}^*(t) \exp\{i(\omega t + \phi_{PCM})\} \quad (14)$$

where  $\vec{E}^*(t)$  is the complex conjugate amplitude of the input beam,  $\omega$  is the angular optical frequency, and  $\phi_{PCM}$  is a phase shift of the conjugate beam relative to the probe beam. For photorefractive materials, such as BaTiO<sub>3</sub>, the conjugate beam is in-phase with the probe beam, therefore  $\phi_{PCM} = 0$ .

As a starting point for developing the theory, the next chapter review the derivation of the rate equations describing the laser diode system without feedback. The phase conjugate term discussed earlier in this section is then applied to the

Table 3. Listing of the two different phase conjugate mirrors and their controlling parameters used in the research.

Mirror Configuration	Controlling Parameter	Dis/Advantage
CAT	$R_{PCM} \propto S_1$	Reflectivity values High but dependent on input beam. Easy alignment.
DPCM	$R_{PCM} \propto I_B(in)$	Reflectivity values Low but can be varied with constant signal beam.

solitary rate equations to establish the three coupled, time-delayed, rate equations necessary for chaotic development. The theory section is then followed by a brief discussion of the two computer models that numerically integrate the set of nonlinear equations. The models are then used as a tool to analyze the experimental data. The remainder of the dissertation encompasses the experimental descriptions, experimental results and finally, comparisons between the model and analytical predictions and the experimental results.

## *II. Theory of Nonlinear Dynamics for Phase Conjugate Feedback in Laser Diodes*

Semiconductor laser diodes are extremely sensitive to external feedback due to the low reflectivities of their output mirrors (facets). The low reflectivity allows even minute amounts of feedback into the gain region of the laser diode which can cause the diode to enter into a state of chaos. Optical feedback can be established by two methods, conventional feedback (CF) and phase conjugate feedback (PCF). There has been extensive research investigating conventional feedback with normal dielectric mirrors both analytically (22)(23) and experimentally (16)(30). In this research, phase conjugate feedback is used for the study of nonlinear dynamics for its relative ease of implementation and its unique characteristic phase and frequency locking of the feedback signal not found in other types of feedback. In contrast to PCF, CF requires precise alignment and focusing of the feedback beam and vibrations in any of the optics can induce random phase variations in the feedback beam which randomly excite various external cavity modes. Published literature on the study of laser diodes with PCF has focused on either computer models that show chaotic behavior (11) or experimental observations of chaotic behavior with PCF (17). However, there is a definite lack of published material that validates computer models, and analytical approximations, with experimental data. Another unique aspect for using phase conjugate feedback, is that there is no conjugate feedback counterpart in electrical or mechanical feedback systems previously studied in chaos.

The theory of phase conjugate feedback begins with a description of the rate equations for the dynamics inside the laser cavity followed by the inclusion of the phase conjugate feedback term. Figure 8 shows a diagram of the different components developed in this section. The laser cavity on the left emits photons into the external cavity which are then partially retro-reflected back towards the laser cavity from the phase conjugate mirror. These reflected photons reach the exit facet of the laser with

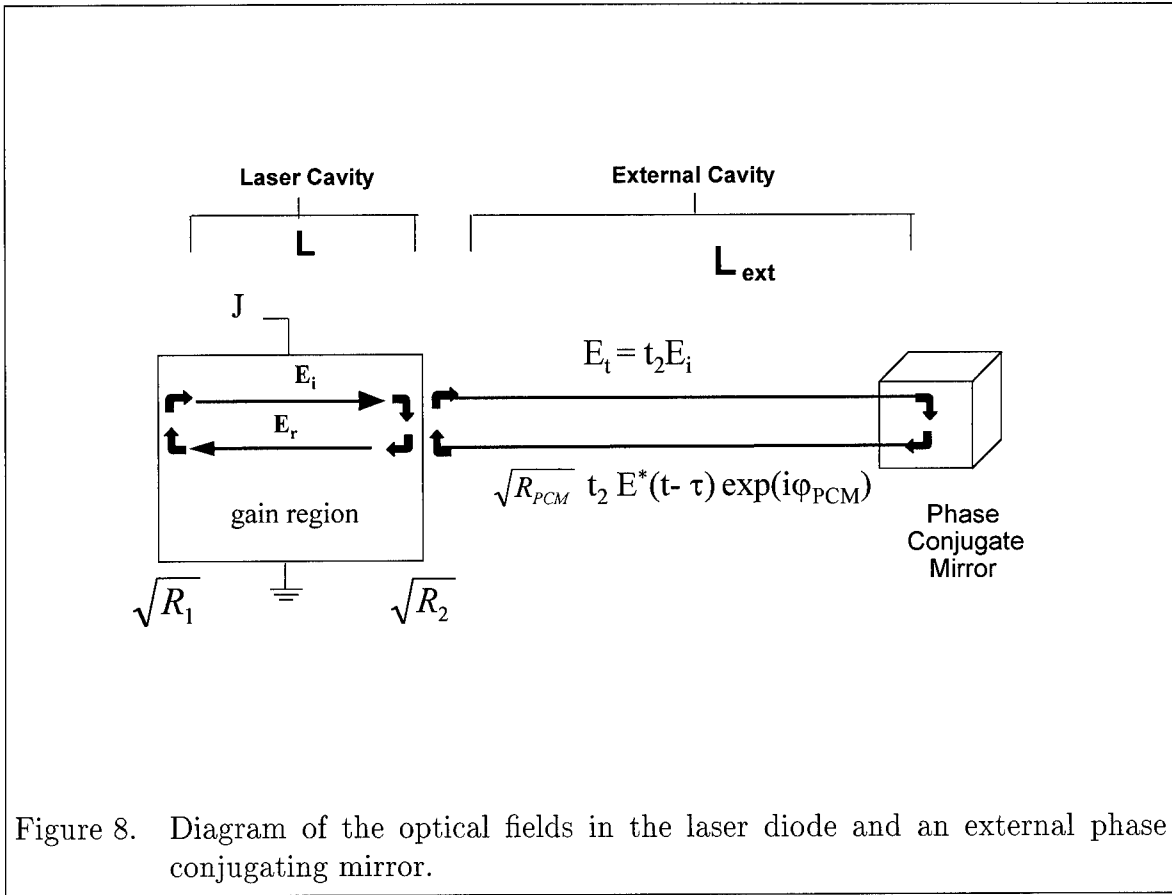


Figure 8. Diagram of the optical fields in the laser diode and an external phase conjugating mirror.

a portion re-entering the laser cavity and the rest being retro-reflected back into the external cavity for another round trip. This interface at the laser and external cavity sets the boundary conditions for how the E-fields interact and how the gain medium is altered in the laser cavity. The change in optical gain is the mechanism that drives the laser into chaotic development. Once a complete description of the fields inside the laser cavity is developed, a linear stability analysis is performed to determine operating regions and feedback levels where the laser diode may go chaotic.

### 2.1 Development of Rate Equations Without Feedback

The two rate equations that are of primary concern for laser diodes are the electron-hole pair number,  $N(t)$ , and the optical field,  $\vec{E}(t)$ . Starting with  $N(t)$ , Yamada developed an equation which adequately depicts the dynamics of the electron-hole pairs in the gain region (29):

$$\frac{\partial N}{\partial t} = D\nabla^2 N + \frac{J}{ed} - \mathcal{R}(N) \quad (15)$$

where  $N(t)$  is the number of electron-hole pairs and  $D\nabla^2 N$  accounts for the diffusion of carriers in the gain medium ( $D$  is the diffusion coefficient). Diffusion of carriers can be considered instantaneous ( $\ll 1$  ps) on the time scale of the carrier lifetimes which are typically  $\sim 1$  ns, and therefore can be neglected in the case of semiconductor laser diodes. The rate equation also includes the addition of carriers in the active region of length  $d$  due to an applied pumping current density,  $J$ . The last term,  $\mathcal{R}(N)$ , is the lump sum rate (#/sec) of all loss mechanisms of electron-hole pairs which include both stimulated and spontaneous emission,

$$\mathcal{R}(N) = R_{st}(N, P) + \frac{N}{\tau_N} \quad (16)$$

Here  $\tau_N$  is the electron-hole carrier lifetime and accounts for all spontaneous emission and non-radiative recombinations. The stimulated radiation rate,  $R_{st}(N, P)$ , is a

function of both the electron-hole pair number,  $N$ , and the laser cavity photon number,  $P$ . The photon number is a dimensionless quantity and represents the magnitude of the normalized electric field with the energy of a cavity photon,  $\hbar\omega$ , such that  $P = |E|^2$ . Furthermore, the loss of a carrier pair,  $\delta N = -1$ , leads to the creation of a photon,  $\delta P = +1$ . Van Tartwijk *et al* showed that the stimulated emission rate can be written as (27)

$$R_{st}(N, P) = v_g g(N) P \quad (17)$$

where  $v_g$  is the group velocity of the longitudinal mode inside the laser cavity and  $g(N)$  is the electron-hole dependent gain coefficient. Based on numerical calculations one can expand the gain coefficient around the threshold value, keeping only the lowest two terms such that

$$g(N) = g(N_{th}) + \frac{\partial g}{\partial N}(N - N_{th}) + \dots \quad (18)$$

where  $g(N_{th})$  is the threshold gain coefficient and  $N_{th}$  is the number of electron-hole pairs at threshold (27:101). Since the electron-hole pairs are restricted to remain in the active region and the injected optical field may extend into the adjacent areas outside the active region, the resultant optical gain of the laser cavity,  $g_{opt}$ , is smaller than  $g(N)$

$$g_{opt} = \Gamma g \quad (19)$$

The confinement factor or filling factor,  $\Gamma$ , describes the fraction of photons that interact in the gain region of the laser,  $0 \leq \Gamma \leq 1$ . Upon substitution of Eqs. (18) and (19) into Eq. (17), the stimulated emission rate can be rewritten as,

$$\begin{aligned} R_{st} &= \left[ v_g g(N_{th}) + v_g \frac{\partial g}{\partial N}(N - N_{th}) \right] P \\ &= \left[ \frac{v_g g_{opt}(N_{th})}{\Gamma} + \xi(N - N_{th}) \right] P \end{aligned} \quad (20)$$

$$= \left[ \frac{\Gamma_o}{\Gamma} + \xi(N - N_{th}) \right] P$$

where  $\Gamma_o = v_g g_{opt}(N_{th})$  is the total loss rate of photons in the laser cavity ( $s^{-1}$ ) or commonly called the inverse photon lifetime,  $\tau_p^{-1}$ , and  $\xi = v_g \partial g / \partial N$  is the differential gain rate. Substituting  $\mathcal{R}(N)$  and  $R_{st}$  into Eq. (16) yields the expression for the rate equation for the electron-hole pairs inside the cavity without feedback,

$$\frac{dN(t)}{dt} = \frac{J}{e} - \frac{N(t)}{\tau_N} - \left[ \frac{\Gamma_o}{\Gamma} + \xi(N(t) - N_{th}) \right] |E(t)|^2 \quad (21)$$

where  $E(t)$  is the amplitude of the complex electric field  $\vec{E}(t) = E(t) \exp(i\omega t)$ . Since we are only concerned about the number of carriers above threshold, we can substitute  $\Delta N(t) = N(t) - N_{th}$  and let  $p = (J/e)/(N_{th}/\tau_N)$  be the ratio of carriers created by the pumping current to carriers lost. This transforms the electron-hole rate equation into

$$\frac{d\Delta N(t)}{dt} = (p - 1) \frac{N_{th}}{\tau_N} - \frac{\Delta N(t)}{\tau_N} - \left[ \frac{\Gamma_o}{\Gamma} + \xi \Delta N(t) \right] |E|^2 \quad (22)$$

Development of a similar rate equation for the E-field in the cavity involves characterizing the gain and loss mechanisms for the active layer in the laser diode and examining the frequency dependent refractive index. Table 4 lists the primary loss mechanisms in the laser cavity that are considered relevant in the literature. The material loss coefficient,  $\alpha_{mat}$ , is derived from the imaginary part of the laser gain medium susceptibility,  $\chi$ , for the unpumped material and represents photons lost to absorption into the material without a pumping current applied. The second loss coefficient,  $\alpha_{int}$ , is loss of photons due to scattering, with  $\sigma$  being the scattering cross section. The total absorption loss,  $\alpha_{abs}$ , is the sum of the first two coefficients plus an additional loss of photons due to absorption from the pumped gain medium. For convenience, the optical gain coefficient of the laser diode cavity,  $g_{opt}$ , is the net gain coefficient in the semiconductor gain medium which incorporates the effect of

absorption from the unpumped material and absorption due to pumping:

$$g_{opt} = -\frac{\omega}{cn}(\chi_o'' + \chi_p'') \quad (23)$$

The mirror loss coefficient in Table 4 is the effect due to the laser facet reflectivities,  $R_1$  and  $R_2$ , distributed over a complete round trip of the internal laser cavity,  $2L$ .

Table 4. The absorption coefficients ( $cm^{-1}$ ) in an externally pumped FP-resonator consisting of an active medium confined between mirrors (27:98).  $\chi_o''$  and  $\chi_p''$  are the two elements of the total scalar susceptibility in an isotropic material due to unpumped background material losses and losses due to external pumping, respectively.

Material Loss	$\alpha_{mat} = \omega\chi_o''/cn$
Internal Loss	$\alpha_{int} = \sigma/n\epsilon_o$
Absorption Loss	$\alpha_{abs} = \alpha_{mat} + \alpha_{int} + \omega\chi_p''/cn$
Mirror Loss	$\alpha_m = (1/2L) \ln(1/R_1R_2)$

To derive the E-field rate equation, we start with the round trip amplitude gain threshold condition for lasing

$$\mathcal{G} = \sqrt{R_1R_2} \exp \left\{ -2i\frac{n\omega}{c}L - \alpha_{abs}L \right\} = 1 \quad (24)$$

where  $\mathcal{G}$  is the round trip amplitude gain in the laser cavity, and  $n = n(N, \omega)$  is the carrier and frequency dependent refractive index of the laser gain medium. Since  $(\omega n(N, \omega))/c$  is carrier and frequency dependent, a linear expansion around the threshold gives

$$\frac{\omega n}{c} \cong \frac{n_{th}\omega_{th}}{c} + \frac{\omega_{th}}{c} \frac{\partial n}{\partial N} (N - N_{th}) + \frac{1}{c} (n_{th} + \omega_{th} \frac{\partial n}{\partial \omega}) (\omega - \omega_{th}) \quad (25)$$

where  $N_{th}$ ,  $n_{th}$ , and  $\omega_{th}$  are the electron-hole number, refractive index and optical frequency at the laser threshold, respectively. Substituting Eq. (25) into Eq. (24)

yields

$$\mathcal{G} = \sqrt{R_1 R_2} \exp \left\{ -2i \left( \frac{n_{th} \omega_{th}}{c} + \frac{\omega_{th}}{c} \frac{\partial n}{\partial N} (N - N_{th}) + \frac{n_g}{c} (\omega - \omega_{th}) \right) L - \alpha_{abs} L \right\} \quad (26)$$

where  $n_g = n_{th} + \omega_{th} \partial n / \partial \omega$  is the group refractive index for the longitudinal mode of the laser cavity. Using the mirror loss term from Table 4, this equation can be re-written in exponential form

$$\begin{aligned} \mathcal{G} &= \exp \{ -\alpha_m L \} \\ &\times \exp \left\{ -\frac{2i}{c} \left( n_{th} \omega_{th} + \omega_{th} \frac{\partial n}{\partial N} (N - N_{th}) + n_g (\omega - \omega_{th}) \right) L \right\} \\ &\times \exp \{ -\alpha_{abs} L \} \end{aligned} \quad (27)$$

The absorption coefficient,  $\alpha_{abs}$ , can also be written as

$$\begin{aligned} \alpha_{abs} &= \alpha_{int} + \frac{\omega}{c n} (\chi_o'' + \chi_p'') \\ &= \alpha_{int} - g_{opt} \\ &= \alpha_{int} - \Gamma g(N) \end{aligned} \quad (28)$$

where Eq. (19) was used in the last step. Finally, the round trip amplitude gain is separated into the product of a frequency independent term,  $\mathcal{G}_1$ , and a frequency dependent term,  $\mathcal{G}_\omega$ , such that  $\mathcal{G} \equiv \mathcal{G}_1 \mathcal{G}_\omega$  where

$$\mathcal{G}_1 = \exp \left\{ \left( (\Gamma g(N) - \alpha_{int} - \alpha_m) L - 2i \frac{\omega_{th}}{c} \frac{\partial n}{\partial N} (N - N_{th}) \right) \right\} \quad (29)$$

$$\mathcal{G}_\omega = \exp \left\{ -2i \frac{n_{th} \omega_{th}}{c} L - 2i \frac{L n_g}{c} (\omega - \omega_{th}) \right\} \quad (30)$$

At threshold,  $N = N_{th}$ ,  $\omega = \omega_{th}$ , and  $\mathcal{G} = 1$ , so the term  $2n_{th} \omega_{th} L / c$  in  $\mathcal{G}_\omega$  must be an integer multiple of  $2\pi$  and therefore can be ignored. Also, using  $\tau_{in} = 2L n_g / c$  as

the cavity round trip time,  $\mathcal{G}_\omega$  can be written as

$$\begin{aligned}\mathcal{G}_\omega &= \exp\{-i(\omega - \omega_{th})\tau_{in}\} \\ &= \exp\{i\omega_{th}\tau_{in}\} \exp\{-i\omega\tau_{in}\}\end{aligned}\quad (31)$$

Recognizing that  $i\omega$  in the Fourier domain for a monochromatic field yields  $d/dt$  in the time domain, this may be rewritten as

$$\mathcal{G}_\omega = \exp\{i\omega_{th}\tau_{in}\} \exp\{-\tau_{in}d/dt\} \quad (32)$$

Two valid assumptions can be made at this time. The first is that the frequency of oscillation is close to the threshold value,  $\omega \cong \omega_{th}$ , and the second is that the E-field has a slowly varying amplitude for each round trip inside the laser cavity:

$$\vec{\mathbf{E}}(t) = \vec{E}(t) \exp\{i\omega_{th}t\} \quad (33)$$

The field after one round trip in the gain medium is then

$$\vec{\mathbf{E}}(t + \tau_{in}) = \mathcal{G}_1 \mathcal{G}_\omega \vec{\mathbf{E}}(t) = \mathcal{G}_1 \exp\{i\omega_{th}\tau_{in}\} \exp\{-\tau_{in}d/dt\} \vec{\mathbf{E}}(t) \quad (34)$$

The derivative in the exponential is expanded as a power series,

$$\begin{aligned}\exp\{-\tau_{in}d/dt\} \vec{\mathbf{E}}(t) &= \sum_{n=0}^{\infty} \frac{(-\tau_{in}d/dt)^n}{n!} \vec{\mathbf{E}}(t) \\ &= \sum_{n=0}^{\infty} \frac{\vec{\mathbf{E}}^{(n)}(t)}{n!} [(t - \tau_{in}) - t]^n \\ &= \vec{\mathbf{E}}(t - \tau_{in})\end{aligned}\quad (35)$$

which applies a time shift to the E-field such that

$$\vec{\mathbf{E}}(t) = \mathcal{G}_1 \vec{\mathbf{E}}(t - \tau_{in}) \quad (36)$$

From the slowly varying amplitude approximation made earlier, the time shifted change in the field is small and can be approximated by a first order differential:

$$\vec{\mathbf{E}}(t - \tau_{in}) \cong \vec{\mathbf{E}}(t) - \tau_{in} \frac{d\vec{\mathbf{E}}(t)}{dt} \quad (37)$$

By substituting the differential approximation in Eq. (37) into Eq. (36), the E-field time rate of change now becomes

$$\frac{d\vec{\mathbf{E}}(t)}{dt} = \frac{1}{\tau_{in}} \left(1 - \frac{1}{\mathcal{G}_1}\right) \vec{\mathbf{E}}(t) \quad (38)$$

Since the gain,  $\mathcal{G}_1$ , is close to unity during lasing, an exponential series expansion can be applied to the term  $(1 - 1/\mathcal{G}_1)$  such that

$$1 - 1/\mathcal{G}_1 \approx (\Gamma g(N) - \alpha_{int} - \alpha_m)L - 2i \frac{\omega_{th}}{c} \frac{\partial n}{\partial N} (N - N_{th}) \quad (39)$$

This result is substituted into Eq. (38) producing the E-field rate equation

$$\frac{d\vec{\mathbf{E}}(t)}{dt} = \frac{1}{\tau_{in}} \left[ (\Gamma g(N) - \alpha_{int} - \alpha_m)L - 2iL \frac{\omega_{th}}{c} \frac{\partial n}{\partial N} \Delta N(t) \right] \vec{\mathbf{E}}(t) \quad (40)$$

Substituting for the full expression for  $\tau_{in}^{-1} = c/(2Ln_g)$  and Eq. (18) for  $g(N)$  gives

$$\frac{d\vec{\mathbf{E}}(t)}{dt} = \frac{1}{2} \left[ (\Gamma g(N_{th}) - \alpha_{int} - \alpha_m)v_g + \Gamma v_g \frac{\partial g}{\partial N} \Delta N(t) - \frac{2i\omega_{th}}{n_g} \frac{\partial n}{\partial N} \Delta N(t) \right] \vec{\mathbf{E}}(t) \quad (41)$$

At the threshold lasing condition, the cavity gain is equal to the sum of the losses in the cavity, and so the first term in brackets vanishes. Recalling that the differential gain rate is  $\xi = v_g \partial g / \partial N$ , the E-field rate equation can be simply written as

$$\frac{d\vec{\mathbf{E}}(t)}{dt} = \frac{1}{2} \left[ \Gamma \xi - \frac{2i\omega_{th}}{n_g} \frac{\partial n}{\partial N} \right] \Delta N(t) \vec{\mathbf{E}}(t) \quad (42)$$

Finally, the substitution of  $\alpha$  as the line-width enhancement factor

$$\alpha = -\frac{2\omega}{c\Gamma} \frac{\frac{\partial n}{\partial N}}{\frac{\partial g}{\partial N}} = -\frac{\chi_p'}{\chi_p''} \quad (43)$$

as the ratio of the real and imaginary parts of the pump-induced susceptibility,  $\chi_p'$  and  $\chi_p''$  respectively, the E-field rate equation can be written as:

$$\frac{d\vec{\mathbf{E}}(t)}{dt} = \frac{1}{2}(1 + i\alpha)\Gamma\xi\Delta N(t)\vec{\mathbf{E}}(t) \quad (44)$$

Equations (22) and (44) represent the set of coupled rate equations for the semiconductor laser diode without feedback. It should be noted that these equations are only valid if the E-field undergoes small variations within a round-trip time ( $\approx 2$  ps) of the laser cavity. In the next section the necessary feedback terms are added to account for the delayed phase conjugate feedback from an externally pumped phase conjugating mirror.

## 2.2 Rate Equations with Phase Conjugate Feedback

The phase conjugate term stated earlier can be used directly with a slight modification to account for the time lag between the E-field leaving the laser cavity, and re-entering the cavity after being reflected from the PCM,

$$\tau = \frac{2L_{ext}}{c} \quad (45)$$

where  $L_{ext}$  is the length of the external cavity formed by the laser and the PCM. Adding the phase conjugate term to the rate equations gives the full coupled rate equations for the E-field and electron-hole number inside the laser diode cavity coupled to an external phase conjugating cavity:

$$\frac{d\vec{\mathbf{E}}(t)}{dt} = \frac{1}{2}(1 + i\alpha)\Gamma\xi\Delta N(t)\vec{\mathbf{E}}(t) + \kappa\vec{\mathbf{E}}^*(t - \tau) \exp\left\{i\phi_{PCM} + i2\Delta\omega\left(t - \frac{\tau}{2}\right)\right\} \quad (46)$$

$$\frac{d\Delta N(t)}{dt} = (p-1)\frac{N_{th}}{\tau_N} - \frac{\Delta N(t)}{\tau_N} - \left[ \frac{\Gamma_o}{\Gamma} + \xi\Delta N(t) \right] |\vec{\mathbf{E}}|^2 \quad (47)$$

where the feedback rate,  $\kappa$ , describes the rate ( $s^{-1}$ ) of coupling reflected photons back into the laser cavity

$$\kappa = \frac{\eta_c(1-R_2)}{\tau_{in}} \left( \frac{R_{PCM}}{R_2} \right)^{1/2} \quad (48)$$

and  $\eta_c$  is a coupling loss term. The frequency change in the conjugate beam due to nondegenerate pump beams ( $\omega_p$ ) in a nondegenerate four wave mixing phase conjugate mirror is  $\Delta\omega = \omega_p - \omega$ . Since the degenerate case is used in this research,  $\Delta\omega = 0$ , but is kept for generality.

As stated earlier chaotic behavior requires systems to have dimension three or higher. It is convenient to split the complex E-field rate equation into independent terms for the normalized amplitude  $P(t) = |\vec{\mathbf{E}}(t)|^2$  and phase  $\phi(t)$ . The final set of coupled rate equations with feedback are:

$$\frac{dP(t)}{dt} = \Gamma\xi\Delta N(t)P(t) + 2\kappa\sqrt{P(t)P(t-\tau)} \cos \left[ \phi(t-\tau) + \phi(t) + \phi_{PCM} + 2\Delta\omega(t - \frac{\tau}{2}) \right] \quad (49)$$

$$\frac{d\phi(t)}{dt} = \frac{1}{2}\alpha\Gamma\xi\Delta N(t) - \kappa\sqrt{\frac{P(t-\tau)}{P(t)}} \sin \left[ \phi(t-\tau) + \phi(t) + \phi_{PCM} + 2\Delta\omega(t - \frac{\tau}{2}) \right] \quad (50)$$

$$\frac{d\Delta N(t)}{dt} = (p-1)\frac{N_{th}}{\tau_N} - \frac{\Delta N(t)}{\tau_N} - \left[ \frac{\Gamma_o}{\Gamma} + \xi\Delta N(t) \right] |P(t)|^2. \quad (51)$$

### 2.3 Regions of Laser Operation

The roadmap for investigating the nonlinear dynamics of the coupled rate equations involves finding the steady state solutions, performing a linear stability analysis and examining the solutions as the feedback level is increased. The eigenvalues for the system can either be real or a complex conjugate pair. A real eigenvalue that is identically = 0 (Fold bifurcation) implies that the overall phase of the laser output is indeterminate which is typical for feedback with a normal dielectric mirror (normal

feedback). In normal feedback cases, the phase of the laser is strongly dependent on the placement of the feedback mirror and small variations in the external cavity length can cause the phase to vary wildly. When a fold bifurcation occurs the laser is actually mode hopping from one eigenvalue to another giving the appearance that the laser is exiting chaos to a stable state. For PCF, a real eigenvalue of  $\lambda = 0$  does not occur. It will be shown later that a laser with PCF will phase lock and be completely deterministic even for small amounts of feedback. For the situation of a complex conjugate pair of eigenvalues, a Hopf bifurcation occurs when the real part is equal to zero as it switches from negative (damped) to positive (undamped). The imaginary part of the eigenvalue gives the new frequency of oscillation undamping at this instability which amplitude modulates the lasing frequency.

Table 5. With increasing feedback, the laser output can be categorized into five different levels of chaotic development.

Level I	Initial reduction of laser linewidth
Level II	Relaxation oscillations become undamped
Level III	Excitation of external cavity modes
Level IV	Significant broadening of laser linewidth, Chaos
Level V	Linewidth narrows and remains narrow for further increases in feedback

The main focus of this research is the dynamics of the laser leading up to, but not entering, chaotic activity. It has been widely accepted that a chaotic system can be categorized into five characteristic levels of chaotic development. The first of these levels, Level I, is identified by an initial reduction in the laser linewidth, which typically occurs with feedback levels  $< 0.1\%$  of the laser output. As the optical feedback is increased, Level II is reached when relaxation oscillations become undamped and begin to appear in the frequency spectrum. Further increases in the feedback causes the laser to enter Level III and are marked by the excitation of external cavity modes. At Level IV, sometimes called coherence collapse or chaos, the laser linewidth broadens significantly from a few MHz to several GHz. Finally, Level V is reached when the laser exits out of chaos with a reduced linewidth, similar

to Level I. Level V is different from Level I in that it needs extremely strong feedback levels and usually requires the exit facet of the diode to be anti-reflection (AR) coated to increase the coupling of the feedback beam into the laser cavity. Table 5 summarizes the five levels. In this research Levels I, II, and III are investigated in detail.

### III. Mathematical Analysis

The three coupled time-delayed differential equations presented at the end of the previous chapter are extremely difficult to analyze analytically. This chapter discusses the mathematical techniques and approximations that are used to find solutions to the equations. The analytical approximations made in this chapter will be revisited in the discussion of the experimental results in order to check the validity of the approximations. In addition to the analytical tools presented here, two computer models that numerically evaluate the three coupled equations are introduced in the next chapter.

#### 3.1 Scaling

To perform numerical analysis and computer modeling on the three coupled nonlinear Eqs. (49)-(51), it is beneficial to carry out a scaling to non-dimensionalize the equations. The scaling used in this research is the same as Gavrielides *et al* (9) which gives:

Time normalization to the photon life time:  $s = t/\tau_p$

Feedback normalization:  $\eta = \kappa\tau_p$

Carrier decay time normalization:  $T = \tau_N/\tau_p$

Field normalization:  $A = E/\sqrt{\Gamma\xi}$

Carrier Normalization:  $\hat{N} = \frac{1}{2}\Gamma\xi\Delta N\tau_p$

The resulting equations with the new normalized parameters are:

$$\frac{da}{ds} = a\hat{N} + \eta a(s - \tau) \cos [\phi(s - \tau) + \phi(s) + \phi_{PCM} + 2\Delta\omega(s - \tau/2)] \quad (52)$$

$$\frac{d\phi}{ds} = \alpha\hat{N} - \eta \frac{a(s - \tau)}{a(s)} \sin [\phi(s - \tau) + \phi(s) + \phi_{PCM} + 2\Delta\omega(s - \tau/2)] \quad (53)$$

$$T \frac{d\hat{N}}{ds} = \mathcal{P} - \hat{N} - (1 + 2\hat{N})a^2 \quad (54)$$

where  $A(s) = a(s)e^{i\phi(s)}$ ,  $\tau$  has been normalized with  $\tau_p$  and  $\mathcal{P} = (p - 1)N_{th}$  is the amount of pumping above threshold. For the experiments, the totally degenerate condition  $\Delta\omega = 0$  is used but  $\Delta\omega$  is retained here for generality.

### 3.2 Steady State Solutions

A common technique for examining the behavior of the system is to look in the steady state where all derivatives can be set to zero and examine the solutions and the behavior of the system. Substituting the steady state values for  $a$ ,  $\hat{N}$  and  $\phi$ :

$$a = a_s \quad \hat{N} = \hat{N}_s \quad \phi = \hat{\omega}t + \phi_s \quad (55)$$

where  $a_s$ ,  $\hat{N}_s$  and  $\phi_s$  are all constants and  $\hat{\omega}$  is the angular frequency of the laser measured relative to the solitary frequency  $\omega$ , yields the solution

$$\begin{aligned} \hat{\omega} &= \Delta\omega \\ &= 0 \text{ for degenerate PCF.} \end{aligned} \quad (56)$$

This simple equation indicates that the relative frequency  $\hat{\omega}$  is identical to the frequency difference between the pump beam and the solitary laser. In other words, it shows that the laser locks to the frequency of the pump beam of the phase conjugator. This condition offers a unique ability of the PCM to adjust the lasing frequency through adjustments of the pump frequency. A similar adjustment of the laser frequency with normal feedback is not possible. In addition to the frequency locking condition given above, we also have

$$\hat{\omega} = -\eta\sqrt{1 + \alpha^2} \sin(\vartheta + \arctan(\alpha)) \quad (57)$$

where  $\vartheta = 2\phi_s + \phi_{PCM}$ . This solution imposes phase locking of the laser. Notice that this solution is independent of  $\tau$  which is also a major change from the case of the normal mirror. For a normal mirror the phase is a strong function of the delay time  $\tau$  and therefore minor changes in the external cavity length can adversely affect the phase. By using phase conjugation, the  $\tau$  dependence is eliminated and Eq. (57) requires the phase of the laser to lock to a constant value set by the conjugate mirror  $\phi_{PCM}$ , the material parameter  $\alpha$ , and the feedback strength  $\eta$ . From this equation, it is clear that the solution for  $\vartheta$  only exists for  $|\hat{\omega}| \leq (\eta\sqrt{1+\alpha^2})$ , where only the positive slope is stable. This equality describes the fold bifurcation line in the  $(\eta, \hat{\omega})$  plane. Figure 9 shows the graphical solution to Eq. (57) and the saddle-node bifurcation lines dividing the space into three regions. Points below the straight lines fall into the region of periodic solutions which have been associated with four-wave mixing (FWM) solutions. Solutions above the bifurcation lines are the phase and frequency locked solutions given by Eq. (57). The relevant parameters and a MathCad<sup>1</sup> template for the figure can be found in Appendix A.

Taking into account the restrictions given by the inequality, the solutions for  $\vartheta$  are:

$$\vartheta = -\arctan(\alpha) - \arcsin\left(\frac{\hat{\omega}}{\eta\sqrt{1+\alpha^2}}\right) + 2n\pi \quad n = 0, 1, 2, \dots \quad (58)$$

for the nodes, and

$$\vartheta = -\arctan(\alpha) - \arcsin\left(\frac{\hat{\omega}}{\eta\sqrt{1+\alpha^2}}\right) + (2n+1)\pi \quad n = 0, 1, 2, \dots \quad (59)$$

for the saddles. These solutions are also shown graphically in Figure 9a.

In addition, the steady state electron-hole number and photon number are

$$\hat{N}_s = -\eta \cos \vartheta \quad (60)$$

---

<sup>1</sup>MathCad is a registered trademark of MathSoft

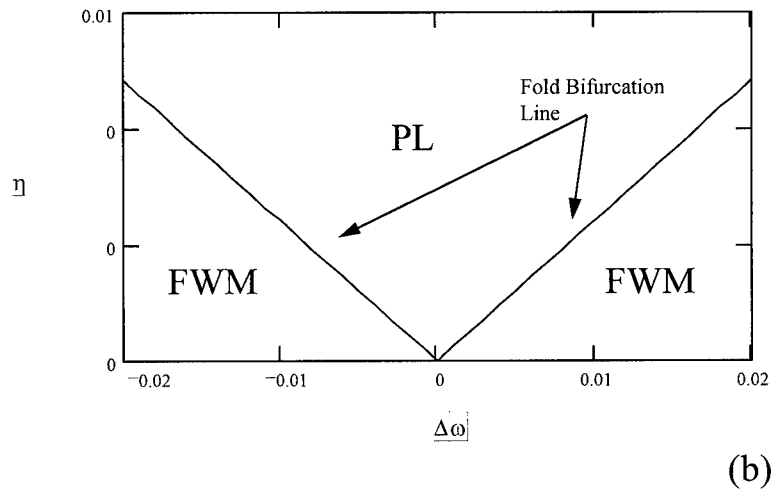
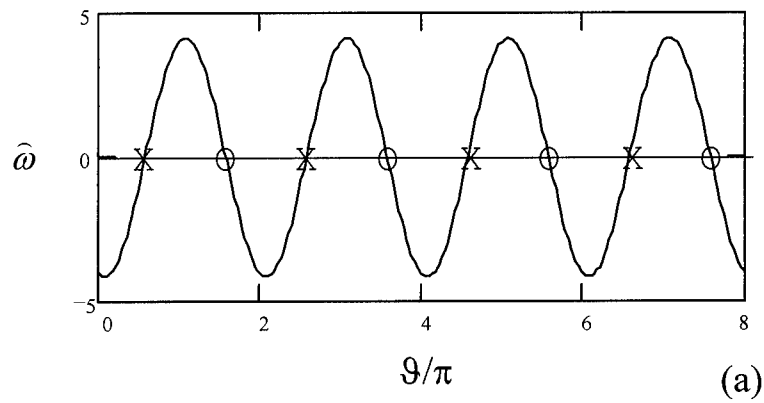


Figure 9. (a) Graphical solution of Eq. (57) showing the stable ( $\times$ ) and unstable ( $\circ$ ) solutions. (b) For a given solution of  $(\eta, \hat{\omega})$ , the fold bifurcation lines can be found as a function of feedback,  $\eta$ . PL is the phase locked region and the area below the fold bifurcation line represents unstable periodic solutions.

$$a_s = \left( \frac{\mathcal{P} + \eta \cos \vartheta}{1 - 2\eta \cos \vartheta} \right)^{\frac{1}{2}} \quad (61)$$

The numerator in Eq. (61) represents the net rate of electron-holes between pumping,  $\mathcal{P}$ , and the steady state population difference  $\hat{N}_s$ . The denominator is related to the stimulated emission gain given in Eq. (21) for emission of photons due to stimulated emission. The effect of the feedback is to change the threshold gain rate of the laser,  $G = 1 - 2\eta \cos \vartheta$ , with the sign of  $\cos \vartheta$  being the dominant factor. In particular, the threshold gain is reduced for  $|\vartheta| < \pi/2$  with the strongest reduction occurring when  $\vartheta = 0$  or  $\Delta\omega = -\eta\alpha$ . This condition is unique to non-degenerate phase conjugation where the difference between the pump and probe frequencies can be adjusted to meet the  $\Delta\omega = -\eta\alpha$  requirement. For example, given typical values of  $\eta = 0.012$  and  $\alpha = 4$ , a separation of the pump and probe frequencies by 1.836 GHz would produce the lowest threshold gain,  $G = 1 - 2\eta$ . Thus, operating at this point, the laser with a non-degenerate phase conjugate mirror would extract the optimum gain from lasing medium since the gain threshold is reduced to the minimum level. Of course, this also implies that for other phase conjugate configurations where  $\Delta\omega \neq -\eta\alpha$ , and particularly for the degenerate case,  $\Delta\omega = 0$ , the phase of the laser will not operate at the point of lowest threshold gain, but rather at a point yielding the smallest line width (1)(17)(20).

### 3.3 Steady State Stability

It was stated earlier that the steady state solutions to the coupled nonlinear equations were independent of  $\tau$  for the phase conjugate case. Although the steady state solutions may be independent of the external cavity, the stability of these solutions could depend on  $\tau$ . To investigate the sensitivity of the steady state solution to small perturbations, a linear stability analysis can be performed on the rate equations by linearizing around their steady state values and assuming a time dependence of the form  $\exp(s\tau)$ . The result is a secular determinant equation whose solutions,

$D(s) = 0$ , yields the time dependent behavior of the perturbation:

$$D(s) = [Ts + (1 + 2a_s^2)][s^2 + 2\eta s \cos \vartheta + \eta^2(1 - e^{-2s\tau})] \\ + 2(\mathcal{P} + \eta \cos \vartheta)[s + \eta\sqrt{1 + \alpha^2} \cos(\vartheta + \arctan(\alpha))(1 + e^{-s\tau})] \quad (62)$$

From the fold bifurcation lines in Figure 9, it is easily identified that the fold bifurcation for the totally degenerate case occurs for zero feedback,  $\eta = 0$ . Since this point offers no additional information, it is the Hopf bifurcation point that is of interest for the dynamics of the laser for degenerate phase conjugate feedback. At the Hopf point, the real part of the complex pair of roots of Eq. (62) passes from negative to positive values and is set to zero. Substituting  $s = i\Omega$  into Eq. (62) and separating the real and imaginary parts gives two equations for the feedback level  $\eta$ , and the frequency  $\Omega$  of the resulting periodic solution

$$-\Omega[2\eta\Omega \cos \vartheta + \eta^2 \sin 2\Omega\tau] + \epsilon \frac{1 + 2\mathcal{P}}{1 - 2\eta \cos \vartheta} [\eta^2(1 - \cos 2\Omega\tau) - \Omega^2] + \\ 2\epsilon(\mathcal{P} + \eta \cos \vartheta)\eta\sqrt{1 + \alpha^2} \cos(\vartheta + \arctan(\alpha))(1 + \cos \Omega\tau) = 0 \quad (63)$$

and

$$\epsilon \frac{1 + 2\mathcal{P}}{1 - 2\eta \cos \vartheta} [2\eta\Omega \cos \vartheta + \eta^2 \sin 2\Omega\tau] + \Omega[\eta^2(1 - \cos 2\Omega\tau) - \Omega^2] + \\ 2\epsilon(\mathcal{P} + \eta \cos \vartheta)[\Omega - \eta\sqrt{1 + \alpha^2} \cos(\vartheta + \arctan(\alpha)) \sin \Omega\tau] = 0 \quad (64)$$

where  $\epsilon = 1/T$ . At this point these two equations must be solved with a nonlinear root finder to find exact solutions, or approximations must be made so that analytical solutions can be found.

Nonlinear behavior of systems at the Hopf bifurcation point provides insight into the magnitude of  $\Omega$  and  $\eta$ . Typically the frequency emerging out of the Hopf bifurcation is close to the relaxation frequency of the system or one of its harmonics. In addition, from the behavior of Eqs. (63) and (64) the combination of  $\Omega\tau$  must be

$O(1)$ . Furthermore,  $\eta$  is typically small and is  $O(\epsilon)$ . This leads to an appropriate scaling of

$$\Omega = \epsilon^{1/2}\sigma \quad \tau = \epsilon^{-1/2}\Theta \quad \eta = \epsilon E \quad (65)$$

where  $\sigma$ ,  $\Theta$ , and  $E$  are all  $O(1)$ . Substitution into Eq. (63) and (64) leads to a solution for the feedback and frequency at the Hopf point in the limit as  $\epsilon \rightarrow 0$  (9)

$$\eta_H = \frac{\epsilon(1 + 2\mathcal{P})}{2[\sqrt{1 + \alpha^2} \cos(\vartheta + \arctan(\alpha)) \cos^2(\sqrt{2\mathcal{P}}\Theta/2) - \cos \vartheta]} + O(\epsilon^{3/2}) \quad (66)$$

and

$$\Omega_H = \epsilon^{1/2}\sqrt{2\mathcal{P}} - \epsilon \frac{(1 + 2\mathcal{P})\sqrt{1 + \alpha^2} \cos(\vartheta + \arctan(\alpha)) \sin(\sqrt{2\mathcal{P}}\Theta)}{4[\sqrt{1 + \alpha^2} \cos(\vartheta + \arctan(\alpha)) \cos^2(\sqrt{2\mathcal{P}}\Theta/2) - \cos \vartheta]} + O(\epsilon^{3/2}) \quad (67)$$

where the lowest order in  $\epsilon$  is the most dominant term and  $\Omega_H$  is the relaxation frequency that emerges from the Hopf bifurcation.

Gavrielides pointed out that this perturbation expansion leading to Eqs. (66) and (67) fails when  $\cos(\sqrt{2\mathcal{P}}\Theta/2)$  approaches 0 which occurs at the resonant points of  $\Omega\tau = (2n + 1)\pi$  or

$$\frac{\Omega_H}{\omega_{ext}} = \left(n + \frac{1}{2}\right) \quad n = 0, 1, 2, \dots \quad (68)$$

Equation (68) is the condition for frequency locking between the relaxation oscillation and external cavity frequency  $\omega_{ext}$  with the locking ratio being  $(n + \frac{1}{2})$ . Equations (67) and (68) also show that when the Hopf frequency equals the solitary relaxation frequency of the laser,  $\Omega_H = \omega_R$ , the external cavity length ( $\tau$ ) falls in the middle of the locking region for adjacent  $n$ .

An additional simplification that can be used is the case of  $\alpha \rightarrow \infty$ . This condition has been extensively examined and is well understood with externally

injected laser systems and offers a more compact form for  $\eta_H$  and  $\Omega_H$ :

$$\eta_H = \frac{1 + 2\mathcal{P}}{2\mathcal{P}} \frac{\omega_R}{2 \cos^2\left(\frac{\omega_R \tau}{2}\right)} \quad (69)$$

and

$$\Omega_H = \omega_R \left( 1 - \frac{1 + 2\mathcal{P}}{4\mathcal{P}} \omega_R \tan\left(\frac{\omega_R \tau}{2}\right) \right) \quad (70)$$

where  $\omega_R = \sqrt{(2\mathcal{P})/T}$  is the scaled relaxation frequency of the solitary laser. These two equations provide a look into the behavior of both  $\eta_H$  and  $\Omega_H$  as the external cavity length is varied. Figure 10 shows both functions over a range of  $L_{ext} = 18\text{--}28$  cm. The unbounded behavior of the functions is due to the lack of a loss mechanism in the system and the fact that these equations are only valid in the non-resonance lengths. The measured resonant peaks from the experimental data will be bounded by inherent loss mechanisms and most likely will have lower magnitudes. Nonetheless, the general behavior provides an excellent preview of the expected behavior for  $\eta_H$  and  $\Omega_H$ .

The analytical techniques and approximations presented in this chapter offer one method of analyzing the set of three nonlinear equations. The next chapter discusses the computer models which numerically evaluate the equations to find steady state solutions. The computer models have been developed to simulate the development of chaotic behavior of the laser diode and are used interpret the experimental data.

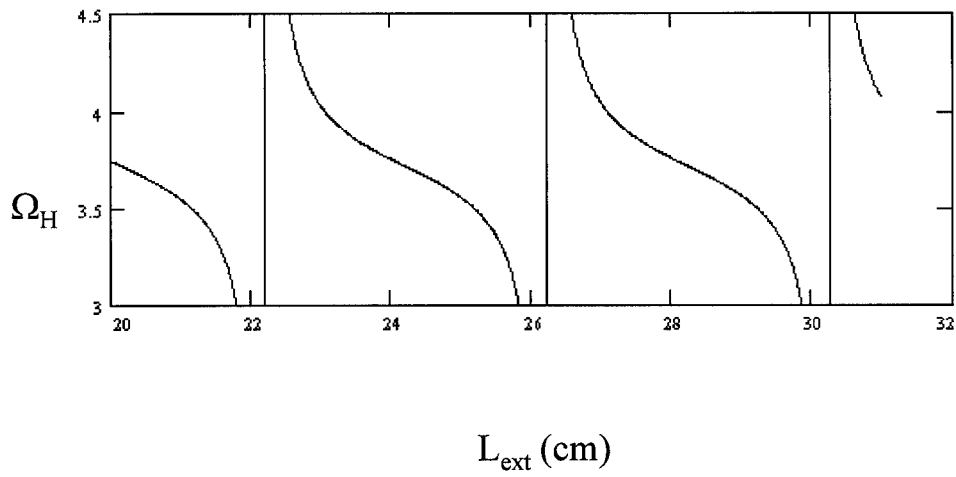
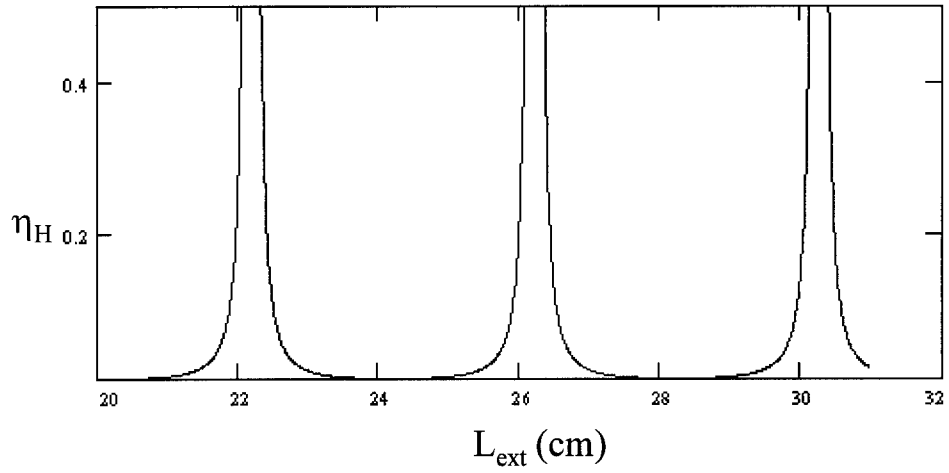


Figure 10. Plots of Eqs. (69) and (70) showing the resonance in  $\eta_H$  and  $\Omega_H$  for typical experimental external cavity lengths.

## *IV. Computer Modeling of the Phase Conjugate Feedback*

The previous chapter provided insight into the necessity of using computer modeling to examine the nonlinear behavior of time-delayed coupled differential equations. Computer modeling provides an alternative to analytical solutions without making approximations, other than the basic assumptions leading to Eqs. (52)–(54). This chapter contains a brief discussion of the two models used in support of this research. The models were developed by the Nonlinear Optics Center, Phillips Laboratory, Kirtland Air Force Base, New Mexico.

### *4.1 Bifurcation Model*

The LKCONBI2.C model integrates the Lang-Kobayashi (L-K) phase conjugate equations to produce a listing of data points which can be plotted to form bifurcation diagrams. A copy of the C-source code is included in Appendix B. Inputs to the model include external cavity length, beginning and ending values of feedback, laser pumping above threshold, linewidth enhancement parameter, and lifetime ratio  $T$ . The scaling used in the model is the same as presented in Section 3.1.

One minor change to the original LKCONBIF.C program was made to move the user input parameters to a separate input file. This was done primarily to avoid compiling the source code for multiple changes in the input parameters and to incorporate additional non-scaled experimental parameters such as measured relaxation oscillation frequency and external cavity length. A listing of all the input parameters is shown in Table 6.

The LKCONBI2 program actually contains two separate models: the evaluation of the full L-K rate equations presented in Eqs. (52)–(54) and the evaluation of the Phillips Laboratory's phase equation (3). The user may select, via an input parameter, which model to evaluate. Both operate the same throughout the program,

Table 6. Input parameters contained in a separate ASCII file for the LKCONBI2 model.

Variable Name	Purpose
BEGIN	Beginning integration time
END	Ending integration time
EXTIME	Time when steady-state begins
NPOINTS	Number of point to use in integration
KMAX	Integration resolution magnifier
HTAMIN	Minimum feedback level
HTAMAX	Maximum feedback level
HTASTEP	Number of steps between max and min feedback
pi	Pumping level above threshold
alpha	Linewidth enhancement factor
ext_length	Unscaled external cavity length (cm)
delta	Scaled frequency offset from solitary laser
phipcm	Phase shift due to PCM
photon_life	Unscaled photon lifetime (sec)
carrier_life	Unscaled carrier lifetime (sec)
model	1=full-up equations, 0=phase equation
Y	Gain saturation term

except for the equation(s) used in the integration routine. For simplicity, the full rate equation option will be discussed below.

The model begins by dividing the full range of feedback specified by the user into feedback steps,  $(HTAMAX-HTAMIN)/HTASTEP$ . Increasing the value of HTASTEP provides more detail in the bifurcation diagrams but also increases the run-time of the model. Typical values of HTASTEP are 50 to 100. Small values of HTASTEP are not recommended since bifurcation points could be missed with too large a step size. For each step of the feedback parameter, a time series of the system is reconstructed using a fourth-order Runge-Kutta integration routine on the set of normalized differential equations, Eqs. (52) - (54). The delayed values of the amplitude, phase and carrier number needed by the equations are handled by establishing a circular stack in memory, whose length is four times the normalized external cavity round-trip delay,  $\tau$ . An index into the stack is used to retrieve the

proper values and the stack is initialized with zeros so that the feedback does not take effect until at least one round trip in time  $\tau$  has been completed. The factor of four in the stack size is to account for the fourth-order integration routine which needs a delayed value for each integration step.

Extrema of the amplitude are not saved until the user-established steady state time, `EXTIME`, has elapsed. This allows transients in the time series to diminish and steady state conditions recorded. During the steady state condition, when a peak in the amplitude has occurred, the feedback rate, time, amplitude and phase of the laser output are recorded in the data file. These points can then be plotted using a separate plotting program to create bifurcation diagrams. Figure 11 shows two examples of bifurcation diagrams plotting the output amplitude extrema versus feedback level. The relevant parameters for these plots are  $T = 316.1$ ,  $\alpha = 4$ , and  $\mathcal{P} = 3.0$ .

External cavity lengths can be divided into two regimes based on the value of the external cavity and relaxation frequencies. An external cavity is labeled as being short when  $\nu_{ext} > \nu_R$  while long cavities have  $\nu_{ext} < \nu_R$ . Each external cavity regime has separate characteristics which are also found into the computer models. Figure 11 shows a computed bifurcation diagram for the short cavity (a) and long cavity (b). The main differences between the short and long regimes occurs at the Hopf points. In the short cavity, the bifurcation at the Hopf points is distinct indicating that only one frequency is emerging at a time. This distinction is due in part to the fact that the external cavity frequency is greater than the relaxation oscillation frequency and requires a higher  $\eta$  to undamp. The frequencies that emerge at additional Hopf points are related to the first Hopf point through a period doubling or quasi-periodicity of the relaxation frequency that has already undamped. On the other hand, the Hopf bifurcations in the long cavity, beyond the first bifurcation, are more obscured. A spectral analysis using the `LKCON2.C` model described in the next section shows that the external cavity frequency has undamped which is quickly followed by several

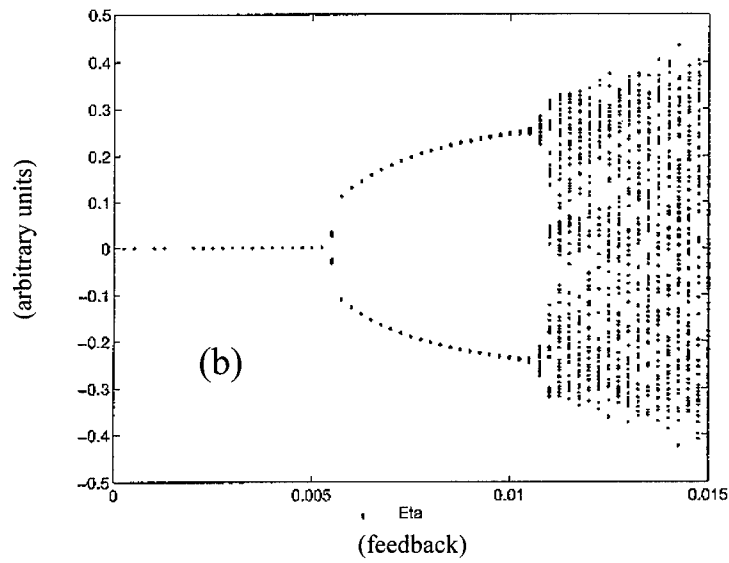
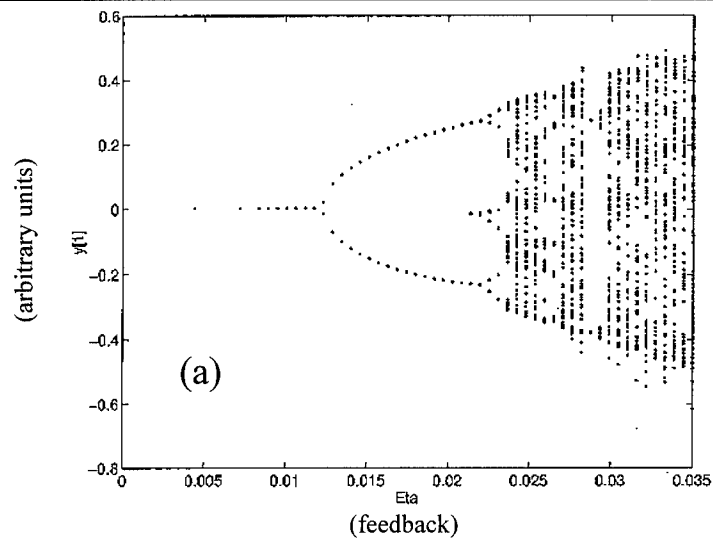


Figure 11. Bifurcation diagrams created using the LKCONBIF.C model. (a) Short external cavity with  $\tau = 16$ , ext\_length = 1.0 cm, (b) Long external cavity with  $\tau = 640$ , ext\_length = 40 cm.

harmonics. This process then develops immediately into a chaotic state shown in the bifurcation diagram.

A direct one-to-one comparison between the bifurcation model and experimental data was not intended in this research. To produce a bifurcation plot experimentally, a data acquisition system to record the amplitude time series of the laser output would require sampling the laser amplitude at a minimum of twice the relaxation oscillation frequency. For the laser at hand,  $\nu_R \approx 3.7$  GHz at low power, so a sampling frequency of 8 GHz would be required. The data acquisition system available for the experiments had a time series measurement limit of 500 MHz and therefore, most of the experimental data consisted of RF and optical spectra.

Although the experimental equipment could not meet the fast sampling requirements to generate bifurcation diagrams, the LKCONBI2.C model was still useful in providing insight to bifurcation points and the type of route to chaos due to various changes to experimental parameters. The most effective tool for comparing theoretical and experimental data was the spectrum model discussed in the next section.

#### *4.2 Spectrum Model*

The second computer model is the LKCON2.C program whose C-source code is listed in Appendix C. This model is used to create RF and FM spectra, which can be compared to the RF spectrum analyzer and Fabry-Perot (F-P) outputs. The majority of the model is similar to the LKCONBI2.C program except that a single value for the feedback parameter is used and the number of points used in the integration routine, NPOINTS, is increased to provide a larger bandwidth in the FFT algorithm. The original Phillips Laboratory LKCON.C program was modified in a similar fashion as the LKCONBIF.C model to move the user input parameters to a separate ASCII file to simplify multiple runs of the model with different input parameters. The user input parameters are the same as those listed in Table 6 with

the addition of an extra term, *inject*, which is the feedback level where the spectra are to be calculated.

From the bifurcation diagram, the user can choose a value of the feedback to use in the LKCON2.C model. Once the integration of the nonlinear equations is complete for the feedback level, two FFTs are applied to the reconstructed time series. The first one is applied to the amplitude of the signal and gives the expected RF spectrum. The second FFT is applied to the phase term and gives the FM spectrum. Both are output in separate data files, FOURIERRF.DAT and FOURIERFM.DAT, respectively. The computed time series data is also recorded in the LKCON.DAT file. Figure 12 is an example of the RF and FM outputs of the LKCON2.C model. The bifurcation map is the same as Figure 11b and the spectra have been calculated for a feedback rate of  $\eta_{inject} = 0.0065$ . The RF spectrum shown in Figure 12b represents the external cavity frequencies and higher harmonics. This spectrum also shows peak spacings of 185 MHz and 375 MHz due to a quasi-periodicity of the external cavity frequency. Spectra similar to Figure 12b will be compared with spectra from the RF spectrum analyzer during the experimental portion of this research. The FM spectrum in Figure 12c shows the relaxation oscillation frequency at  $\pm 4.7$  GHz along with modulations from the RF surrounding  $\nu_R$  and the DC component. This type of spectrum is representative of the Fabry-Perot output in the experiments. In a latter section, the model outputs and experimental spectra are compared using RF and FM spectra for numerous external cavity lengths.

As with the bifurcation model, this model behaves differently in the short and long cavity regimes. For short cavities where  $\nu_{ext} > \nu_R$ , the spectra are consistent with period doubling routes to chaos. The dominant frequency in this case is the relaxation oscillation which quickly undamps and period doubles with increasing feedback. The external cavity frequency has little effect on the chaotic development since the feedback level required to undamp  $\nu_{ext}$  is significantly higher than the relaxation oscillation. At these large levels of feedback, the relaxation oscillation

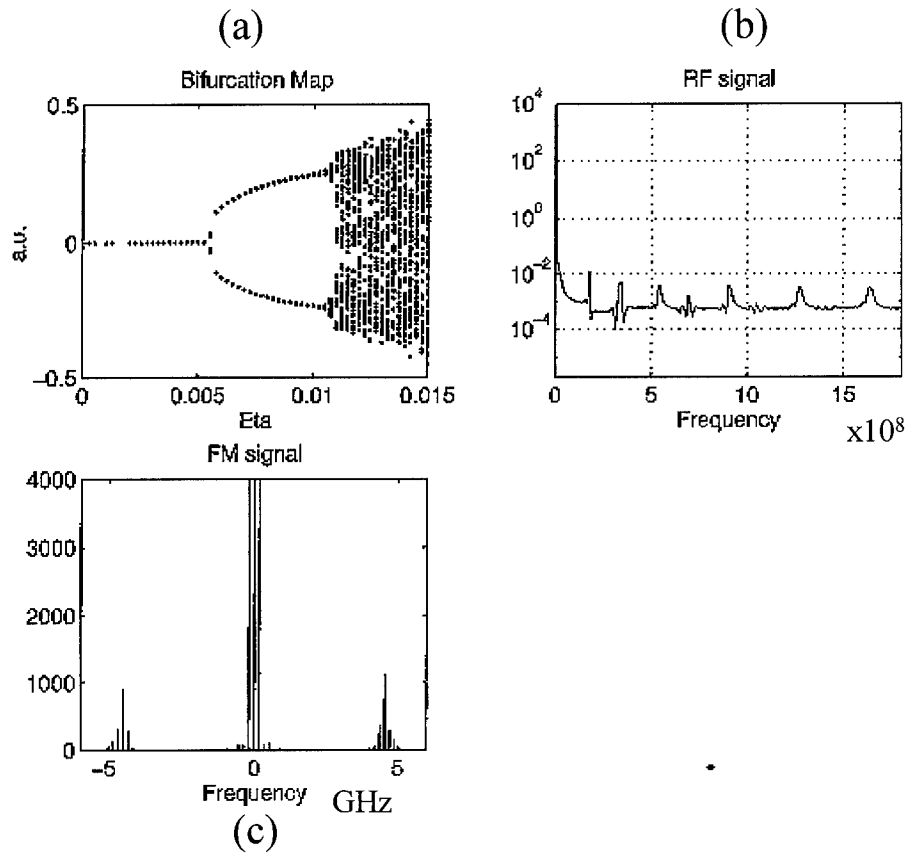
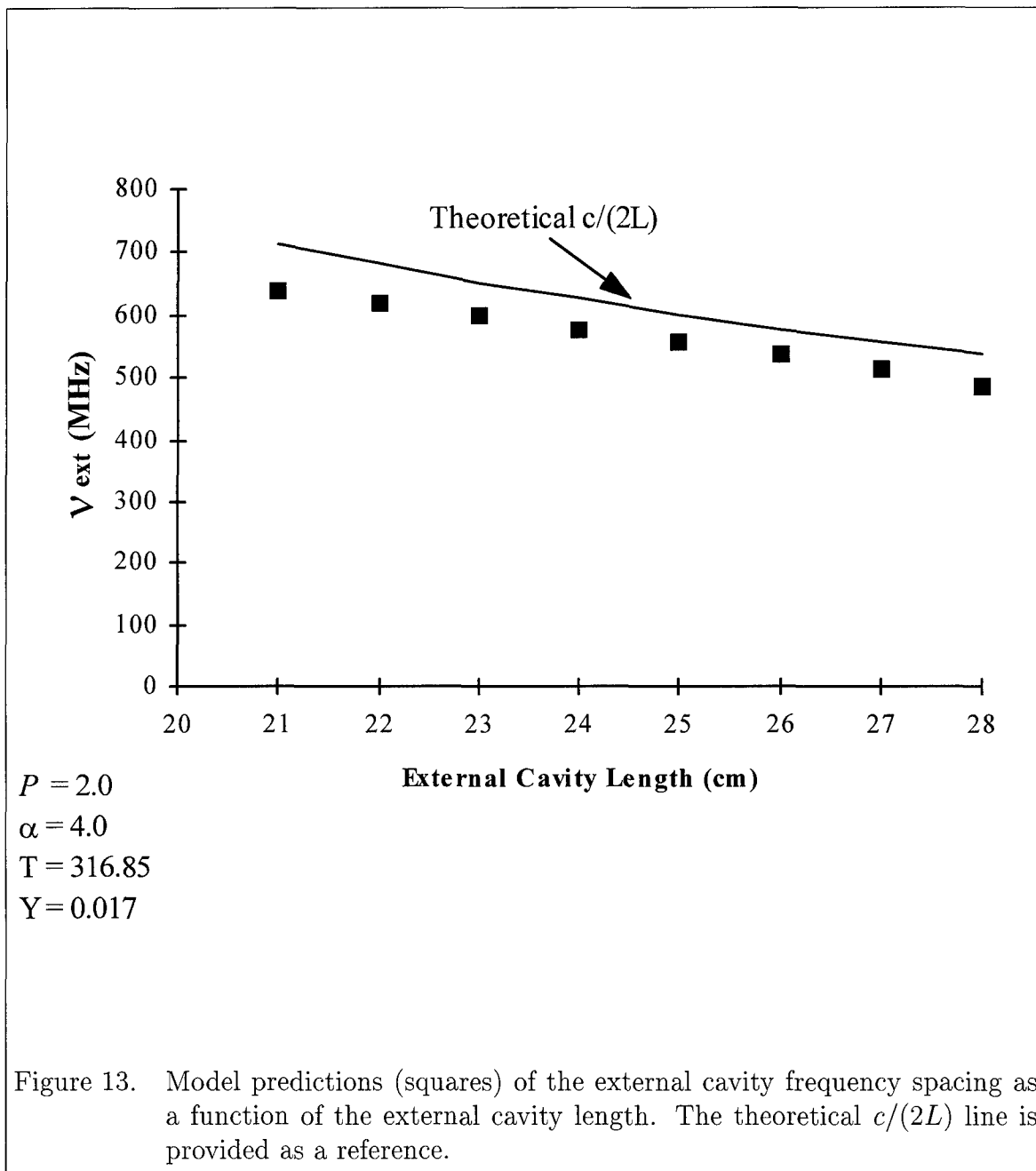


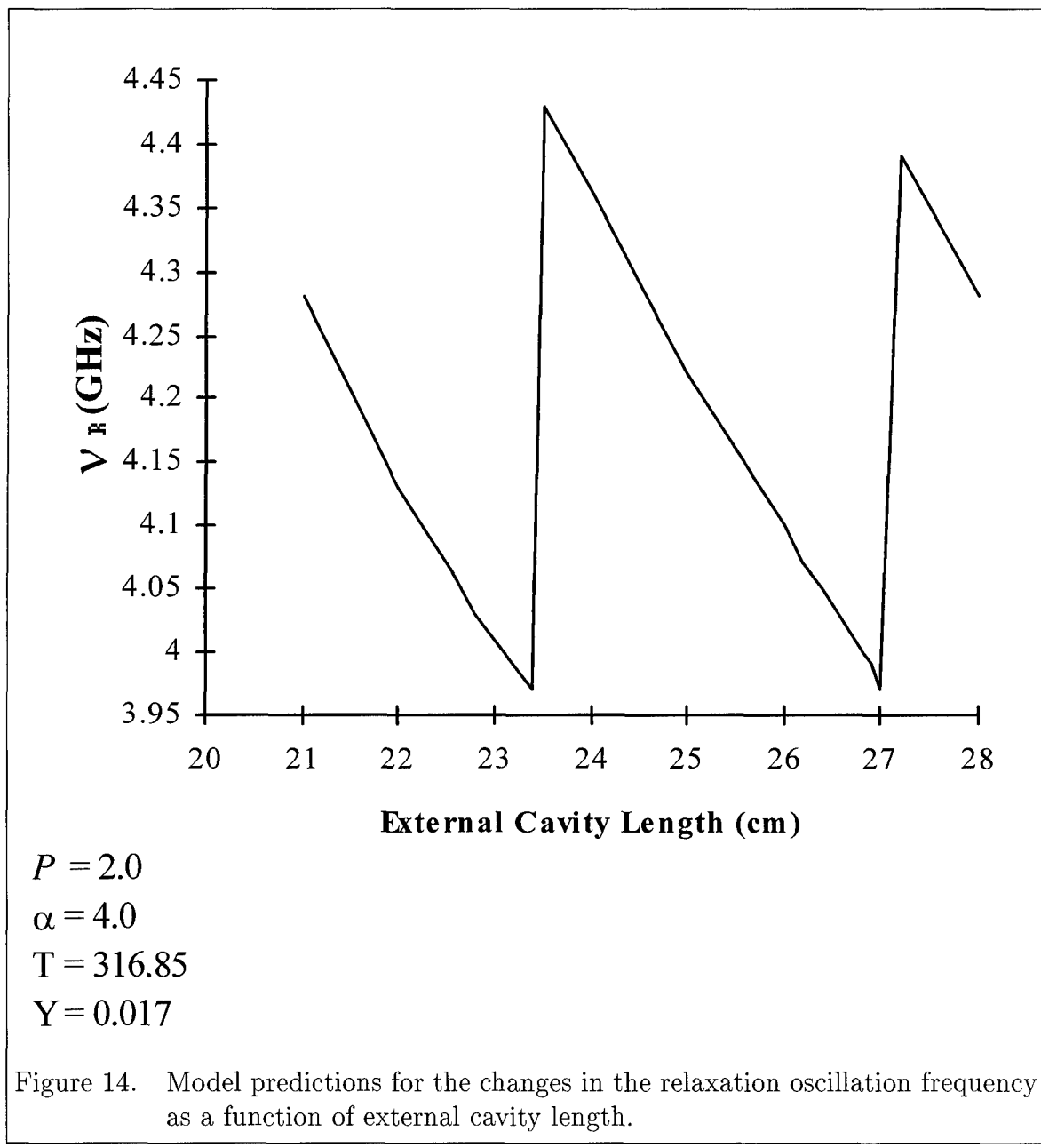
Figure 12. (a) Bifurcation diagram from Figure 11b. (b) RF spectrum of the bifurcation diagram in using the LKCON2.C model with a feedback rate of  $\eta_{inject} = 0.0065$ . The fundamental  $\nu_{ext}$  is at 180 MHz, with spacings at 185 and 375 MHz. (c) FM spectrum for the same feedback rate.  $\nu_R$  appears at  $\pm 4.7$  GHz along with modulations from the RF.

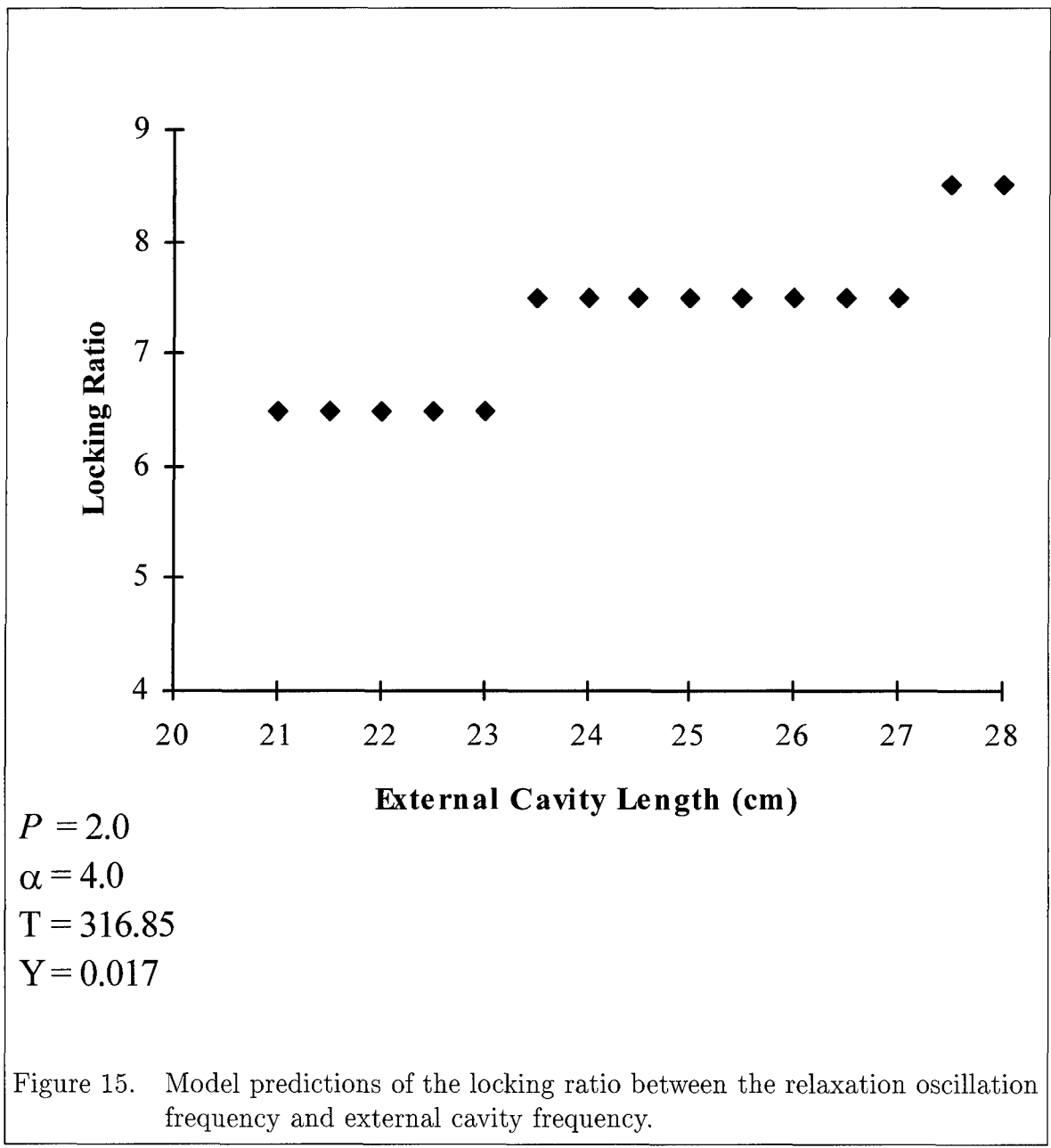
has already period-doubled many times and the laser begins to operate in Level IV, chaos. Although the short cavity region could not be directly tested experimentally, the conclusions drawn on the behavior of the model are consistent with theory and experiments using short cavities with normal dielectric mirrors and direct optical injection (24).

In the long cavity regime where  $\nu_{ext} < \nu_R$ , the model as described earlier runs into a difficulty in predicting the external cavity frequency and mode spacing. The result is an external cavity frequency that ranges from half the experimental value of  $\nu_{ext}$  for the lower end of the long cavities to one-fourth  $\nu_{ext}$  for very long cavities. This problem was investigated and found to be caused by a fundamental limitation of the model which did not include gain saturation of the laser. The model was corrected to include a Gain Saturation term,  $Y$ , which yields results that more closely agree with experimental data. The specifics of the changes made to the model are discussed in Section 6.1.

The LKCON2.C model can also be used to predict the steady state behavior of the laser and phase conjugate feedback system as a function of the external cavity length. Figures 13-15 show model predictions of the dependency of the external cavity frequency, relaxation oscillation and locking ratio as functions of external cavity length. These plots will be compared with experimental results to validate the performance of the model, as shown in Chapter VI. It is clear from these figures that the model output is representative of the trends introduced by the analytic approximations in the previous chapter.







## *V. Experimental Descriptions and Results*

The experimental portion of this research can be divided into three groups of testing. The first set of experiments characterized the solitary laser without feedback to document the operating characteristics of the Spectra Diode Laser (SDL) 5412 laser diode. In the second group of experiments, weak feedback from the CAT phase conjugate mirror geometry was applied to the laser. Measurements of the laser output due to the effects from the conjugate feedback were conducted by varying the feedback power, laser bias, and external cavity length. The final group of experiments used the double phase conjugate mirror (DPCM) geometry as the feedback mechanism and performed similar tests as with the CAT mirror for comparison. Each group of experiments is discussed in detail along with the results. This chapter is followed by an analysis of the comparison between model and experimental data.

### *5.1 Solitary Laser Characterization*

Before feedback experiments were conducted, it was necessary to measure some key characteristics of the solitary laser to see the effects due to chaos. The parameters measured in these simple experiments without feedback included lasing threshold, light-current output, nominal wavelength, and linewidth. The equipment and configuration used in this test are shown in Figure 16.

The lasing threshold was established by increasing the laser's bias current from zero mA and collecting output power measurements just after the microscope objective (MO) collimating lens. Power measurements were taken using a Newport 815 power meter and the lasing threshold was extrapolated from the point in the light-current curve where the power output suddenly increases. After threshold, the bias current was further increased in steps to its maximum value of 85 mA so that the efficiency or slope of the light-current line could be found. Figure 17 shows the

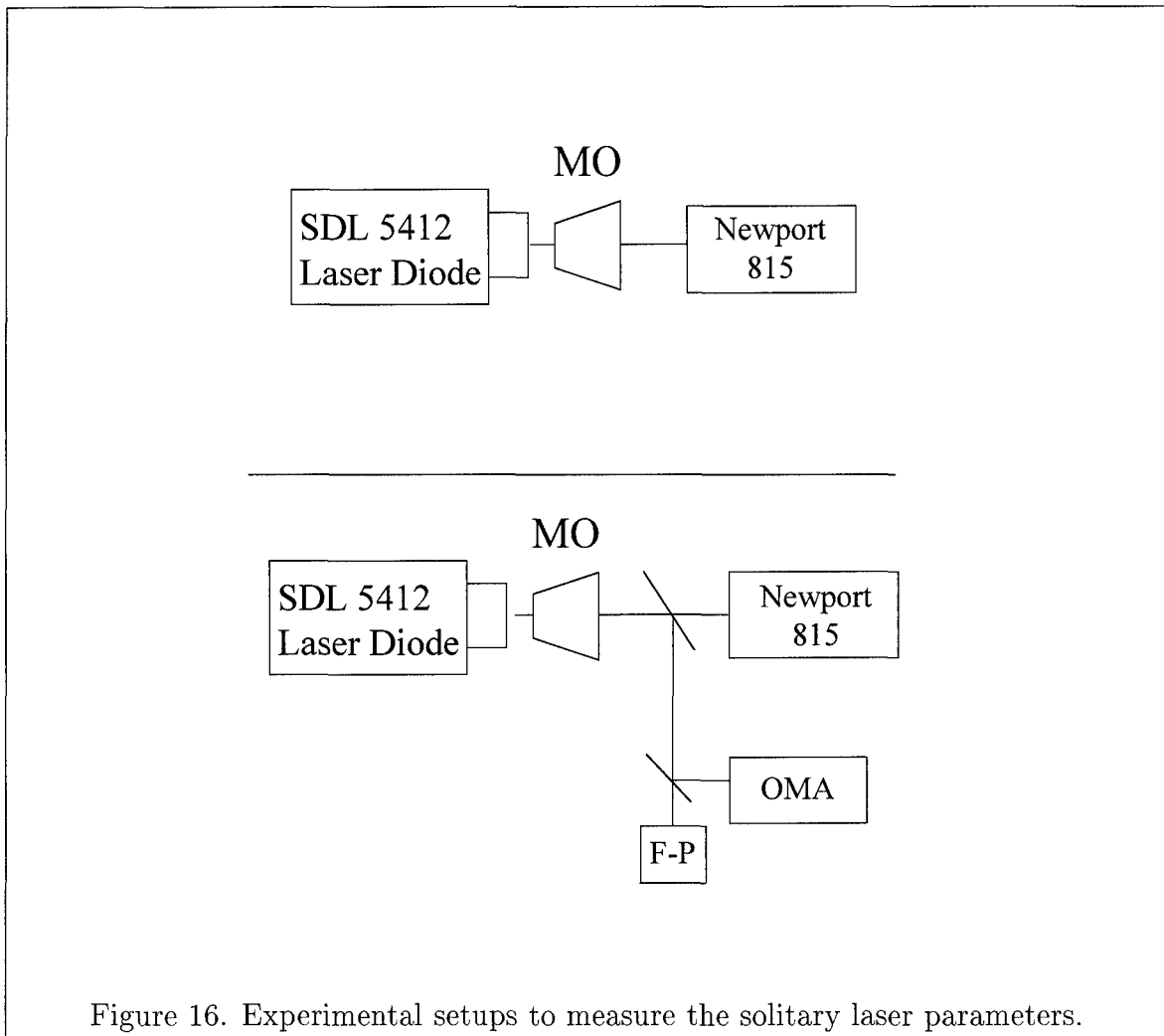


Figure 16. Experimental setups to measure the solitary laser parameters.

light-current data for the solitary laser. The extrapolated threshold current is found to be 14.92 mA with a slope efficiency of 0.93 mW/mA.

In a similar experiment, a 0.6 m monochromator and optical multichannel analyzer (OMA) combination was used to measure the center wavelength and determine if the laser was truly single mode as the bias current was varied from just past threshold to approximately three times threshold. As shown in Figure 16, at the same time the OMA was measuring the center wavelength, a F-P was used to measure the linewidth and quantify the amount of noise on the laser waveform. The main source of noise was due to current and temperature fluctuations from the power

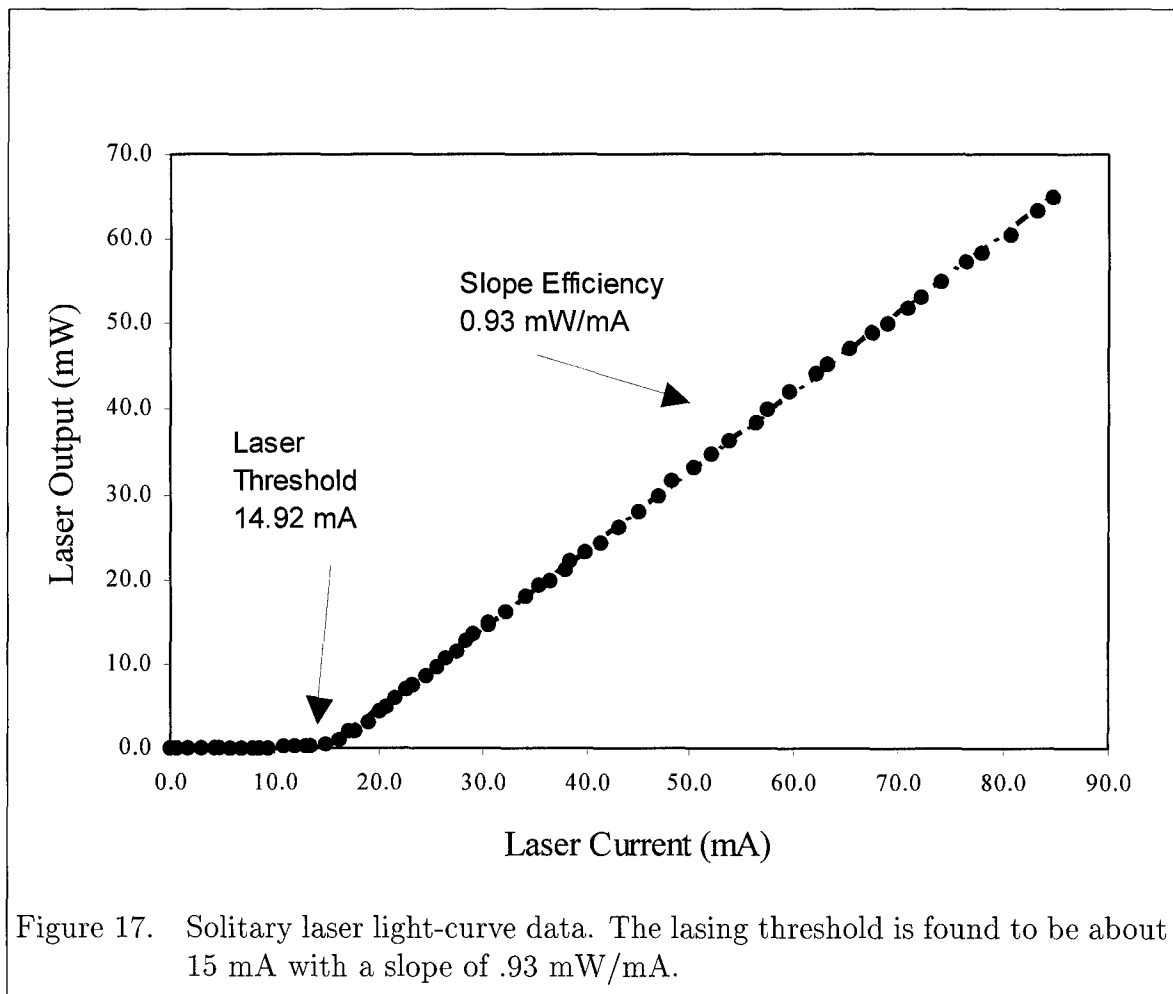


Figure 17. Solitary laser light-curve data. The lasing threshold is found to be about 15 mA with a slope of .93 mW/mA.

Table 7. Summary of the solitary laser characteristics.

Lasing threshold	14.92 mA
Light-Curve Slope	0.93 mW/mA
Nominal center wavelength (40 mA bias)	804.9 nm
Change in wavelength vs bias	0.03 nm/mA
Nominal Linewidth	135 MHz

supply which led to temporal linewidth fluctuations in the F-P display. Figures 18–20 show OMA scans of the solitary laser biased at 30, 40 and 50 mA. At a bias of 30 mA, Figure 18, the OMA shows a nominal center wavelength of 804.4 nm but also some weak peaks surrounding the main lobe. Although this small structure is not contributing a significant amount of power to the solitary laser output, it was found in later feedback experiments that these other modes become undamped. The F-P spectrum shown in Figure 21 with the laser biased at 30 mA also depicts frequencies other than the main lobe at -1.5 and -2.2 GHz. Increasing the bias current to 40 mA, Figure 19, reduces second order modes and the laser operates single mode with a center line of 804.9 nm and a nominal linewidth of 135 MHz. At a bias current of 50 mA, Figure 20, the laser is still single mode with a center wavelength 805.1 nm. Because of the uncertainty of single mode operation for laser bias currents below 40 mA, the feedback experiments described in the next several sections were conducted at biases of 40 and 45 mA, or 2.6x and 3x threshold. Table 7 summarizes the characteristics of the solitary laser.

### 5.2 Self-Pumped Phase Conjugate Feedback

Figure 22 shows the experimental setup for investigating the laser dynamics using the CAT geometry as the feedback mirror. The major components of this configuration were a SDL 5412 single mode laser diode (LD) and the self-pumped phase conjugate mirror created by a 2400 ppm Rh-doped BaTiO<sub>3</sub> crystal. The laser output was collimated using a 20X (8 mm focal length) microscope objective then immediately split with a 50/50 BK-7 non-polarizing beam splitter (BS). The reflected

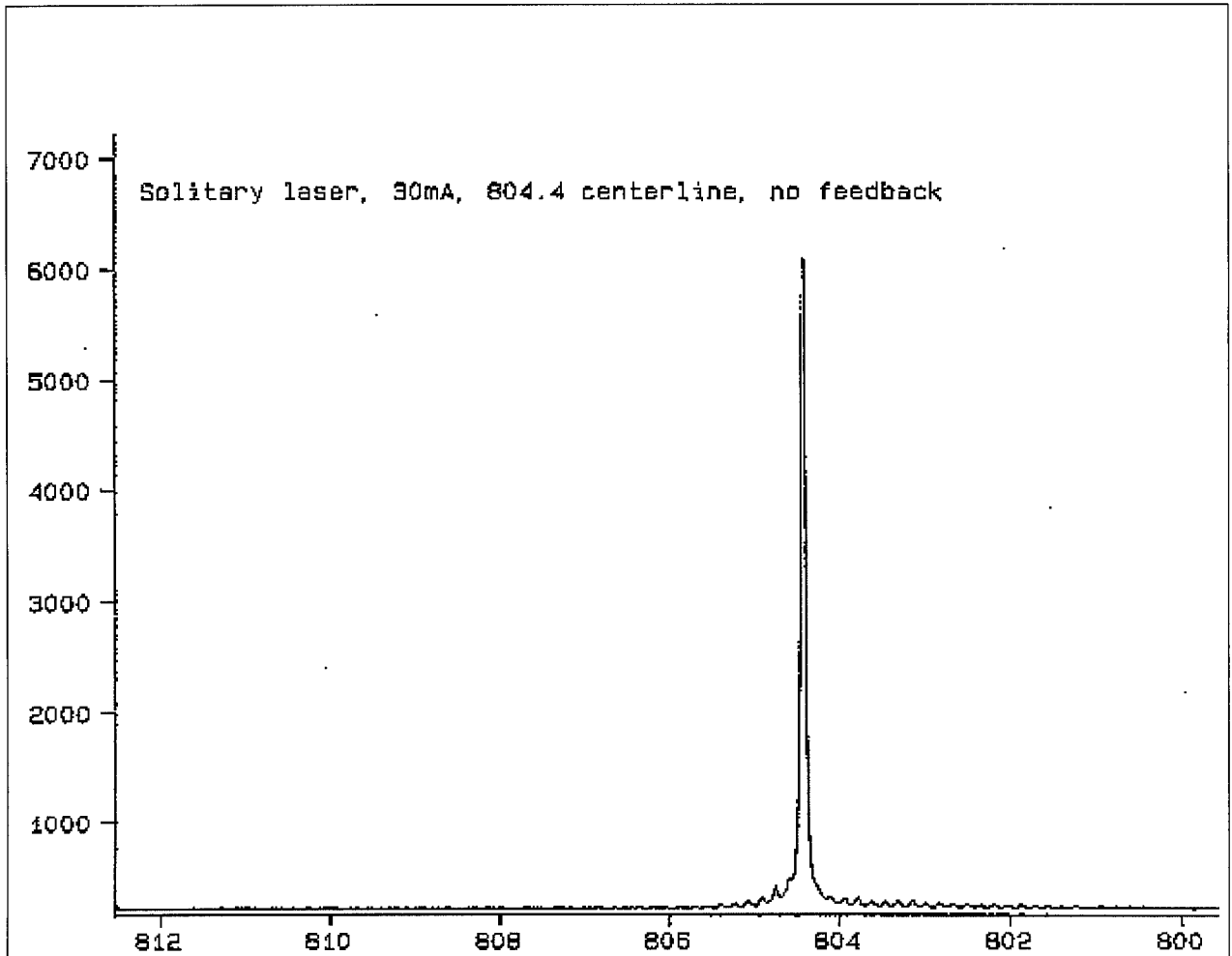
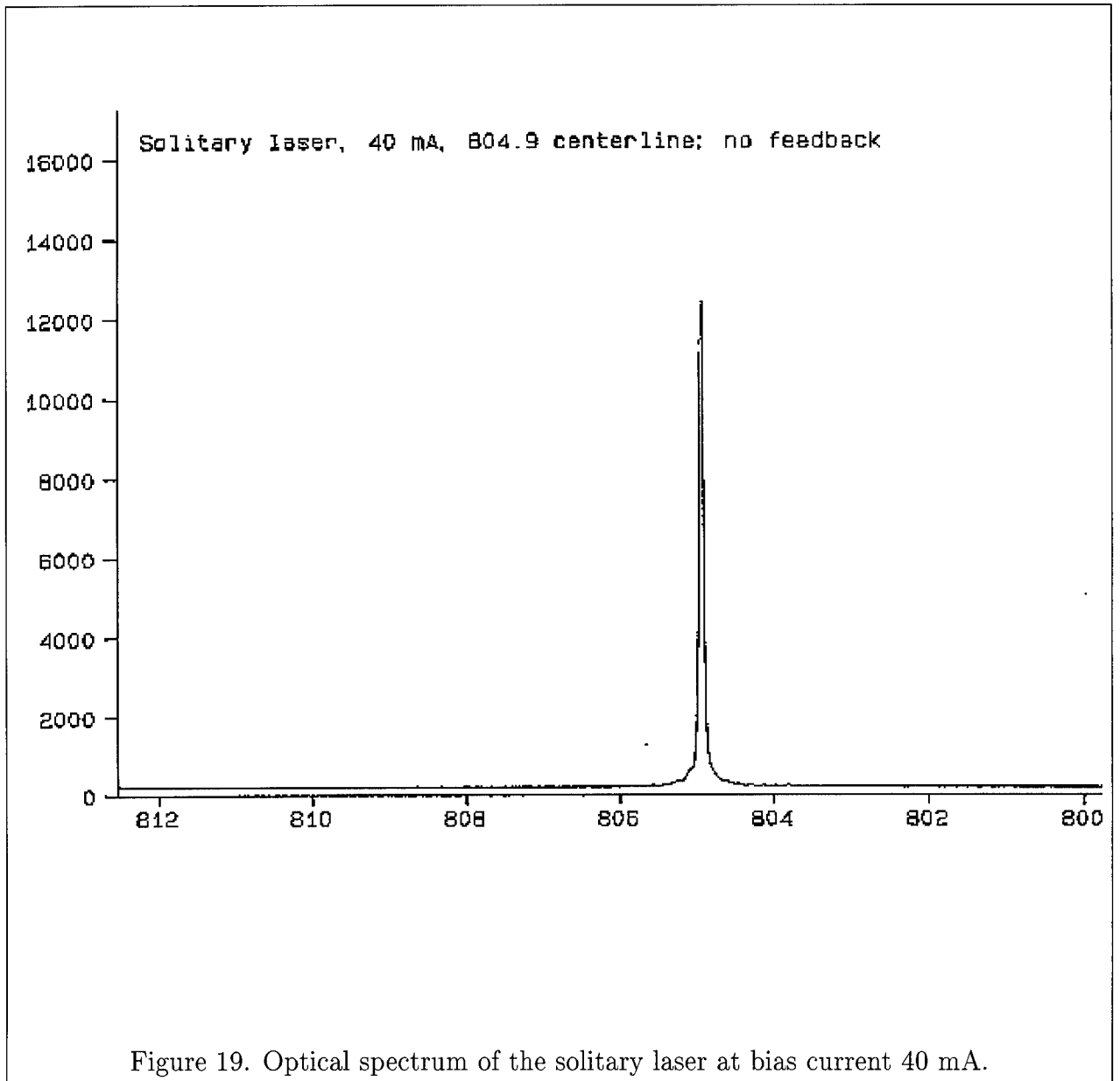
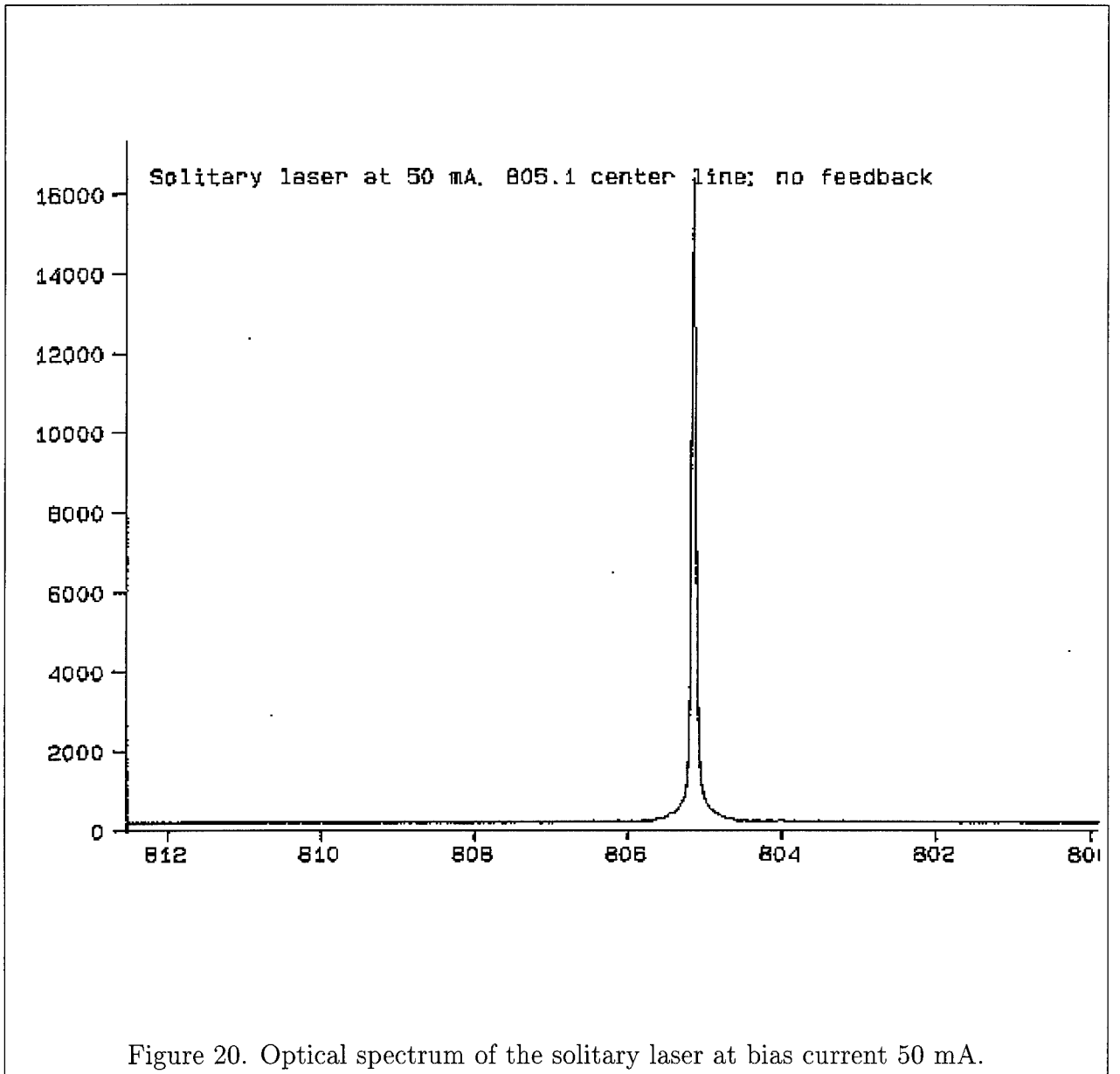


Figure 18. Optical spectrum of the solitary laser at bias current 30 mA. The center wavelength is 804.4 nm with small peaks surrounding the main lobe. These small peaks are easily excited with feedback causing the laser to operate multi-mode. Operating the laser with a bias current  $> 40$  mA ensures a single mode output.





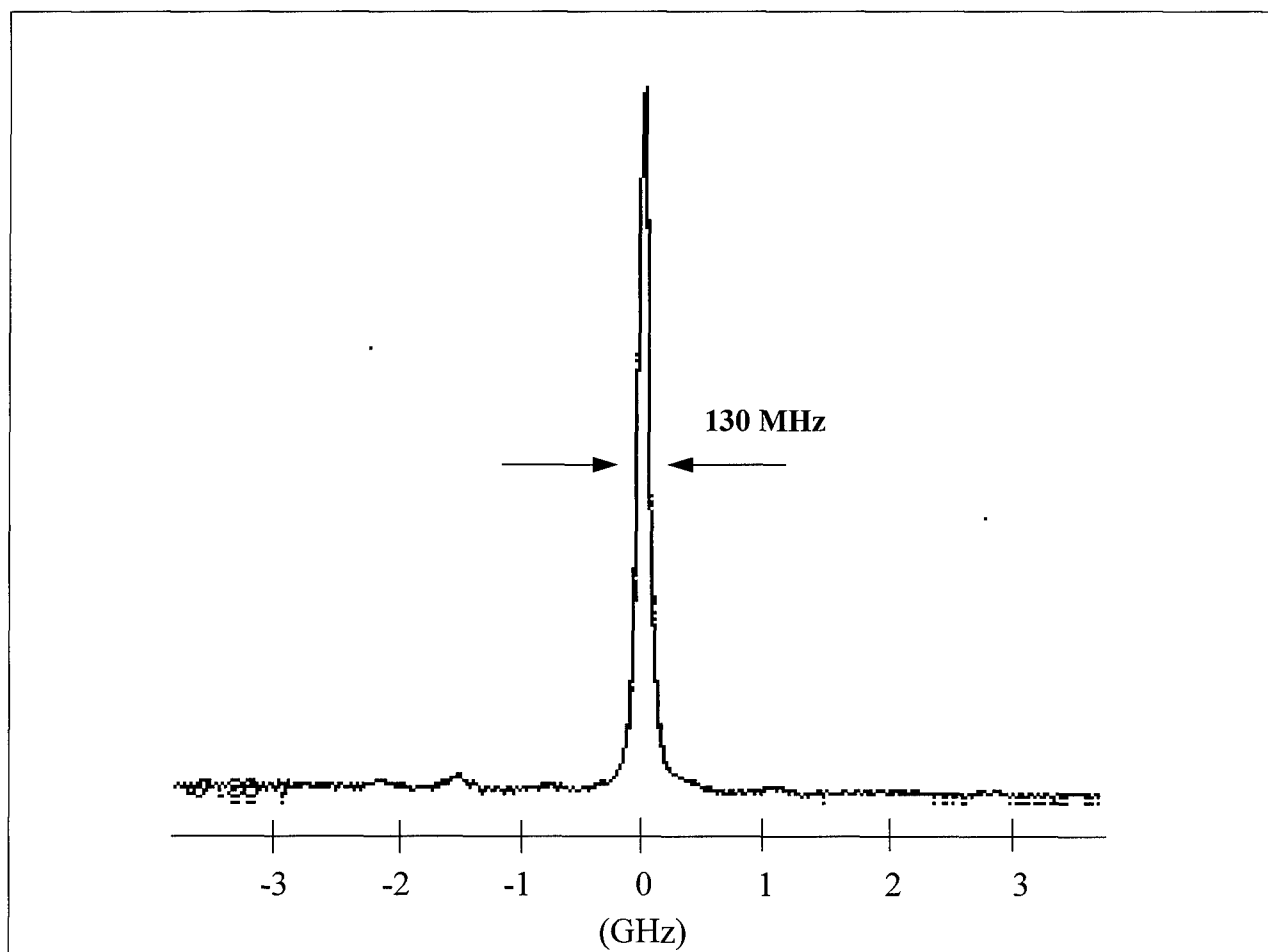
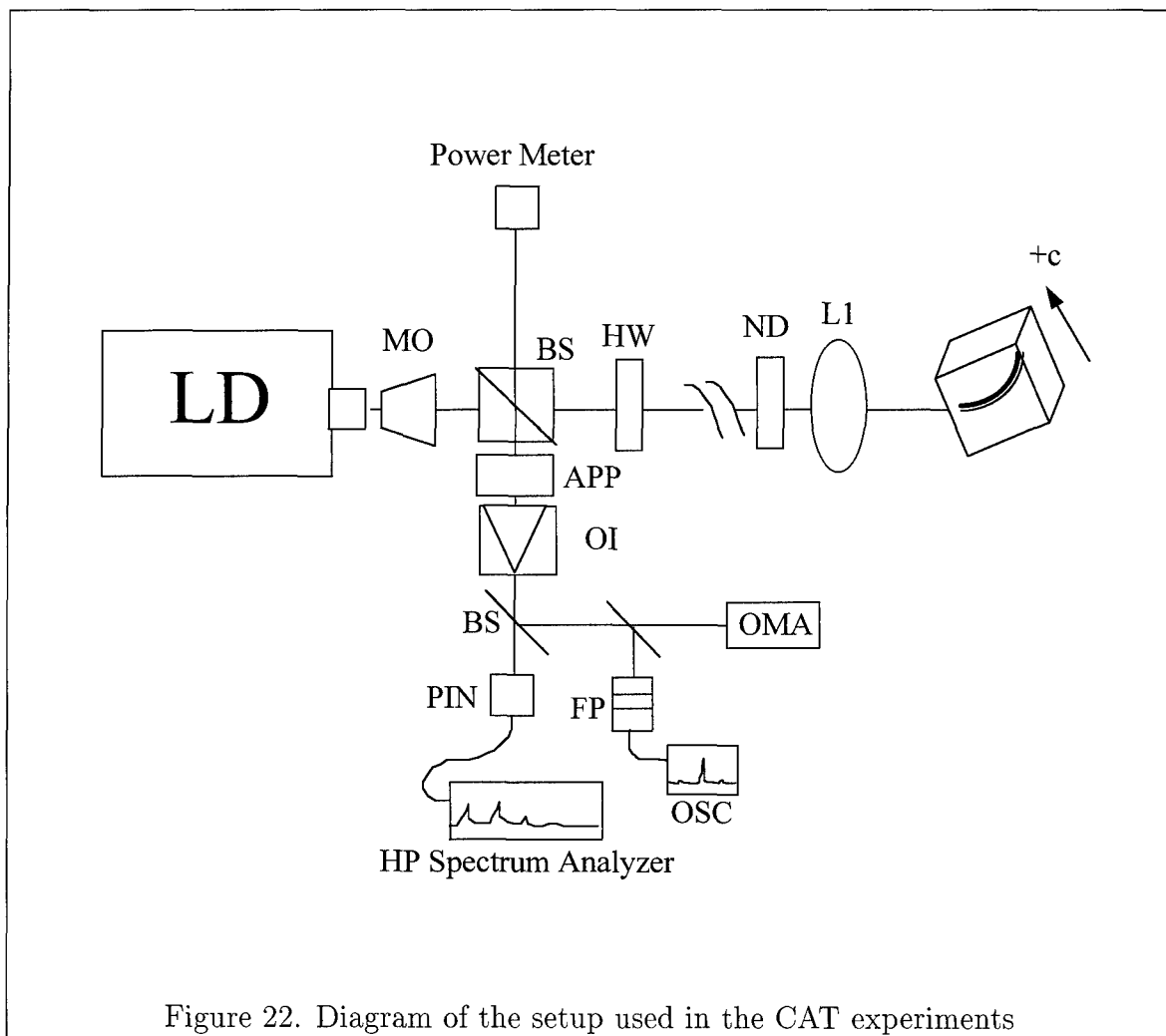


Figure 21. Fabry-Perot output of the solitary laser biased at 30 mA. The linewidth of the laser line is measured to be 130 MHz. The center lobe of the scan is rough due to low frequency noise in the power supply and temperature instabilities in the T-E cooler. The smaller peaks at -1.5 GHz and -2.2 GHz are other frequencies that exist at low bias currents.



light from the beamsplitter was passed through an anamorphic prism pair (APP) to re-shape the beam into a circular form which was well suited for the apertures in the diagnostic equipment. An optical isolator (OI), -41 dB, was used to prevent any back reflections from the diagnostic equipment from re-entering the laser diode thus establishing an unwanted external cavity. To examine the laser output for RF frequencies, an Electro-Optics Technology (EOT) amplified p-n junction diode (PIN diode), frequency response  $> 800$  MHz, was used with a Hewlett-Packard (H-P) RF Spectrum analyzer which had a frequency cut-off of 1.8 GHz. Two Fabry-Perots (F-P) were available to examine frequencies beyond the 1.8 GHz cut-off of the RF spectrum analyzer. One F-P had an 8 GHz FSR and Finesse  $> 200$ , the second with a 6 GHz FSR and Finesse  $> 10000$ . The former proved to be more useful in examining the optical spectrum of the laser diode since multiple F-P modes could not be completely eliminated in the latter. The final piece of diagnostic equipment was the 0.6 meter monochromator/OMA which was used to verify that single mode operation was maintained during the experiments.

For the beam going to the crystal, a half-wave plate (HW) was used to rotate the nearly linearly polarized laser output to coexist with the extraordinary direction in the crystal which is the favored orientation for generating a phase conjugate signal. In later experiments, the half-wave plate was eliminated to reduce the number of optical elements in the external cavity so that shorter external cavity lengths could be obtained. This did not have an adverse effect on the conjugate mirror since the diode output is greater than 95% linearly polarized and the laser is orientated so its primary polarization is in the extraordinary direction for the  $\text{BaTiO}_3$  crystal. A series of neutral density filters and a variable neutral density filter were used to control the amount of feedback and a 50 mm focal length lens (L1) was used to focus the beam loosely into the crystal. The phase conjugate return beam was sampled with a Newport 815 power meter to measure the average power returned to the laser from the external cavity mirror and a second EOT photodiode could also be used in

place of the Newport meter so that the RF spectrum of the return signal could be analyzed.

*5.2.1 Single Mode Operation with Phase Conjugate Feedback.* The primary purpose for this experiment was to verify that the laser remained in single-mode operation during the onset of chaos. If the laser did not remain single-mode then the assumption of a single-mode laser would have to be corrected and the coupled set of nonlinear Eqs. (49)-(51) would have to be modified to include multi-modes. As was mentioned in an earlier section, the OMA and F-P scans showed possible multi-mode operation of the solitary laser at laser current bias levels of 30 mA. Although the multiple modes in the solitary laser spectrum at that bias level did not contribute significant power to the laser output, applying feedback had a dramatic affect on these small amplitude modes causing them to significantly increase in amplitude. As mentioned earlier, the feedback experiments must be conducted with the laser operating in a single mode so an appropriate bias level to maintain single mode operation was required.

The OMA was used to monitor the laser output as the feedback was increased from zero  $\mu\text{W}$  until the laser began to show signs of the relaxation oscillation and external cavity frequencies undamping. Figure 23 shows outputs of the OMA with the laser biased at 30 and 40 mA with weak phase conjugate feedback. For 30 mA, a second mode appears at 804.6 nm for extremely weak feedback,  $< 0.002\%$  of the laser output, even before the relaxation oscillation frequency was detected. Additional peaks, as shown in the figure, appear at 804.7 and 804.9 nm for weak to moderate feedback. The inset in the figure is the RF spectrum taken at the same time as the OMA scan which shows  $\nu_{ext} = 225$  MHz and higher harmonics have become undamped. When the laser is biased at 40 mA, the laser remains single mode during the onset to chaos. Figure 23b shows the OMA scan when the laser is biased at 40 mA with moderate feedback ( $> 0.01\%$ ). The inset shows the strong RF peaks corresponding to  $\nu_{ext}$  and higher harmonics. Additional increases

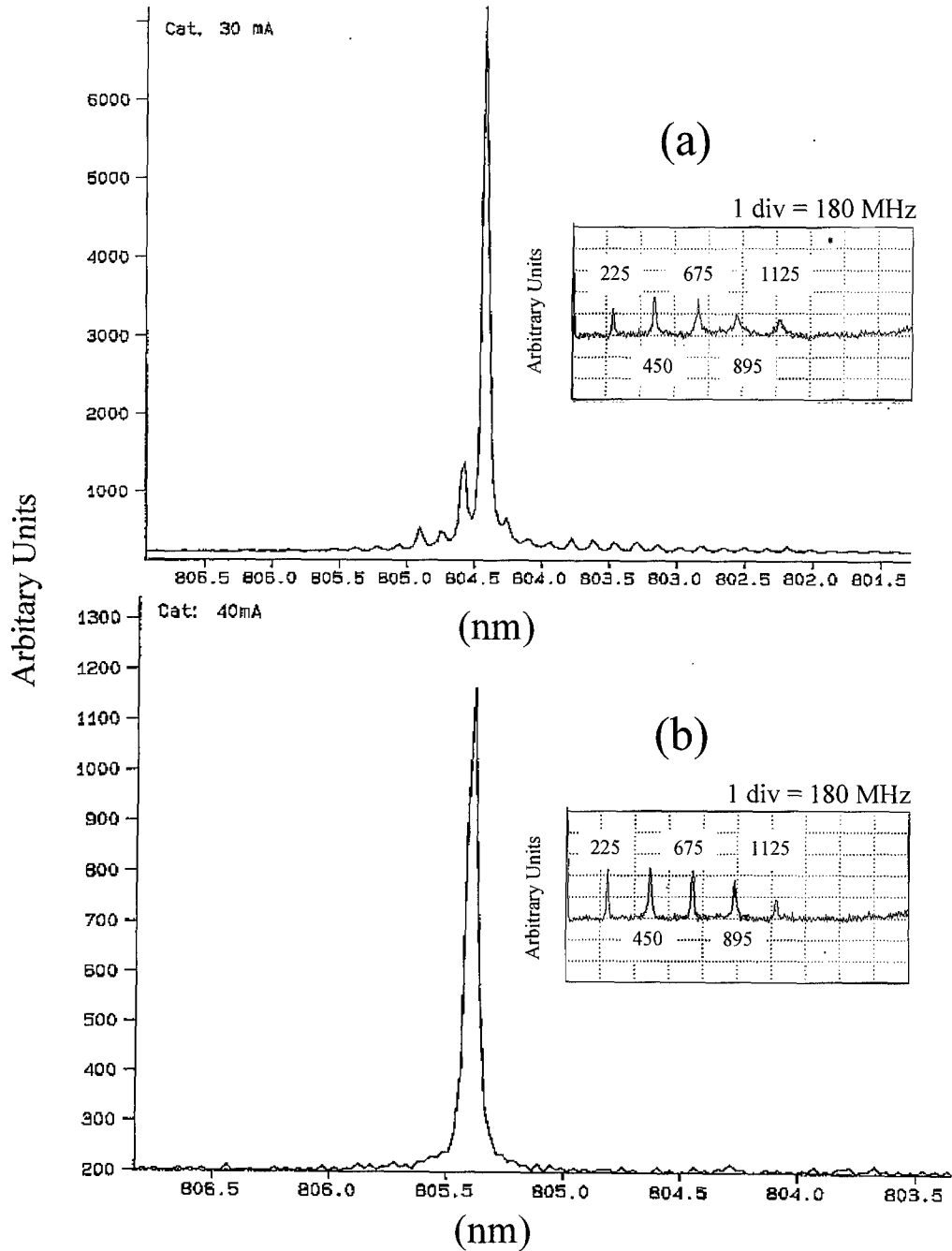


Figure 23. OMA scans during the onset of chaos. (a) The laser is biased at 30 mA and the feedback was set so that the relaxation and external cavity frequencies were undamped. Multiple laser modes have started to lase due to the feedback. (b) The laser is biased at 40 mA and the feedback is increased to place the laser near the chaotic state. Even at this strong feedback, the laser remains single mode.

in the feedback from that shown in the figure resulted in a broadband RF structure (chaotic behavior). Therefore, at the time of the scans shown in the figure, the laser was operating just below the chaotic region which covers the full range of feedback levels investigated in this research. Hence, laser bias currents above 40 mA were suitable for the additional feedback experiments and ensured single mode operation during weak to moderate feedback levels.

*5.2.2 CAT Phase Conjugate Mirror Time Response.* Part of the characterization of the onset of chaos for the CAT mirror configuration was to measure the speed of the crystal as a phase conjugate mirror. This would determine if a fourth coupled differential equation depicting the time response of the reflectivity of the PCM was necessary to describe the nonlinear behavior of the laser diode completely. The time dependent behavior of the mirror reflectivity would manifest itself in a  $d\kappa/dt$  equation. The theory leading up to the set of coupled nonlinear equations, Eqs. (49)-(51), has assumed that the PCM performs almost instantaneously, so  $\kappa$  is considered a constant.

The context of speed of the PCM is different than the onset, or build-up time of the mirror. The onset is the time needed by the crystal to create a conjugate signal once the crystal is illuminated. In BaTiO<sub>3</sub> and other photorefractives, the holographic grating constituting the PCM is established by photoionization of impurities creating charge carriers. These charge carriers then migrate in the crystal material and are trapped in the dark regions of the light intensity pattern. This sets up a space-charge electric field which in turn modulates the refractive index of the crystal through the Pockels effect. Since the whole process of establishing the holographic index grating relies on the migration of charge carriers in the crystal, the fundamental time limit for the onset of the grating is on the order of 2 ms for BaTiO<sub>3</sub> (31:102). However, once the holographic grating has been established, the speed at which the mirror reacts to small changes in the input beam is the real question at hand. The development of chaotic behavior in the laser diode introduces numer-

ous high frequencies in its output resulting from the undamping of the relaxation oscillations (several GHz) and external cavity frequencies (several MHz).

These questions were answered in a series of experiments that compared the frequency content and delay of the feedback signal from the CAT phase conjugate mirror configuration to a feedback signal from a normal dielectric mirror. Figure 22 shows the experimental setup for the CAT phase conjugate mirror. Fast PIN diodes were used to sample the direct laser output and the feedback signals. The output signal from the PIN diodes was displayed on a RF signal analyzer and a 500 MHz oscilloscope. In both cases the feedback was adjusted so that the relaxation oscillation and the external cavity frequencies became slightly undamped so that the laser would not enter the chaotic regime. Furthermore, the intensities of the beams entering the PIN diodes were balanced with a variable neutral density (ND) filter placed in front of the diode sampling the direct laser output so the signal amplitudes could be quantitatively compared. To compare the signal wave-forms, significantly long external cavities ( $> 30$  cm) were chosen so that the fundamental cavity frequency would be well below the bandwidth limit of the 500 MHz oscilloscope.

Figure 24 shows two traces from the RF signal analyzer for the feedback from a normal mirror and the laser output. The decrease in magnitude of the peaks above 800 MHz is due to the decrease in sensitivity of the PIN diodes used in the experiment. It can be clearly seen in this figure that the frequency content of both the normal feedback and laser output signals are the same. The external cavity mode of 230 MHz ( $L_{ext} = 65$  cm) and higher harmonics are easily identified in both signals, indicating that amplitude modulation from the onset of chaotic activity in the laser is contained in both the laser output and the normal feedback signal. For a normal dielectric mirror, this response is expected since these mirrors can be considered to react instantaneously and have a flat broadband RF response.

The time delay between the two PIN diode detectors is shown in Figure 25 as a correlation between the two signals. The correlation trace shows that the feedback

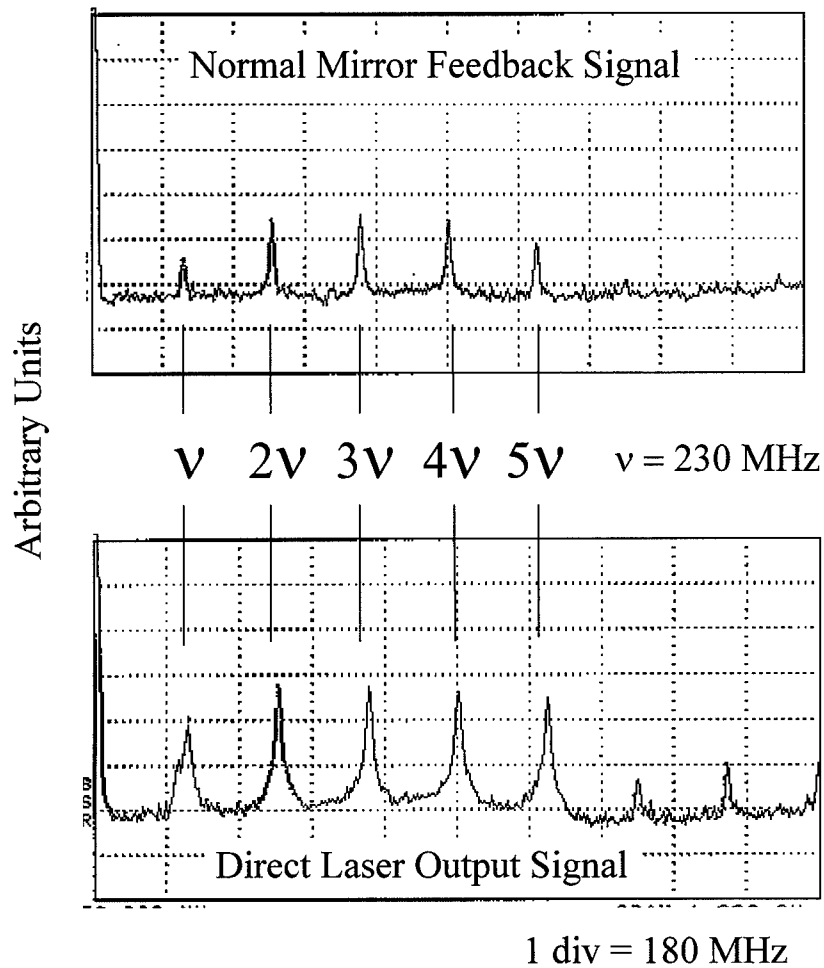


Figure 24. RF spectra of the feedback signal from a normal mirror (above) and the laser output (below). Both signals contain the same frequency information indicating that there is no filtering being done by the normal mirror. The speed of a normal mirror can be considered instantaneous.

signal (middle trace) is highly correlated with the original laser output (top trace) at a point when the feedback waveform is delayed by 11 ns. The calculated path difference (both optical and electrical) between the two traces is 10.9 ns indicating that all delays have been properly accounted.

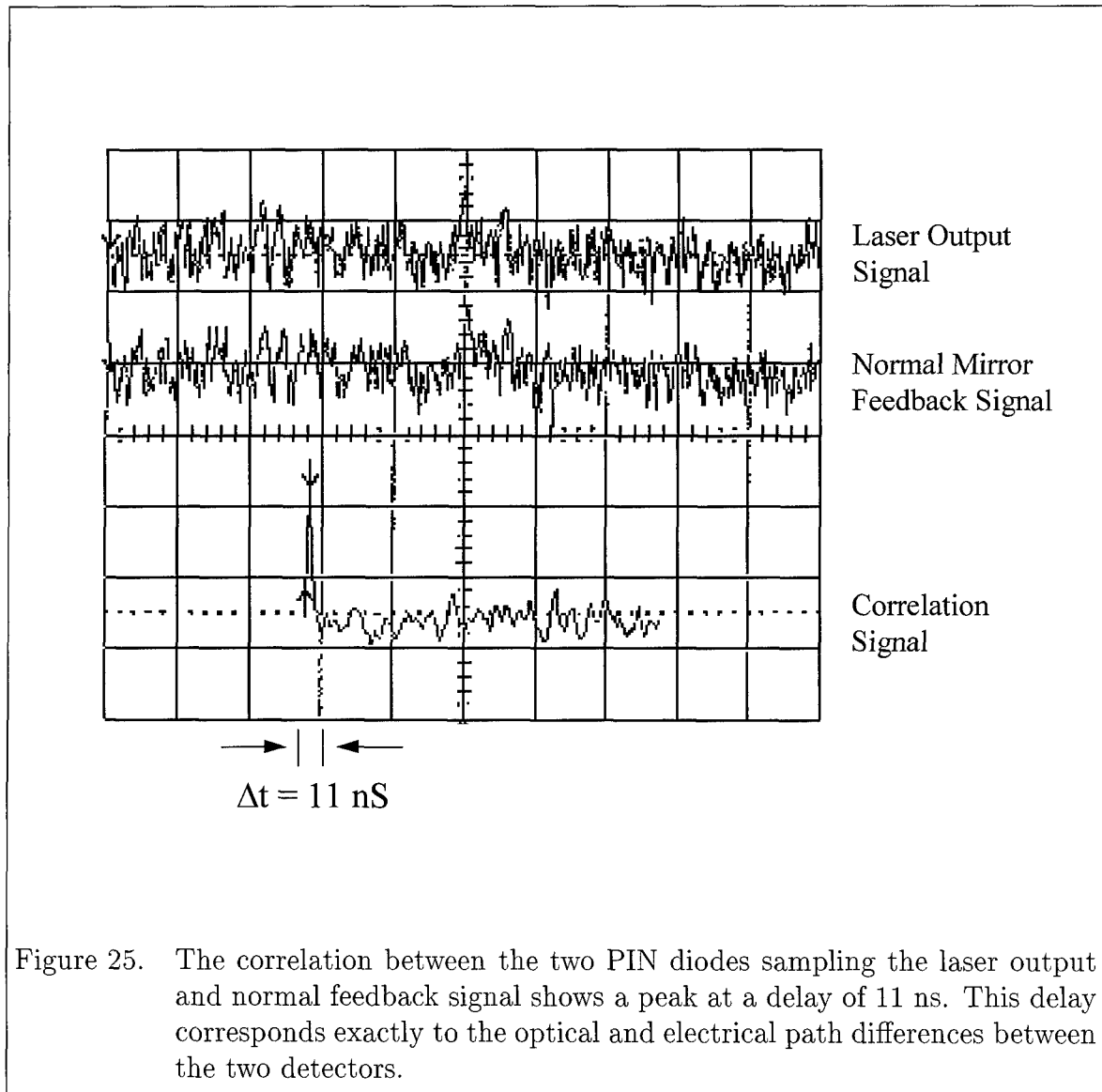


Figure 26 shows a similar RF spectrum for the case of the CAT PCM for an external cavity of 87 cm. The small overall magnitude of the two traces is a result of the lower intensity necessary by the CAT PCM to undamp the external cavity

frequency. Since the phase conjugate feedback couples easier into the laser cavity than the normal mirror, significantly lower feedback levels were used to prevent the laser from going fully chaotic. Therefore the ND filter in front of the laser output detector was increased to balance the two signals for comparison purposes. Regardless of the absolute magnitude of the two signals, it is easily seen that the PCM feedback signal also contains the fundamental external cavity frequency plus several harmonics. Figure 27 shows the correlation (bottom trace) between the direct laser output (top trace) and the CAT phase conjugate signal (middle trace). As was shown for the normal dielectric mirror, the two signals have a strong correlation peak corresponding to the path differences between the two PIN detectors. In other words, the CAT PCM feedback signal contains the RF frequency information and correlates well with the direct laser output and therefore, performs on the order of the normal dielectric mirror.

*5.2.3 External Cavity Length and Frequency Dependency.* One of the easiest parameters to change in the set of nonlinear equations is the time delay due to the position of the feedback mirror in the external cavity. According to the analysis of Auyeung *et al*, the mode structure of the external cavity bounded by a PCM depends on whether the PCM is established by degenerate or non-degenerate four-wave nonlinear interaction (4). For the degenerate case, such as the self-pumped CAT and DPCM configurations used in this research, the external cavity will support a frequency spacing of  $c/(2L_{ext})$ . This is obtained by requiring a single-round trip self-consistent solution for the complex radius of curvature of the wavefront. This spacing is also the same for a cavity bounded by a normal mirror. In contrast, for a non-generate PCM the field must take two round trips in the external cavity in order to satisfy the self-consistent solution, thus the mode spacing for the non-degenerate PCM becomes  $c/(4L_{ext})$ . This change from the non-degenerate case results from a frequency shift in the conjugate beam and passing through the PCM a second time cancels this effect. The non-degenerate PCM was not investigated in this research.

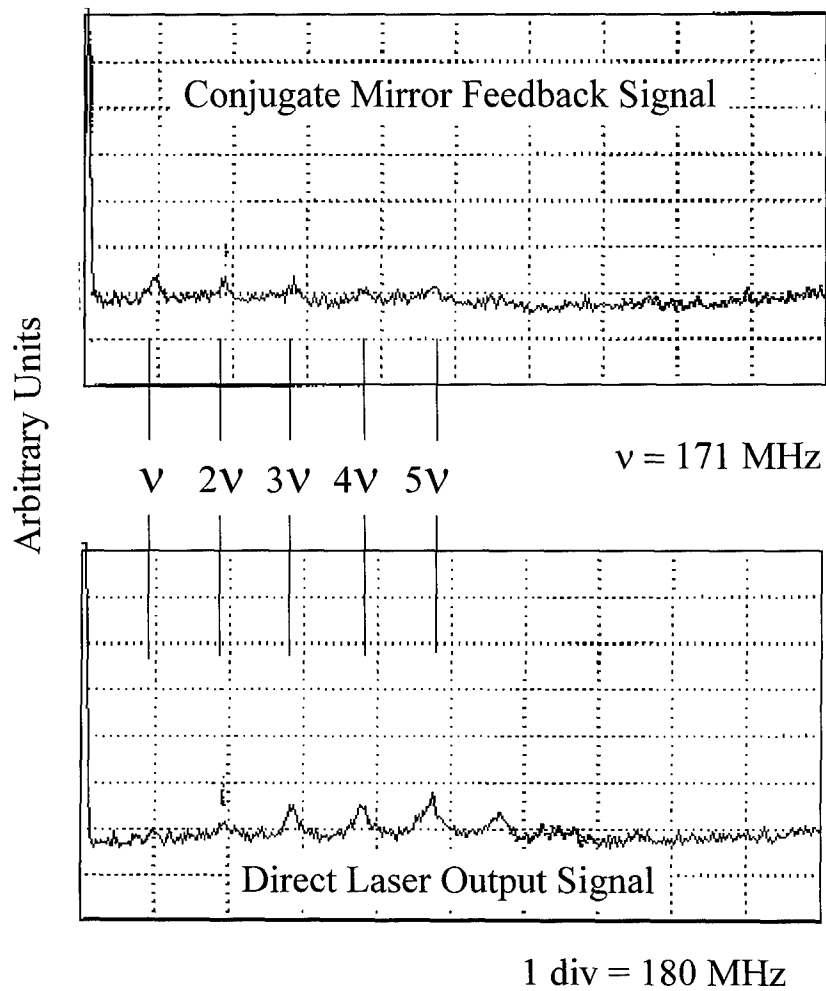
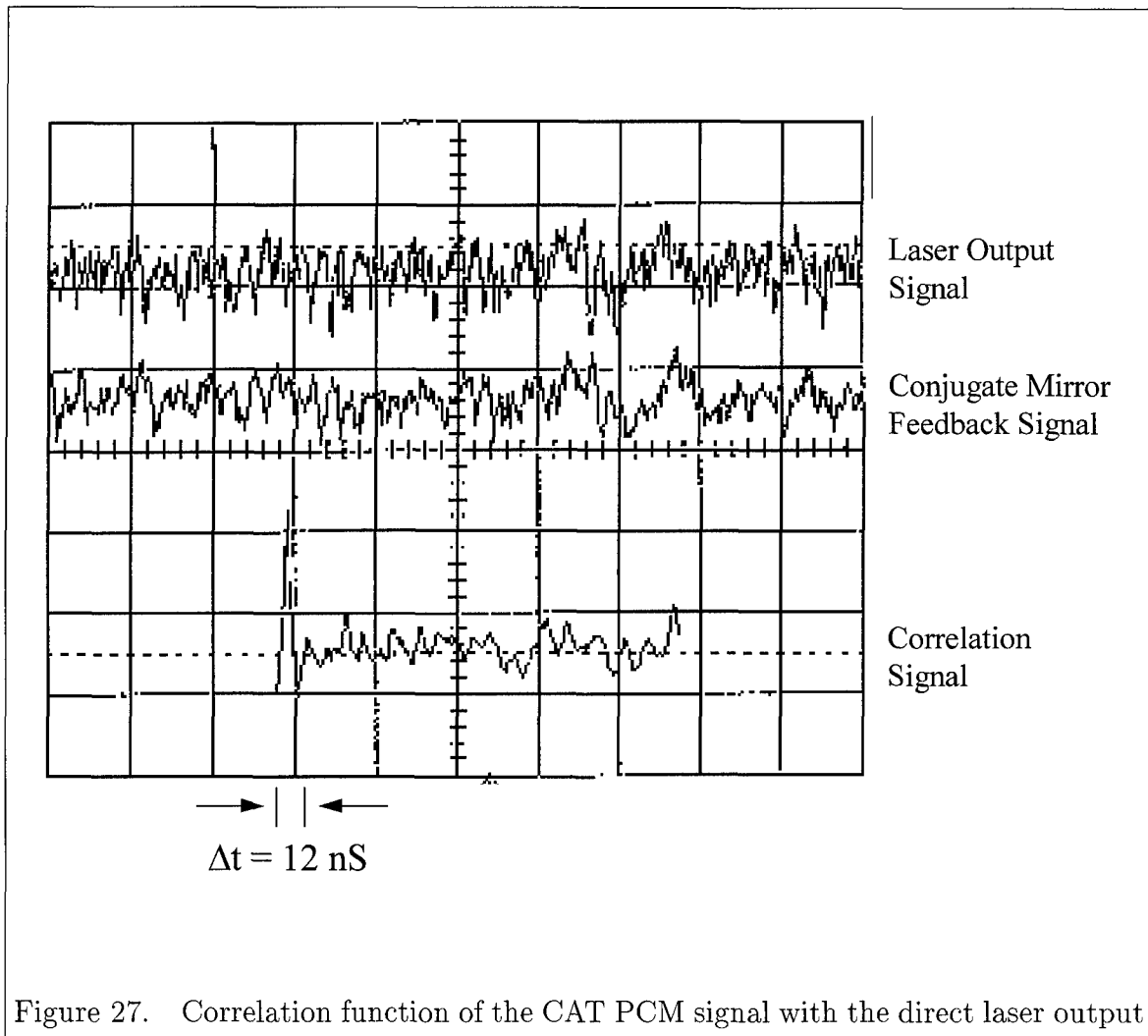
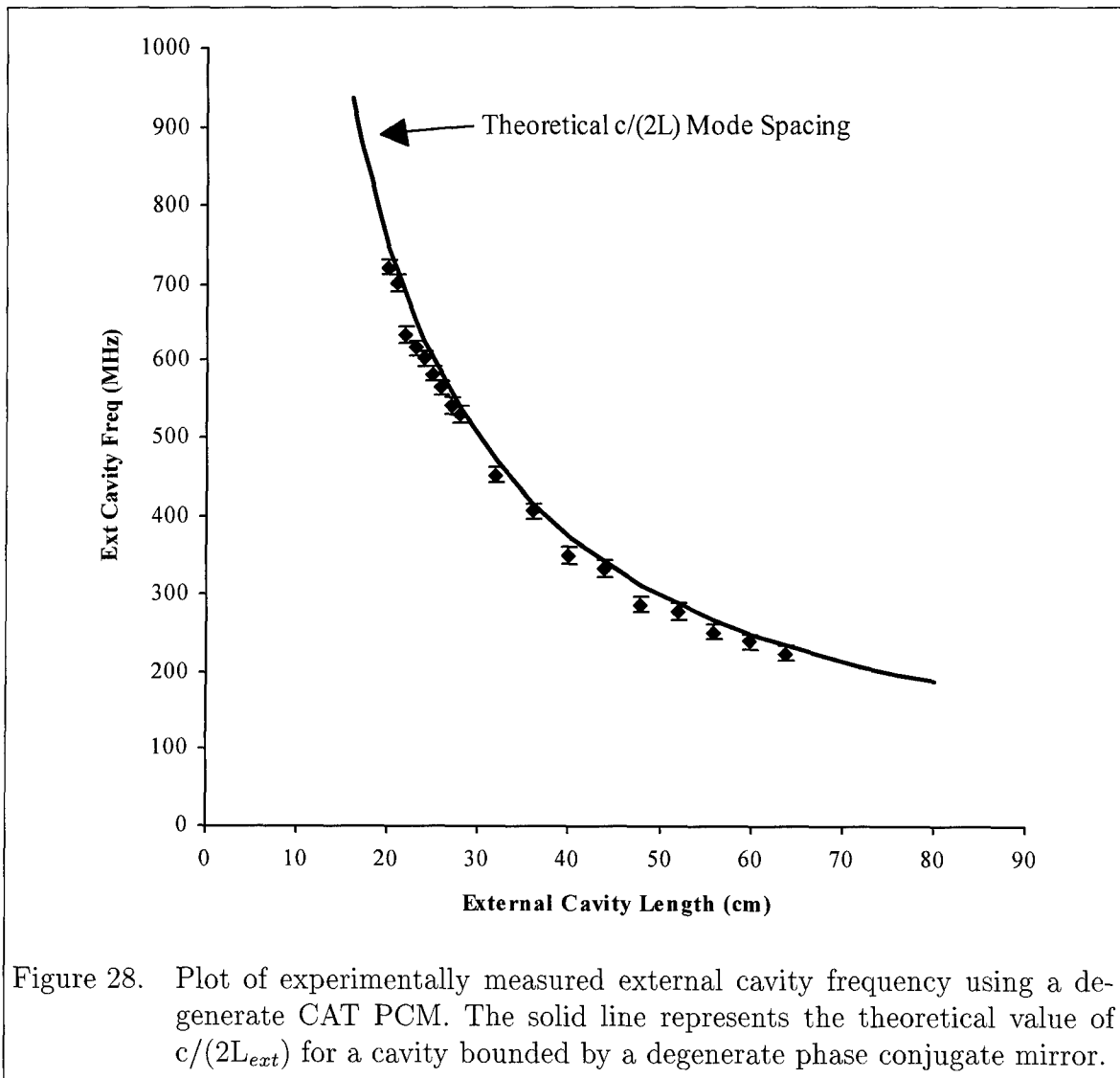


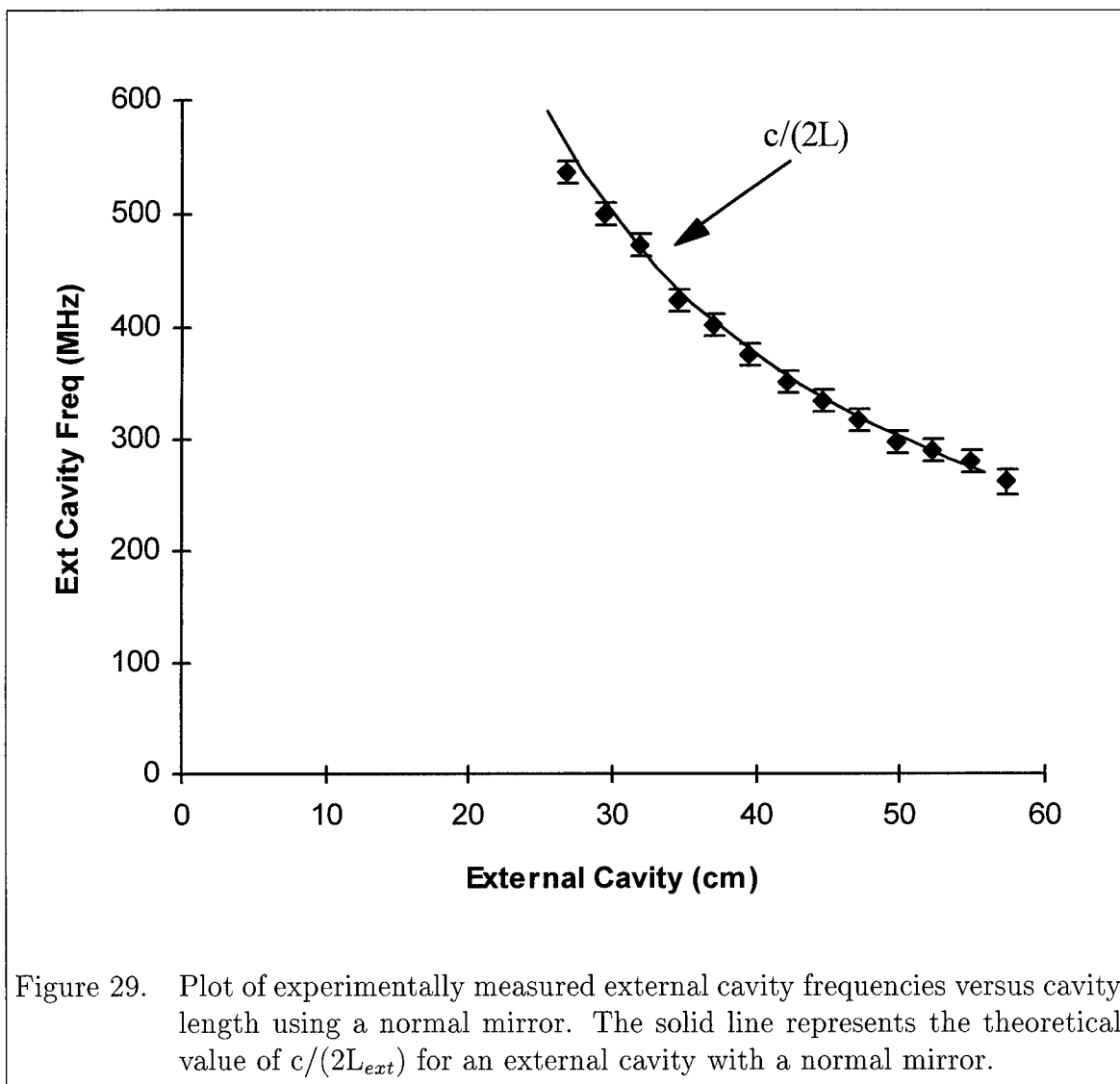
Figure 26. RF spectra of the feedback signal from the CAT PCM mirror and the laser output. Both signals contain the same frequency information indicating that there is no filtering being done by the CAT mirror.



The graphs in Figures 28 and 29 show the effect of the external cavity frequency,  $\nu_{ext}$ , by varying the external cavity length using the CAT phase conjugate mirror and a normal mirror. Each graph shows the theoretical limit of  $\nu_{ext} = c/(2L_{ext})$  for the degenerate PCM and normal mirror, where  $L_{ext}$  is the optical path measured from the edge of the laser facet to the entrance face of the crystal.

*5.2.4 External Cavity Resonance and Frequency Locking.* Based on the mathematical analysis presented in Section 3.3, resonance enhancement in the feedback levels for the first Hopf bifurcation was expected as the external cavity length was extended. The external cavity was scanned using a micrometer translation





stage and a Klinger translation stage. The micrometer stage was restricted by a 2 cm throw which caused a slight error in the measurement by resetting the stage for subsequent scans. This problem was corrected by replacing the micrometer with a Klinger translation stage which had a significantly larger throw. Figure 30 shows the experimental equipment used to investigate the cavity resonance using the CAT geometry. The cavity was extended over 8 cm, in 1 mm increments, to capture at least two resonance cycles predicted by Eq. (66). The Hopf point was determined by monitoring the F-P display and recording the feedback power when the relaxation frequency appeared. The phase conjugate feedback was then allowed to grow until the external cavity frequency could be recorded.

Figure 31 shows the results of the data collection. The top curve, which corresponds to the right vertical axis, plots the ratio of the relaxation frequency to the external cavity frequency,  $\nu_R/\nu_{ext}$ . The stair stepping nature of the curve indicates frequency locking of  $\nu_R$ , with the plateaus corresponding to integer values 6, 7, and 8. The lower part of the curve shows the power of the feedback signal at the first Hopf bifurcation when  $\nu_R$  becomes undamped. Resonances can be seen for cavity lengths of 22.8 and 26.2 cm with the width of the locking region being 3.4 cm. The peak shown at 20.2 cm is the trailing edge of an earlier peak.

The mechanism allowing the integer steps in the ratio of the two frequencies is the change in  $\nu_R$ . The lower half of Figure 32 presents the variation in  $\nu_R$  and compares it to the locking ratio presented in the previous figure. The solitary laser relaxation oscillation frequency of 3.7 GHz falls midway between the maximum and minimum values. At the points of transition to a higher integer ratio,  $\nu_R$  will attain its maximum value and  $\Delta\nu_R = 500$  MHz over the full locking range.

*5.2.5 Verification of the Conjugate Signal.* As mentioned in Section 5.2.3, the mode spacing for the degenerate PCM and the normal cavity is the same  $c/(2L_{ext})$  relationship. Since the mode spacing is the same, verification of a phase conjugate

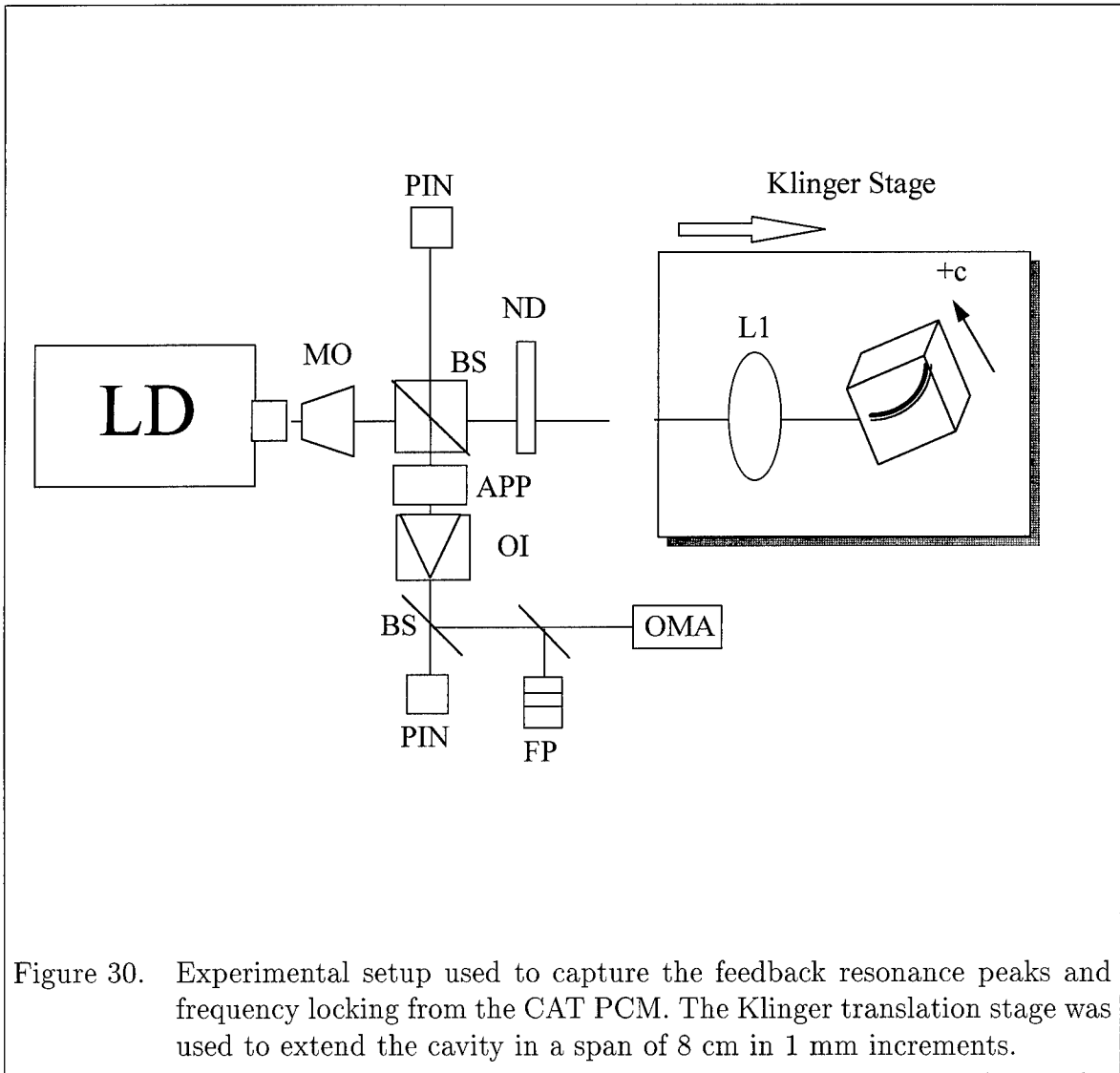


Figure 30. Experimental setup used to capture the feedback resonance peaks and frequency locking from the CAT PCM. The Klinger translation stage was used to extend the cavity in a span of 8 cm in 1 mm increments.

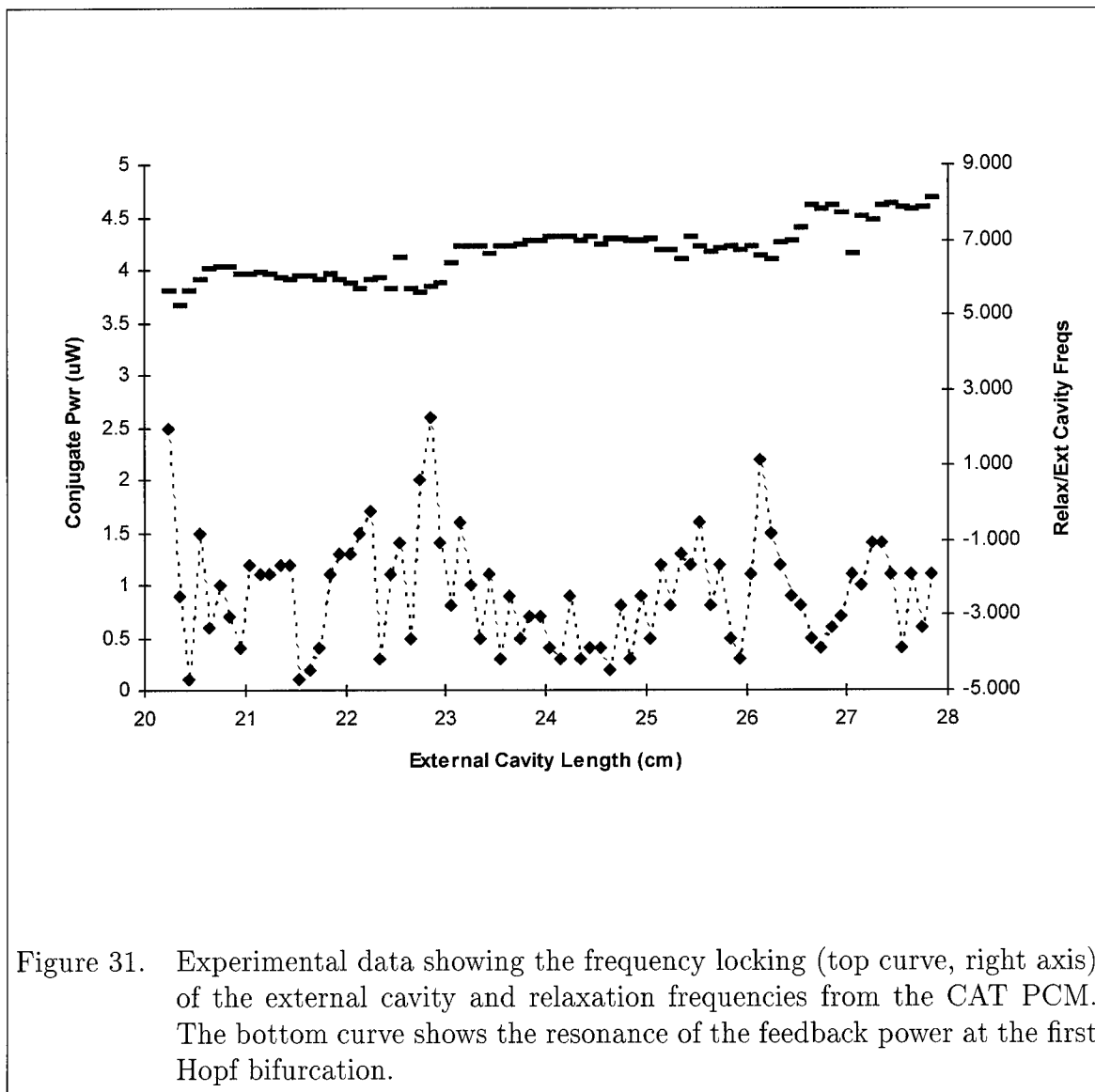
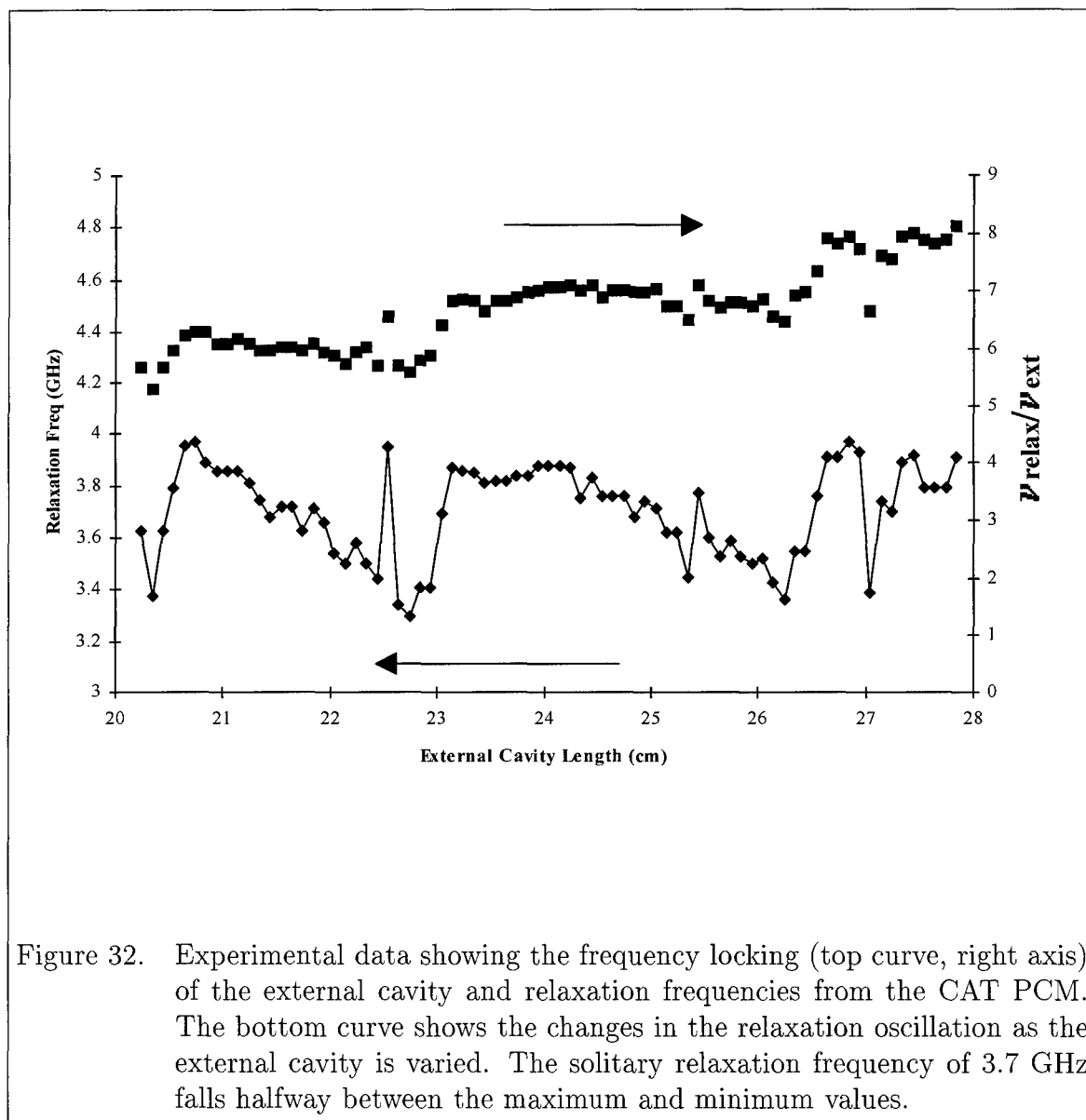
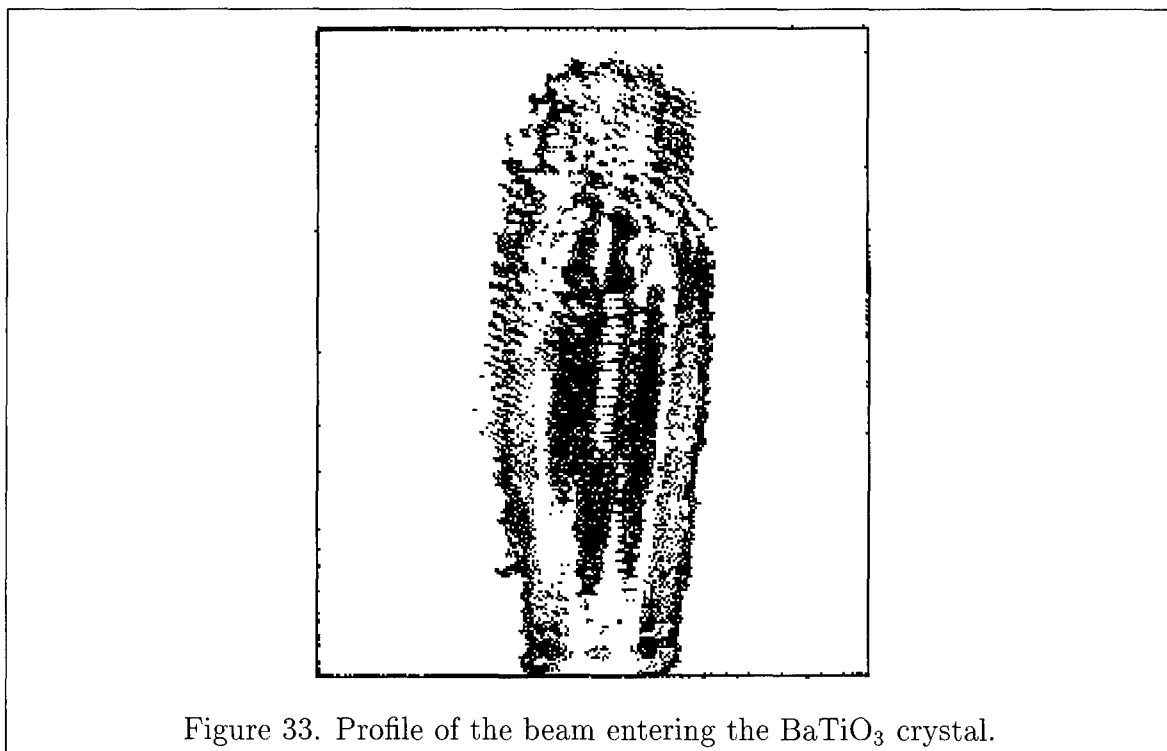


Figure 31. Experimental data showing the frequency locking (top curve, right axis) of the external cavity and relaxation frequencies from the CAT PCM. The bottom curve shows the resonance of the feedback power at the first Hopf bifurcation.



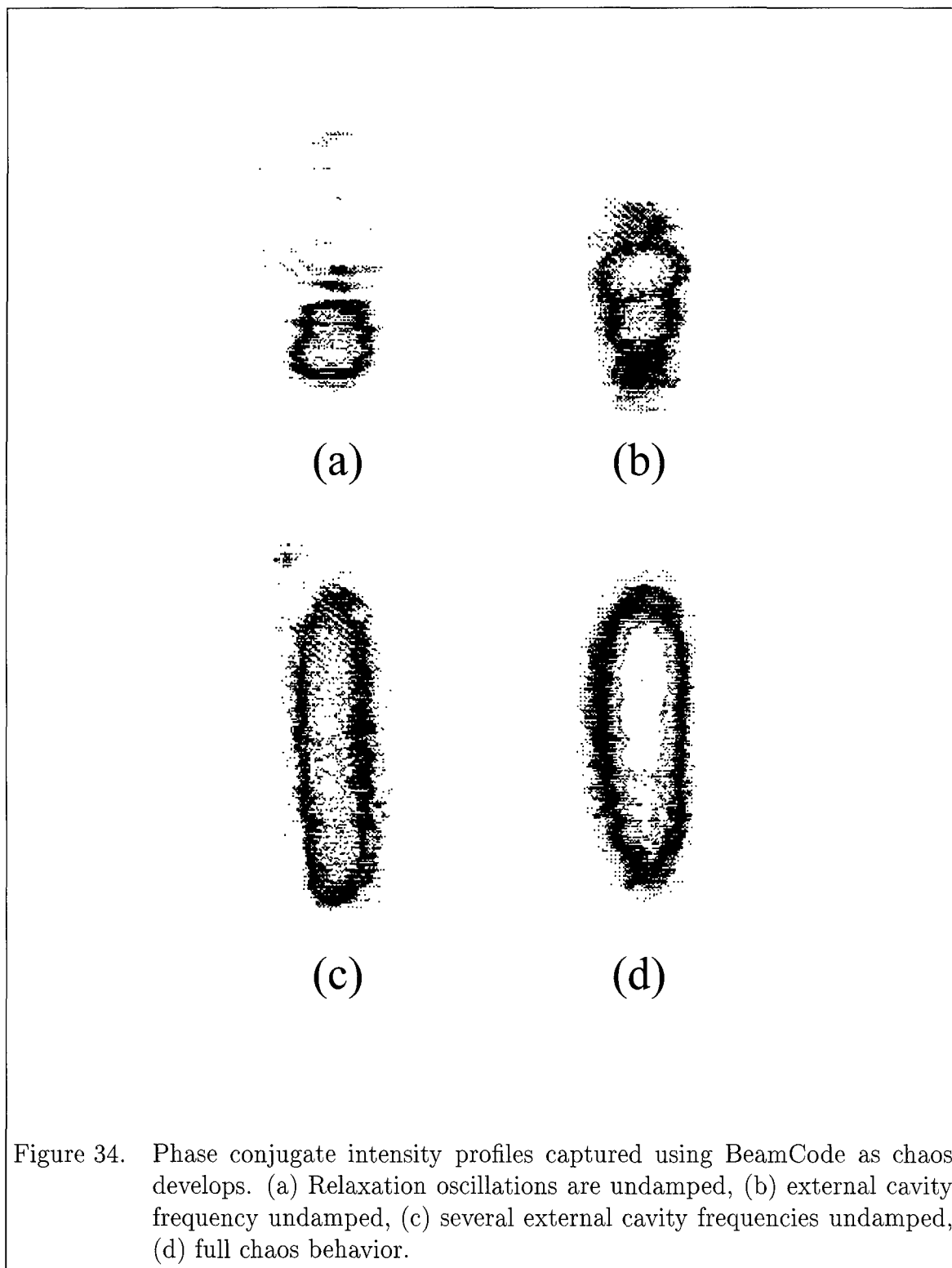
signal was necessary to rule out the possibility that the feedback beam for the CAT mirror might contain a normal reflection component, possibly from total internal reflection inside the crystal. Therefore, several experiments were conducted to test the validity of the phase conjugate signal using the commonly accepted method of image reconstruction through a phase distorting medium in the optical path (6).

To capture the image of the conjugate beam, a BeamCode camera replaced the Newport meter sampling the conjugate beam. The camera was also placed in the beam entering the crystal to record the profile of the original beam. Figure 33 shows the contour profile of the original beam entering the crystal. The vertical fringes



shown in the figure are a result of interference effects from several ND filters placed in front of the camera. The basic profile of the unaltered beam is a 2-D gaussian, with the horizontal direction having the smaller waist.

Figure 34 shows the conjugate return profile for several levels of feedback. In (a), the relaxation frequency has begun to undamp and the conjugate begins to



build around the central portion of the beam profile. The reconstruction of just the central portion of the original profile is a consequence of the low feedback power needed to undamp the relaxation oscillation. With the self-pumped geometry, low feedback power is generated by low input intensity to the BaTiO<sub>3</sub> crystal, hence only the most intense portions of the image profile (central portion) are efficiently conjugated. Increasing the feedback until the external cavity mode appears, the conjugate profile shown in (b) continues to grow around the central portion of the profile. Image (c) shows the beam profile as the feedback is increased to the level where several harmonics of the external cavity frequency appear. When full chaos in the laser output is reached, (d), the conjugate signal is well defined and resembles the original beam. This profile clearly shows the full reconstruction of the original image.

The same sequence of events was repeated with a normal cavity for comparison. Figure 35 shows the beam profiles corresponding to the events of the relaxation oscillations undamped (a), external cavity frequency undamped (b), and full chaos in the laser output (c). As expected, the full beam profile is clearly visible in all cases since the normal mirror has a flat intensity response to its input beam. The only difference between the images in the figure is the overall intensity of the return beam entering the camera, which increases from (a) to (c).

Using a piece of plastic as a phase distorting medium, the two tests were repeated. Figure 36 shows a comparison of the conjugate and normal feedback profiles. In both cases the images shown were taken when the relaxation and external cavity frequencies have undamped. It was also noted that the phase conjugate mirror with the distorter required about the same amount of feedback power to achieve the undamping of the two frequencies as compared to the PCM without the distorter. In contrast, the normal mirror required over 50% more feedback power to achieve the same result.

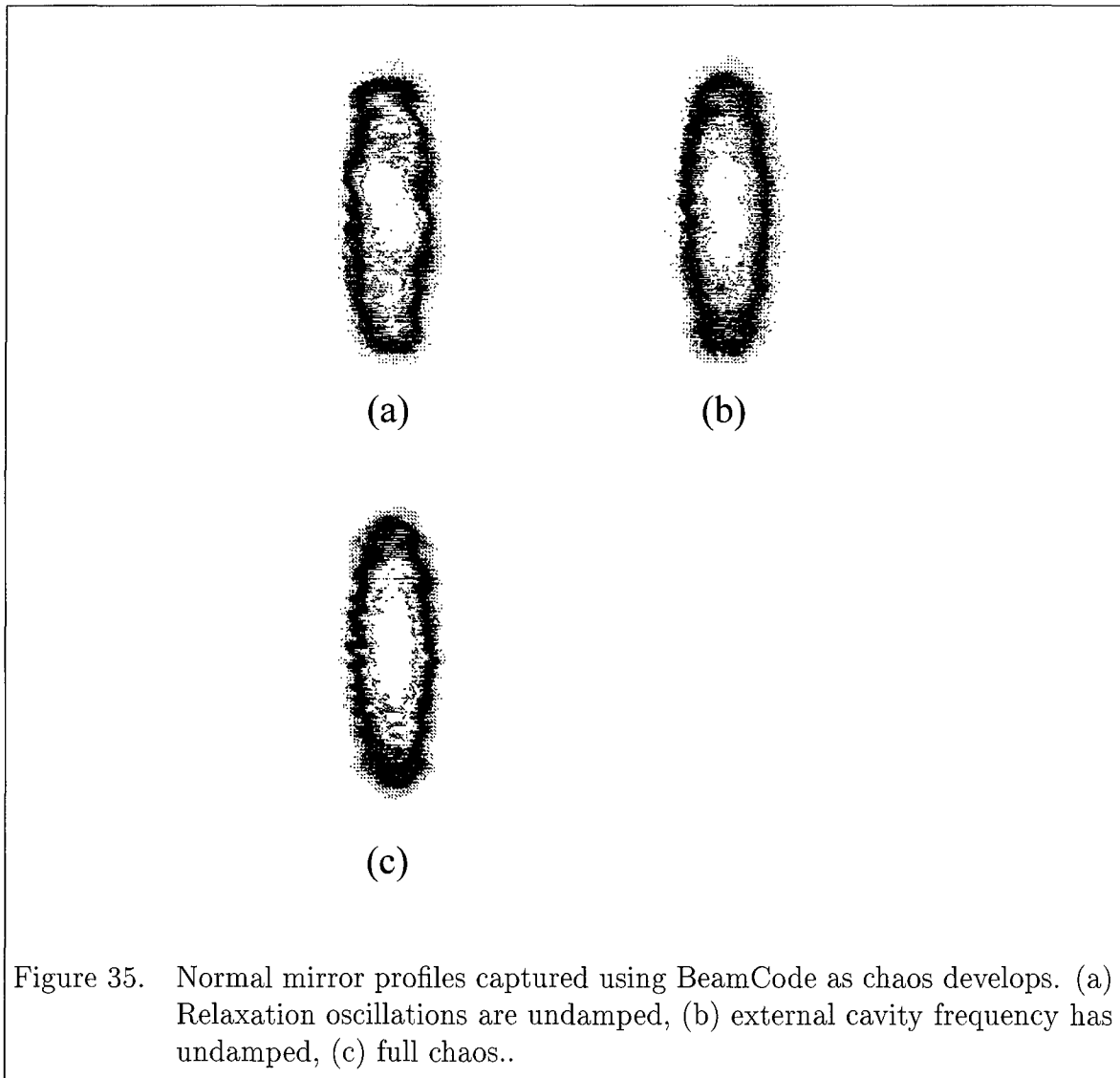
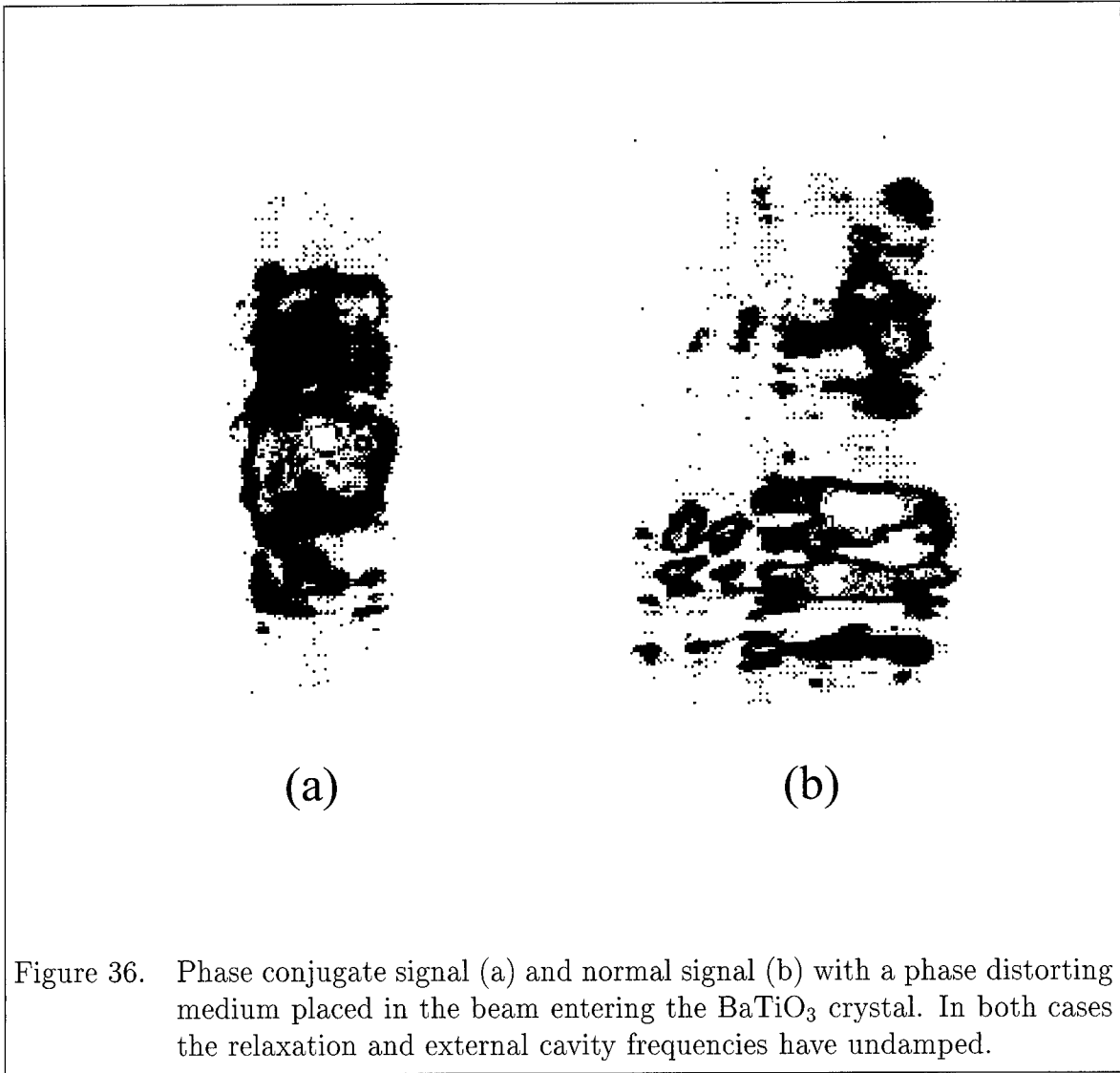


Figure 35. Normal mirror profiles captured using BeamCode as chaos develops. (a) Relaxation oscillations are undamped, (b) external cavity frequency has undamped, (c) full chaos..



The changes in feedback power for the normal mirror is easily attributed to scattering of photons off the distorting medium. Coupling into the laser is reduced since the phase front is badly distorted, therefore, more feedback power is required to overcome the losses in the external cavity. The behavior of the conjugate signal demonstrates that the PCM is producing a conjugate beam which feeds back the same amount of power even with the distorting medium in the beam path.

### *5.3 Double Phase Conjugate Mirror Measurements*

Most of the tests described in Section 5.2 for the CAT geometry were duplicated with the double phase conjugate mirror (DPCM). Figure 37 shows the basic experimental setup used to conduct the tests. The mirror was constructed using the transmission grating DPCM with input angles of  $120^\circ$  degrees, with respect to the +c-axis. A variety of input angles were tried, most arrangements produced little or no feedback. It appeared that  $120^\circ$  was the most optimal choice of angle. Even at this setting, the maximum amount of feedback was small compared to the CAT geometry. As a result, full chaotic behavior was never achieved with the DPCM, although sufficient feedback was obtained to operate in Levels I, II and III. Due to complexities of the DPCM geometry, the external cavity was not varied as extensively as the CAT geometry, but was varied enough to verify the trends shown in the CAT external cavity experiment.

The experimental results of the conjugate feedback of the DPCM configuration show similar behavior to the CAT PCM. Figure 38 shows the external cavity mode spacing as a function of the round trip external cavity length. Measurement of the cavity length is slightly different than the CAT PCM geometry since the DPCM is an asymmetric cavity. For the DPCM, photons from one beam are scattered off the holographic grating in the direction of the other input beam's conjugate signal, as was shown in Figure 7. Therefore, the external cavity is in a ring formation as the photons traverse through the  $\text{BaTiO}_3$  crystal, retracing the opposite input beam's

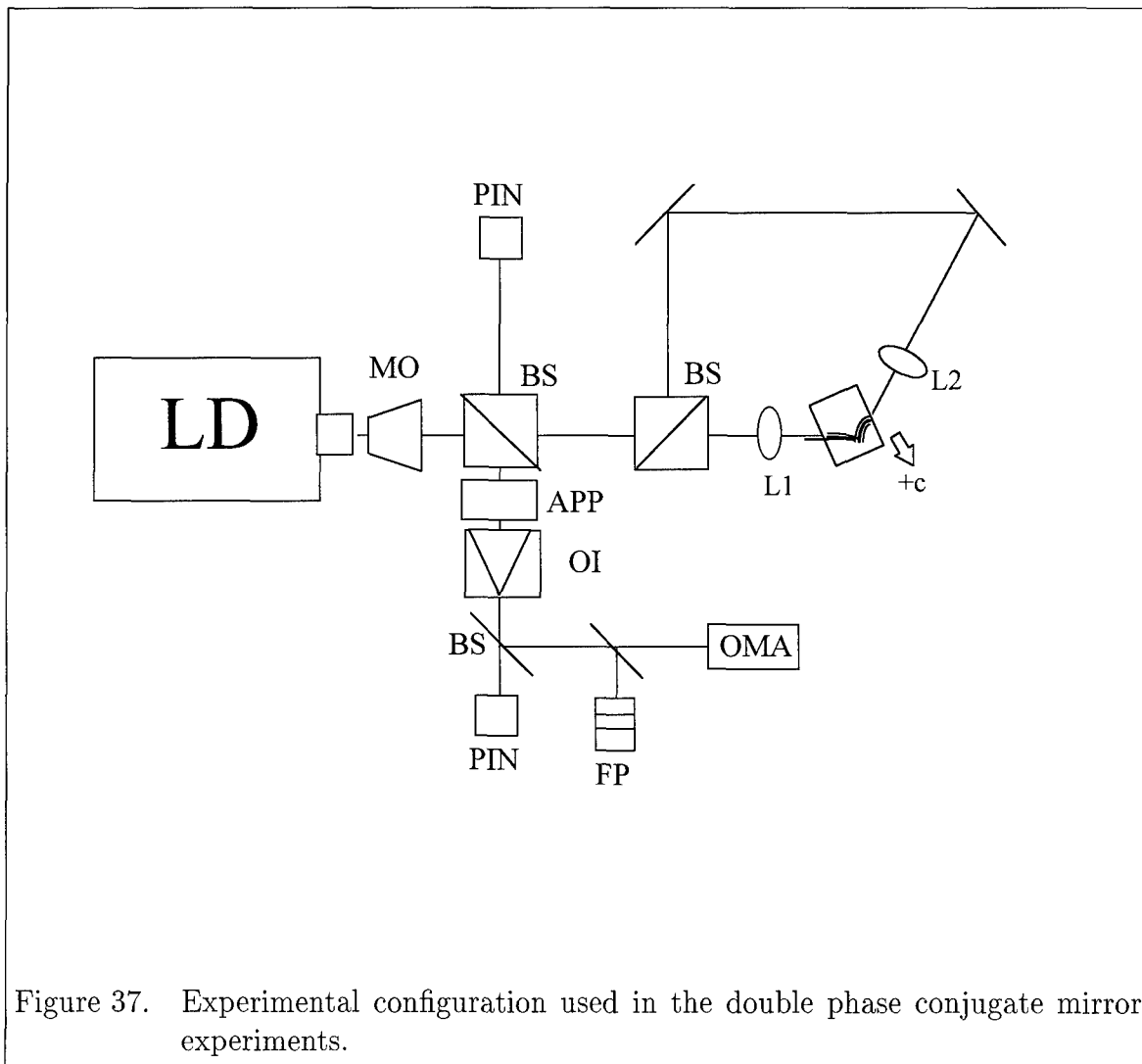
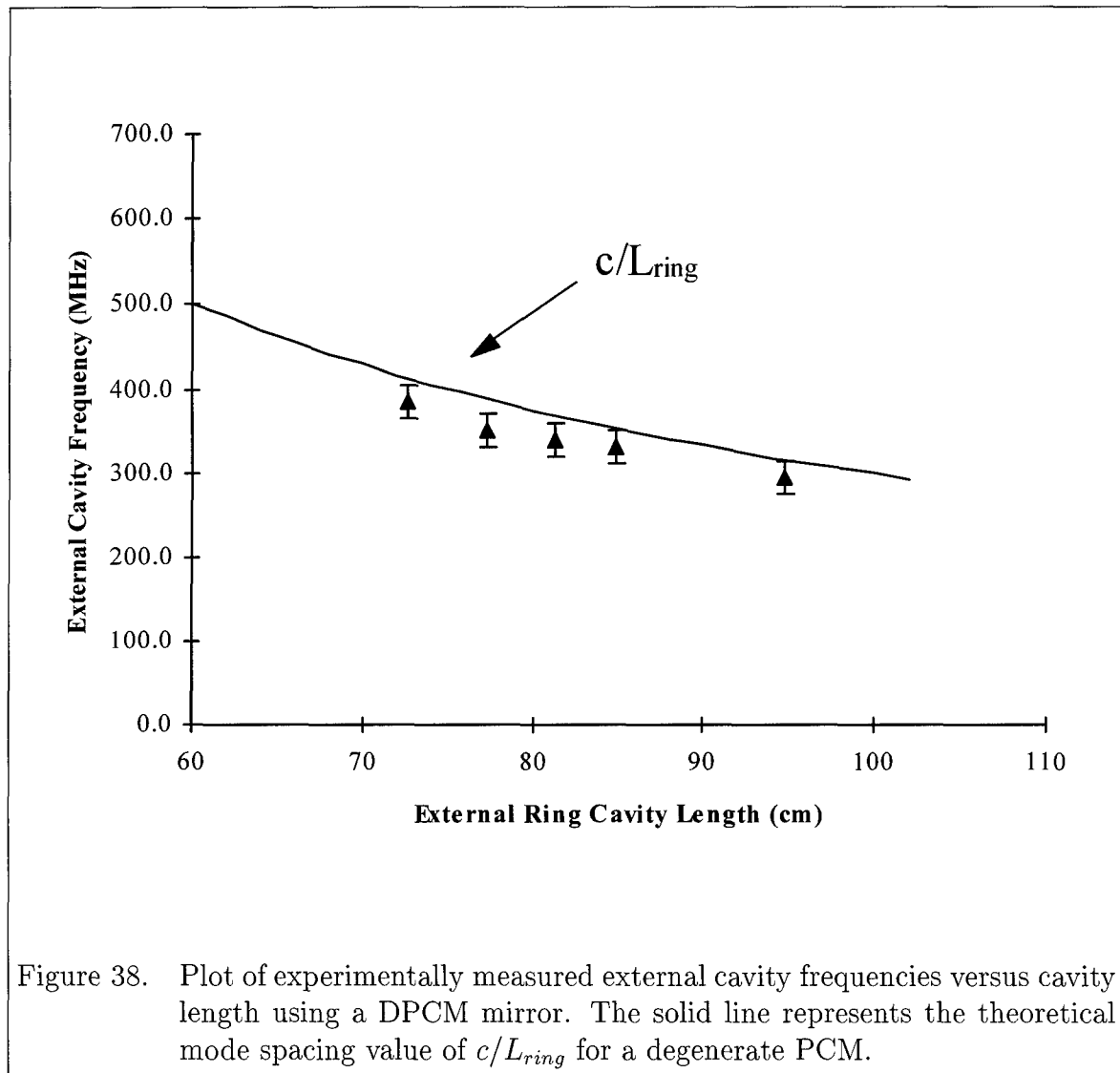


Figure 37. Experimental configuration used in the double phase conjugate mirror experiments.

phase front. This is different from the CAT geometry where the input and conjugate beams share the same path. Hence the round trip external cavity length of  $2L_{ext}$  as measured in the CAT PCM experiments now becomes  $L_{ring}$ , where  $L_{ring}$  is the total optical path length of the beam leaving the laser, passing through the crystal and then re-entering the laser. So for the degenerate DPCM, the theoretical external cavity frequency spacing is restated as  $c/L_{ring}$ , as shown in Figure 38.



The RF response of the DPCM was also tested in a similar manner to the CAT and normal mirror tests presented earlier. Figure 39 shows the two RF spectra of

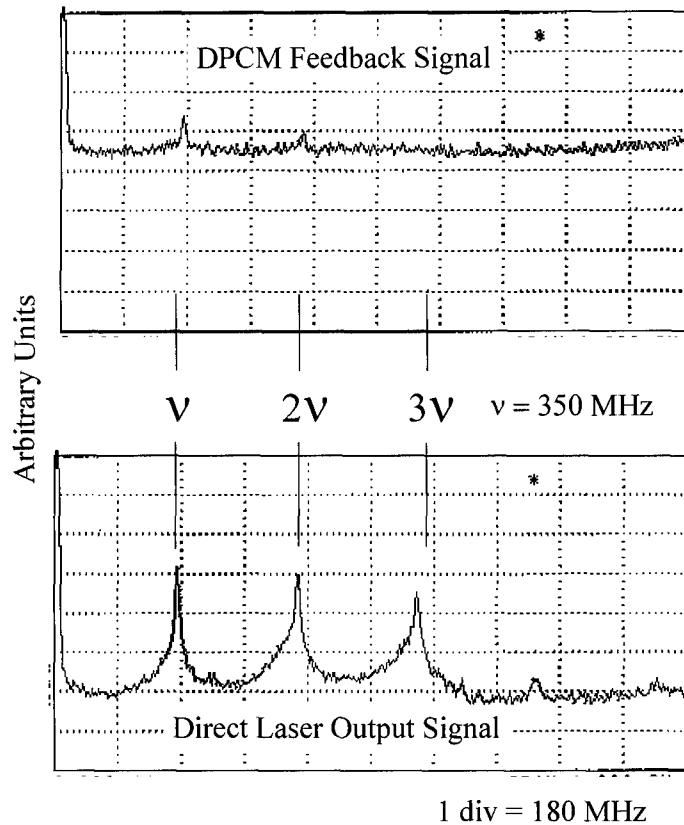


Figure 39. RF spectra of the feedback signal from the DPCM mirror and the laser output. Both signals contain the same frequency information indicating that there is no filtering being done by the DPCM mirror

the DPCM conjugate beam and the direct laser output. Since the conjugate levels were extremely low, the ND filter in front of the PIN diode sampling the laser output was removed to identify the RF signals clearly. Consequently, no comparison can be made between the amplitudes of the two spectra shown in the figure. However, the spectra do show the primary peak of  $\nu_{ext} = 350 \text{ MHz}$  which corresponds to  $L_{ring} = 85.7 \text{ cm}$ . A second weak peak in the DPCM spectrum can also be seen at  $2\nu_{ext} = 700 \text{ MHz}$ . No other peaks can be seen, but the sensitivity of the detector dramatically decreases for frequencies  $> 800 \text{ MHz}$ , which would explain the lack of peaks beyond

$2\nu_{ext}$ . The direct laser output spectrum shows this dramatic decrease in sensitivity for  $\nu = 1400$  MHz.

The next chapter takes the raw experimental data and makes a comparison against the predictions of the analytical solutions and computer models discussed in Chapters III and IV.

## VI. *Experimental and Modeling Results*

The culmination of this research was to provide insight into the processes of chaotic development in laser diodes with phase conjugate feedback and the validation of a computer model that could accurately predict this nonlinear behavior. This chapter explains the improvement made to the LKCON2.C model and compares the experimental data with the model outputs.

### 6.1 *Gain Saturation Improvement*

As mentioned in Section 4.2, an inaccuracy was identified with the original computer model for long external cavities. In this region, the model's prediction of the external cavity frequency quickly diverged from experimental data. The result for long cavities ( $L_{ext} \approx 15\text{--}30$  cm) was an external cavity frequency spacing that was underestimated by as much as one-fourth of the measured experimental frequency spacing. The same deficiency may also exist for short cavities; however, at short cavity lengths, the dominant route to chaos is through period doubling of the relaxation oscillation which is seen in the model. Simulations with short cavities show that the period doubling of the relaxation oscillation may actually mask the incorrect external cavity frequency since Level IV behavior is reached before the external cavity frequency undamps. Since no experimental data had been collected for  $L_{ext} < 15$  cm, validation of the external cavity frequency spacing below 15 cm was not possible.

The original computer model was based on an underlying assumption in the set of coupled nonlinear equations that the gain coefficient presented in Eq. (18) varied linearly with  $\Delta N$ . This first order linear approximation was an insufficient estimate of the gain coefficient. A more realistic representation requires the inclusion of a small signal gain saturation term  $Y$  to limit the effect of the electron hole number on the photon number as shown below.

The inclusion of the gain saturation term only affects  $da/ds$  and  $d\hat{N}/ds$  presented in Eqs. (52)-(54). The corrected set of nonlinear equations used in the LKCON2.C model are

$$\begin{aligned} \frac{da}{ds} = & \frac{1}{2} \left[ \frac{2\hat{N} + 1}{\sqrt{1 + Y\mathcal{P}(a^2 - 1)}} - 1 \right] a \\ & + \eta a(s - \tau) \cos(\phi(s - \tau) + \phi(s) - \phi_{PCM} - 2\Delta\omega(s - \tau/2)) \end{aligned} \quad (71)$$

and

$$T \frac{d\hat{N}}{ds} = \mathcal{P} - \hat{N} - \frac{(1 + 2\hat{N})}{\sqrt{1 + Y\mathcal{P}(a^2 - 1)}} a^2 \quad (72)$$

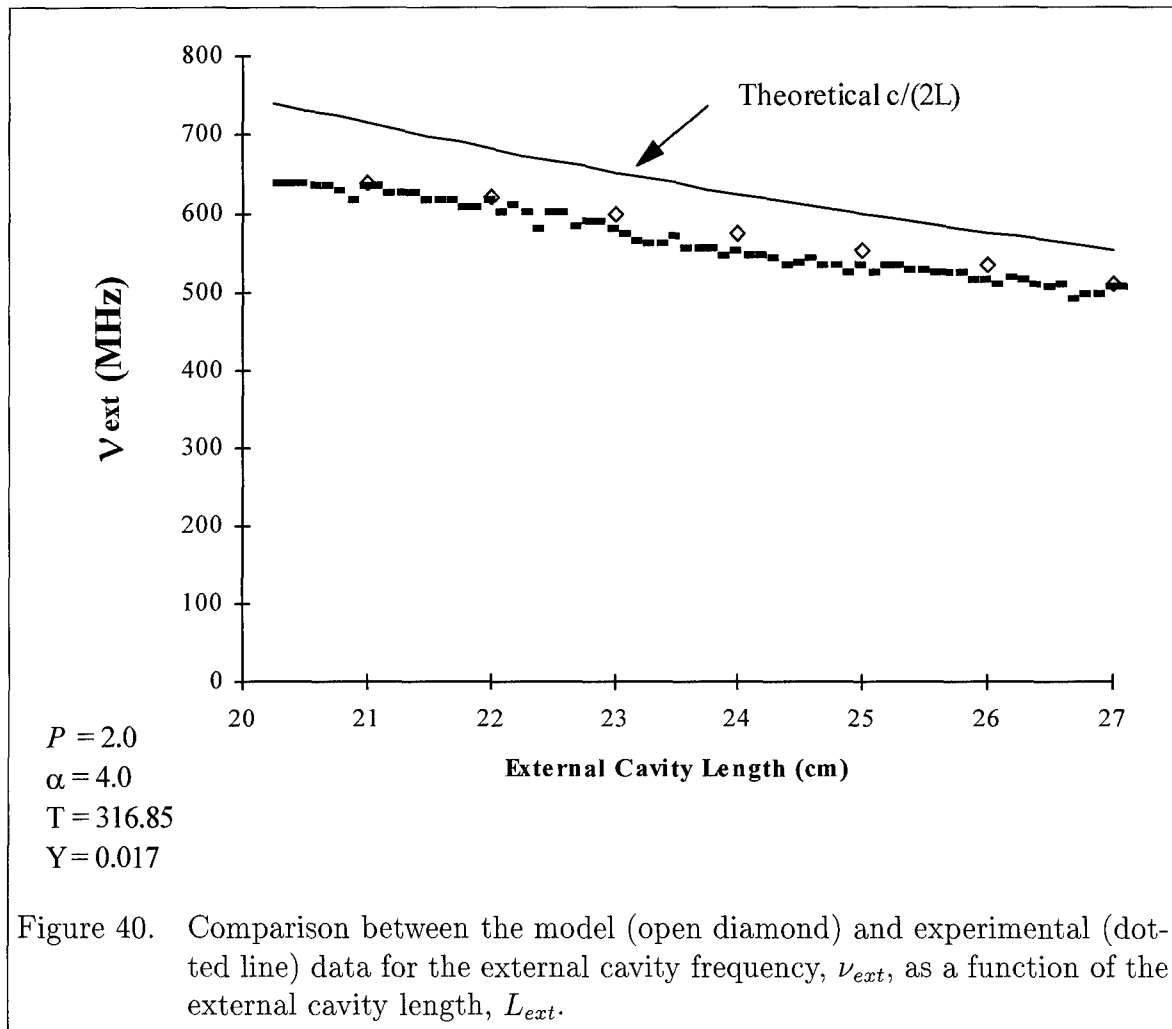
where  $Y$  is the dimensionless small signal gain saturation term ( $Y > 0$ ). Setting  $Y = 0.0$  recovers the original set of equations. Notice that for  $Y > 0$ , the amplitude of the field reduces the magnitude of the stimulated gain term included in  $\hat{N}$ . Increasing the value of  $Y$  causes the stimulated gain to saturate more quickly.

Simpson *et al* measured the small signal gain term to be  $Y = 0.017$  in a solitary laser diode similar to the SDL 5412 laser diode used in our experiments (24). It was found through comparison of the model and experimental data that a value of  $Y = 0.017$  was adequate for the SDL 5412. Even though it was beyond the scope of this research to specifically measure the small signal gain term, the excellent agreement between the computer model results and experimental data confirms that the value of  $Y = 0.017$  is reasonable.

With the gain saturation term added to the model a comparison between experimental data and model predictions can be accomplished. The next several sections present the analysis of the model and experimental data for the external cavity frequency spacing, changes in relaxation oscillation, locking ratio and feedback resonance. A qualitative comparison between the bifurcation map and experimental data is discussed in the last section.

## 6.2 External Cavity

Figure 40 shows the experimental (closed diamonds) and model data (dotted line) for the external cavity frequency as a function of the external cavity length in the range  $L_{ext} = 20\text{--}27$  cm. Also shown in the figure is the  $\nu = c/(2L_{ext})$  line which



is the theoretical mode spacing for degenerate phase conjugate feedback discussed by Auyeung *et al.* As shown in the figure, there is excellent overall agreement between the experimental and model results. The maximum difference between these two data sets is on the order of 25 MHz which is outside the 3 MHz resolution of the spectrum analyzer. The additional error between the data sets is attributed to the

limited accuracy of the FFT in the model ( $\pm 20$  MHz) and to a lesser extent, to an error in measuring the experimental external cavity ( $\pm 2$  mm).

Despite the small differences between the experimental and model data sets, there still remains an overall downward shift of the frequencies relative to the  $c/(2L_{ext})$  line. The downward shift in the frequency data cannot be attributed to a frequency bias of the RF spectrum analyzer. The analyzer was tested by splitting the solitary laser output and up-shifting one of the beam's frequency by 48 MHz using an acousto-optic modulator. The two beams were then recombined onto the PIN diode detector and the beat signal between the two laser beams was displayed on the RF spectrum analyzer. The manufacturer's specification for the instrument is a display resolution  $< 3$  MHz over the full span (DC-1.8 GHz) of the analyzer. The 48 MHz beat signal was detected well within this specification.

In addition, a horizontal translation of the experimental and model data to coincide with the  $c/(2L_{ext})$  line is not reasonable. Although a cavity length measurement error of  $\pm 2$  mm does exist, this error is well below the  $>3$  cm translation needed to move the experimental data onto the  $c/(2L_{ext})$  line. The most reasonable explanation for the overall downward shift of both the experimental and computer model data is the presence of other non-linear processes, such as gain saturation, that have not been included in Auyeung's analysis. The development of the  $c/(2L_{ext})$  line was based on the self-consistent solution of the radius of curvature of the laser beam in a simple cavity formed between the phase conjugate mirror and the gain medium. No other processes or limitations on the lasing medium or the phase conjugate mirror were considered. Furthermore, this downward shift in  $\nu_{ext}$  was also seen in the experimental results from the DPCM and to a lesser degree in the normal mirror experiments. This suggests the shift is strictly a laser and external cavity phenomenon and is independent of the feedback method.

### 6.3 Relaxation Oscillation and Locking Ratio

Figure 41 shows the comparison of the raw experimental data and the LK-CON2.C model for changes in the relaxation oscillation as the external cavity length is varied. The relevant model parameters are listed at the bottom of the figure. Both curves have the same  $\Delta L_{ext} = 3.5$  cm between successive transitions, as well as  $\Delta\nu_R = 500$  MHz as the max-min transition of the relaxation oscillation. The general features of the experimental data seem to be captured by the model curve. However, it is apparent from the figure that there seems to be a shift of the model data both in frequency and external cavity length relative to the experimental data.

Earlier in Section 3.3 it was shown that the Hopf frequency,  $\Omega_H$ , emerging out of the first Hopf bifurcation varied around the solitary relaxation value. As shown in Figure 41, this corresponds to a  $\nu_R = 4.28$  GHz for the model and 3.72 GHz for the experimental data. As a cross-check, the solitary relaxation frequency can also be extracted from the span between adjacent transitions. Since the span between resonant transitions is  $2\pi$ , an expected value for the experimental  $\nu_R$  using Eq. (68) is calculated to be:

$$\nu_R = \frac{c}{2\Delta L_{ext}} = 4.28 \text{ GHz} \quad (73)$$

This is obviously different than the measured value of  $\nu_R = 3.72$  GHz. Figure 42 shows a diagram of the F-P display for an arbitrary cavity length. From the display, it is not possible to determine which frequency is to be associated with adjacent F-P cavity modes. Since the FSR of the F-P is 8 GHz, the natural association is to assume that the two frequencies displayed are at 3.72 GHz. However, the model provides insight into the proper interpretation of the F-P display, which is overlapping modes with frequencies at 4.28 GHz. Therefore the data must be reinterpreted with a solitary relaxation frequency of 4.28 GHz, which also agrees with the calculated value based on the span between resonant transitions.

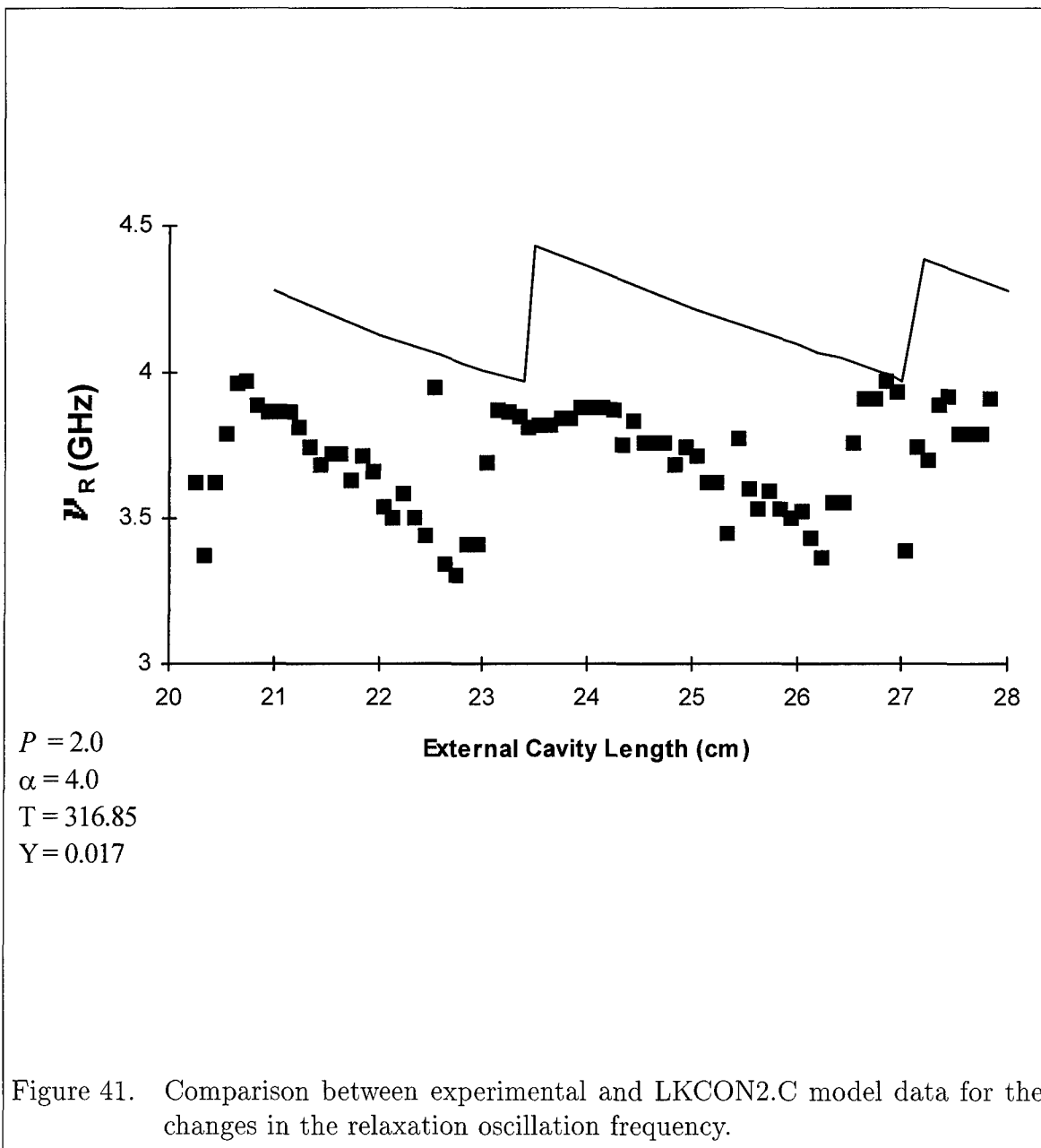


Figure 41. Comparison between experimental and LKCON2.C model data for the changes in the relaxation oscillation frequency.

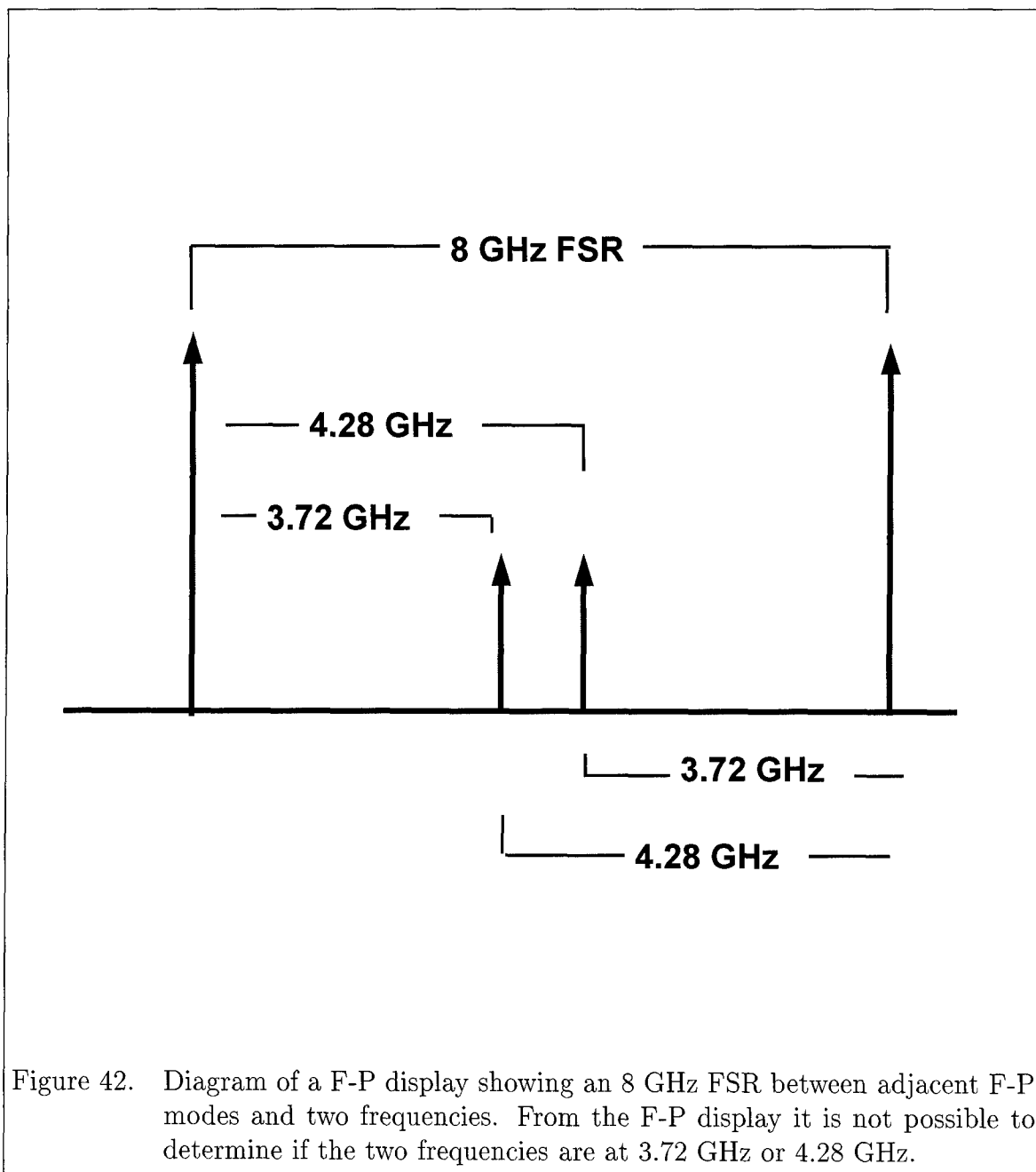
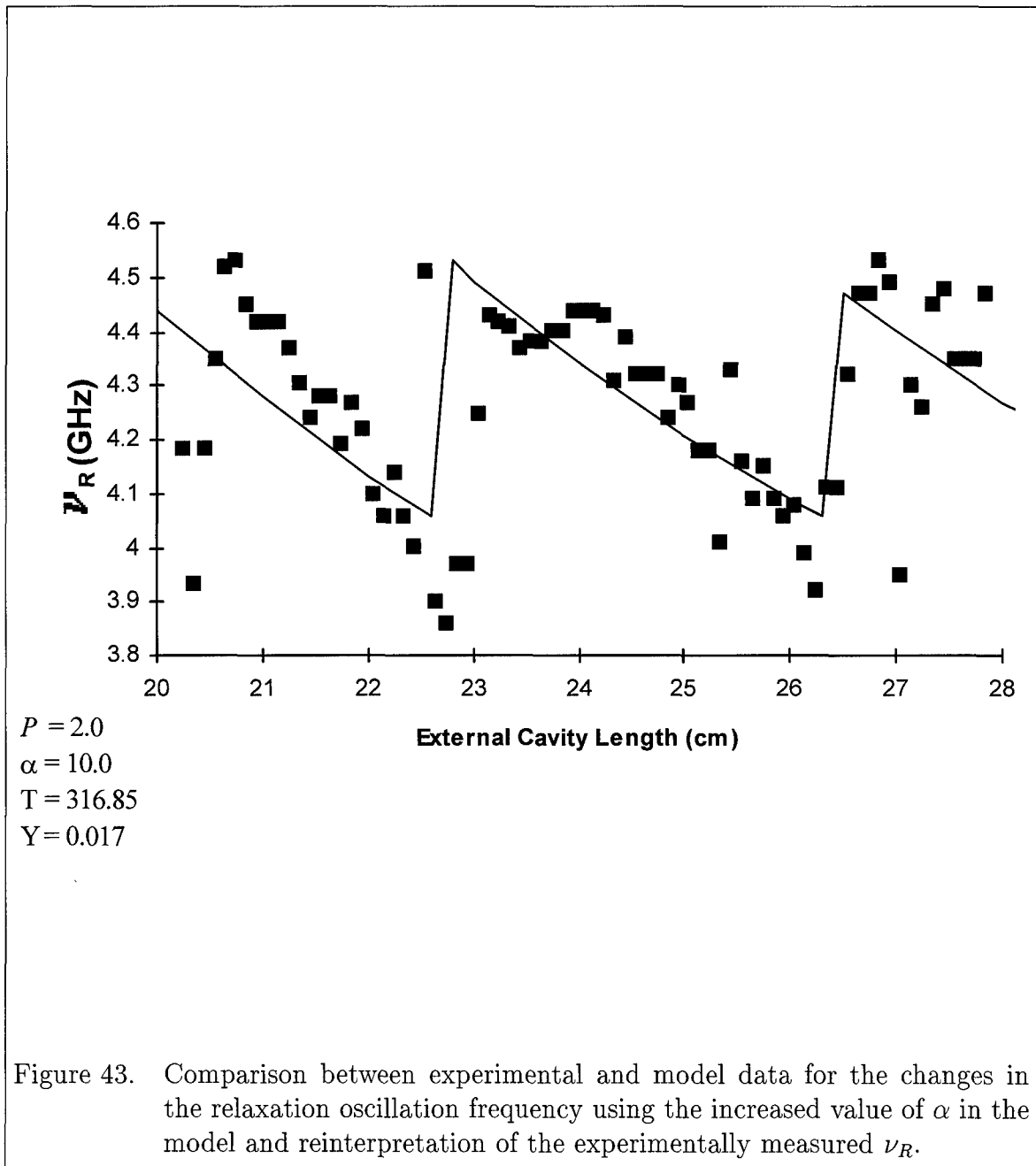


Figure 42. Diagram of a F-P display showing an 8 GHz FSR between adjacent F-P modes and two frequencies. From the F-P display it is not possible to determine if the two frequencies are at 3.72 GHz or 4.28 GHz.

The reinterpretation of the experimental data accounts for the vertical shift between the computer model and the experimental data. To address the horizontal differences, we need to apply the approximation of  $\alpha \rightarrow \infty$  made in Section 3.3. It was shown that this approximation simplifies the equations for the relaxation frequency emerging out of the first Hopf bifurcation. Accordingly, the  $\alpha$  parameter in the model was increased to a relatively high value of 10. The effect of the increase in  $\alpha$  was to shift the model data horizontally along  $L_{ext}$  so that the transition points at 22.7 and 26.2 cm match. In effect, the increase in  $\alpha$  reduces the dependency of Eq. (67) on the  $\cos(\vartheta)$  term in the denominator and hence transitions in  $\Omega_R$  (or  $\nu_R$ ) will occur when  $\Omega\tau = (2n + 1)\pi$ . Increasing  $\alpha$  beyond a value of 10 in the model has no significant contribution to the shift in the data since the denominator of Eq. (67) goes as  $\arctan(\alpha)$ . Figure 43 shows the result of incorporating both the increase of  $\alpha$  in the model data and the reinterpreted experimental values. The excellent agreement between the two curves is evident in the figure.

Figure 44 shows the integer values of the locking ratio for the experimental and model data. The locking ratio values for the model data have been calculated using the  $\alpha = 10$  model data and the ratios for the experimental data have been calculated using the relaxation frequencies shown in Figure 43. As shown in Figure 44, the graph of the experimental data has a whole integer trend with values of 7, 8, and 9 over the range of  $L_{ext} = 20\text{--}28$  cm while the model data has half-integer values of 6.5, 7.5 and 8.5 over the same range. Earlier in the external cavity frequency comparison, the experimental data had been shown to be on the order of 25 MHz below the model data. This small difference is significant enough to increase the locking ratio of the experimental data by a half-integer. Re-scaling the experimental data to coincide with the model trend would lower the experimental locking ratio values by a half integer. Therefore, the disparity in the locking ratios is attributed to the small, but consistent, differences in the external cavity frequency between the model and the experimental data.



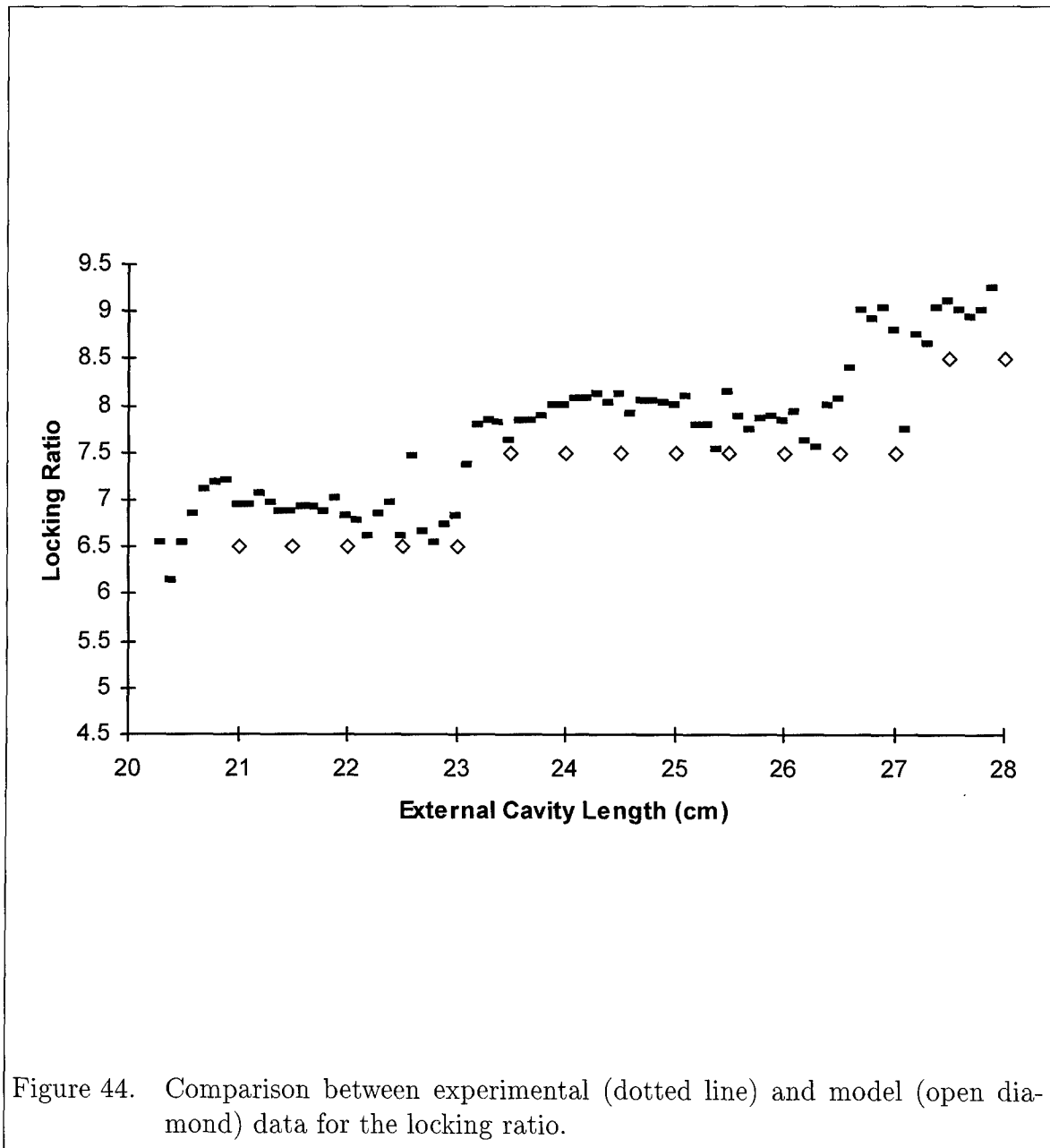


Figure 44. Comparison between experimental (dotted line) and model (open diamond) data for the locking ratio.

#### 6.4 Feedback Resonance

The last comparison to be discussed is between the experimental external cavity resonance data and Eq. (69) describing  $\eta_H$  using the approximation  $\alpha \rightarrow \infty$ . Figure 45 compares the measured experimental and model results for external cavity lengths of 20–28 cm. The experimental phase conjugate feedback power was normalized using Eq. (48) for  $\kappa$ . The laser cavity coupling efficiency in Eq. (48) was assumed to be  $\eta_c = 1$  and a value for the laser facet reflectivity,  $R_2 = 0.3$ , was chosen based on manufacturer specifications. The resultant value for  $\kappa$  was then rescaled using the scaling presented in Section 3.1 to convert the experimentally measured feedback power into the dimensionless parameter  $\eta$ .

The significant attribute of this figure is the overall fit of the periodicity between the data sets. Qualitatively, Eq. (69) accurately captures the general trend of the data. Again, the 3.5 cm peak-to-peak resonance spacing in the experimental data suggests a calculated  $\nu_R = 4.28$  GHz. The model representation shown in the figure was calculated using  $\nu_R = 4.28$  GHz which yields an excellent fit to the data. This value for the relaxation frequency also agrees with the value established earlier in Section 6.3 when the LKCON2.C model outputs for the relaxation frequency were compared to the experimental values. For comparison, using a relaxation oscillation value  $\nu_R = 3.72$  GHz in Eq. (69) yields a resonance spacing of 4 cm, which was originally shown in Figure 10 when the equation for  $\eta_H$  was first introduced. A curve fit to the experimental data with a resonance spacing of 4 cm is poor since only one peak can be matched with that spacing.

A notable conclusion from this graph is that the experimental data, the LKCON2.C model, and the approximate solution for  $\eta_H$  given in Eq. (69) all agree over this range. Since Eq. (69) offers a convenient and compact form to investigate cavity resonance behavior, a validating test would be to apply the external cavity plot to a second set of data and look for resonance point matches. As mentioned in the experimental descriptions, external cavity resonance data were also taken indepen-

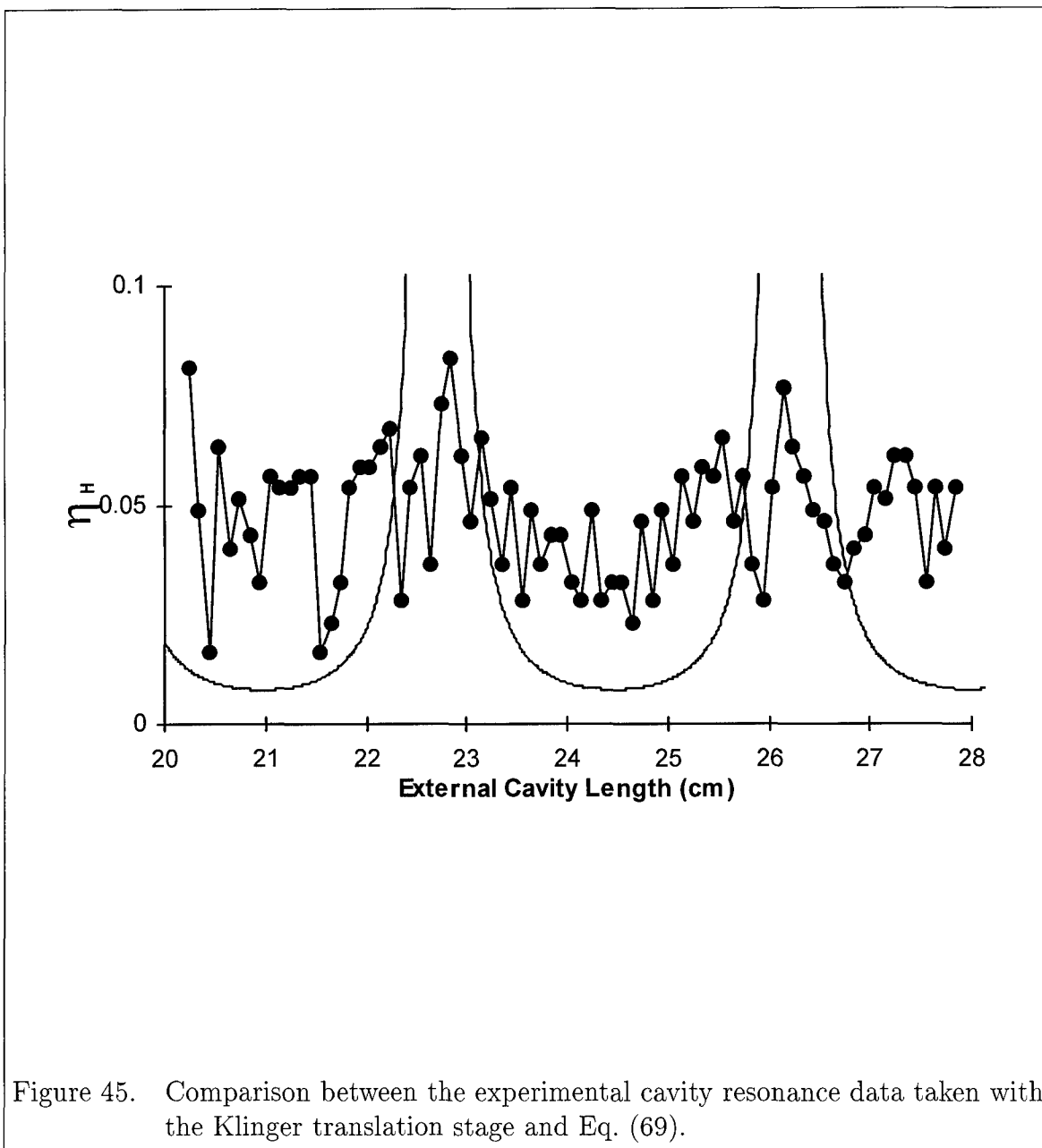


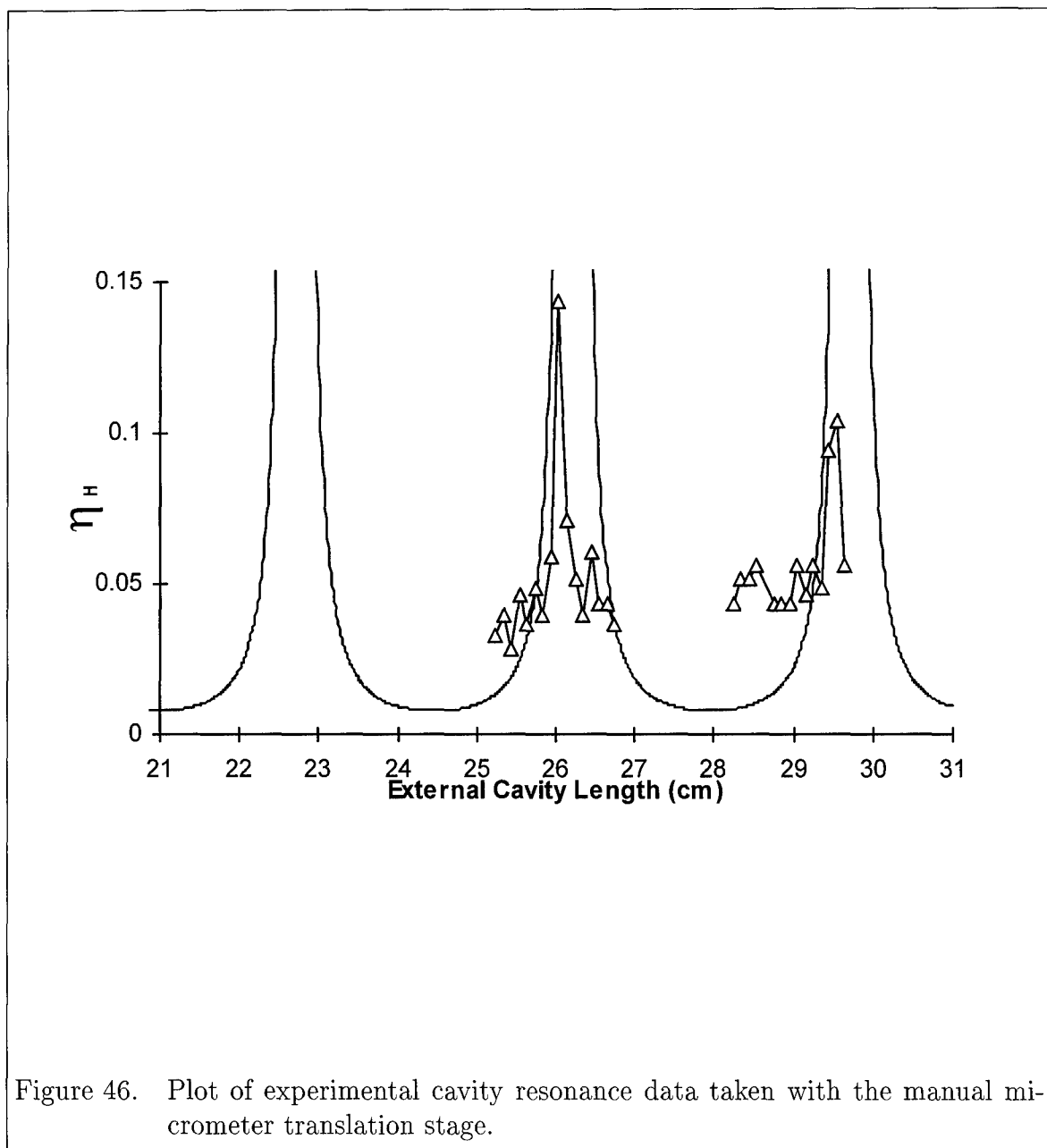
Figure 45. Comparison between the experimental cavity resonance data taken with the Klinger translation stage and Eq. (69).

dently using a manual translation stage which only had a 2 cm throw. Figure 46 plots the translation stage data against Eq. (69) for the ranges 25–27 cm and 28–30 cm which accurately shows the correlation between the experimental data and the approximate solution.

### 6.5 Bifurcation Diagram

The direct experimental construction of a bifurcation diagram, depicting the extreme values of the laser output amplitude versus feedback rate, was not possible due to data acquisition equipment limitations. However, a qualitative comparison between experimental data and the LKCONBI2.C model was accomplished and used throughout the experimental work. The comparison uses experimental RF and F-P spectra to identify key events in the model bifurcation map, such as relaxation oscillation undamping, the external cavity frequency appearing and total chaos. The experimental feedback power associated with these spectral events can then be used to locate the position in the model bifurcation map. This procedure was also used in reverse where model predictions could be used to forecast expected experimental values at least to within an order of magnitude.

Figure 47 shows the model bifurcation map for  $L_{ext} = 20$  cm. The diamonds overlaid on top are the locations of the key events found in the experimental spectra. The phase conjugate feedback power has been normalized in a similar manner as described in the previous section so that the feedback power is now displayed as  $\eta$ . Table 8 lists the values of the key events for the experimental and model data. The emergence of the external cavity frequency at  $\eta^{model} = 0.0065$  is difficult to see in the map due to the limited resolution of the graphic, but was confirmed by examining the model RF spectrum. No attempt was made to calibrate the sensitivity of the F-P or spectrum analyzer instruments, therefore, exact pinpointing of the bifurcation points in the experimental data is not reasonable. Nonetheless, there is a general agreement between the experimental data and the LKCONBI2.C model.



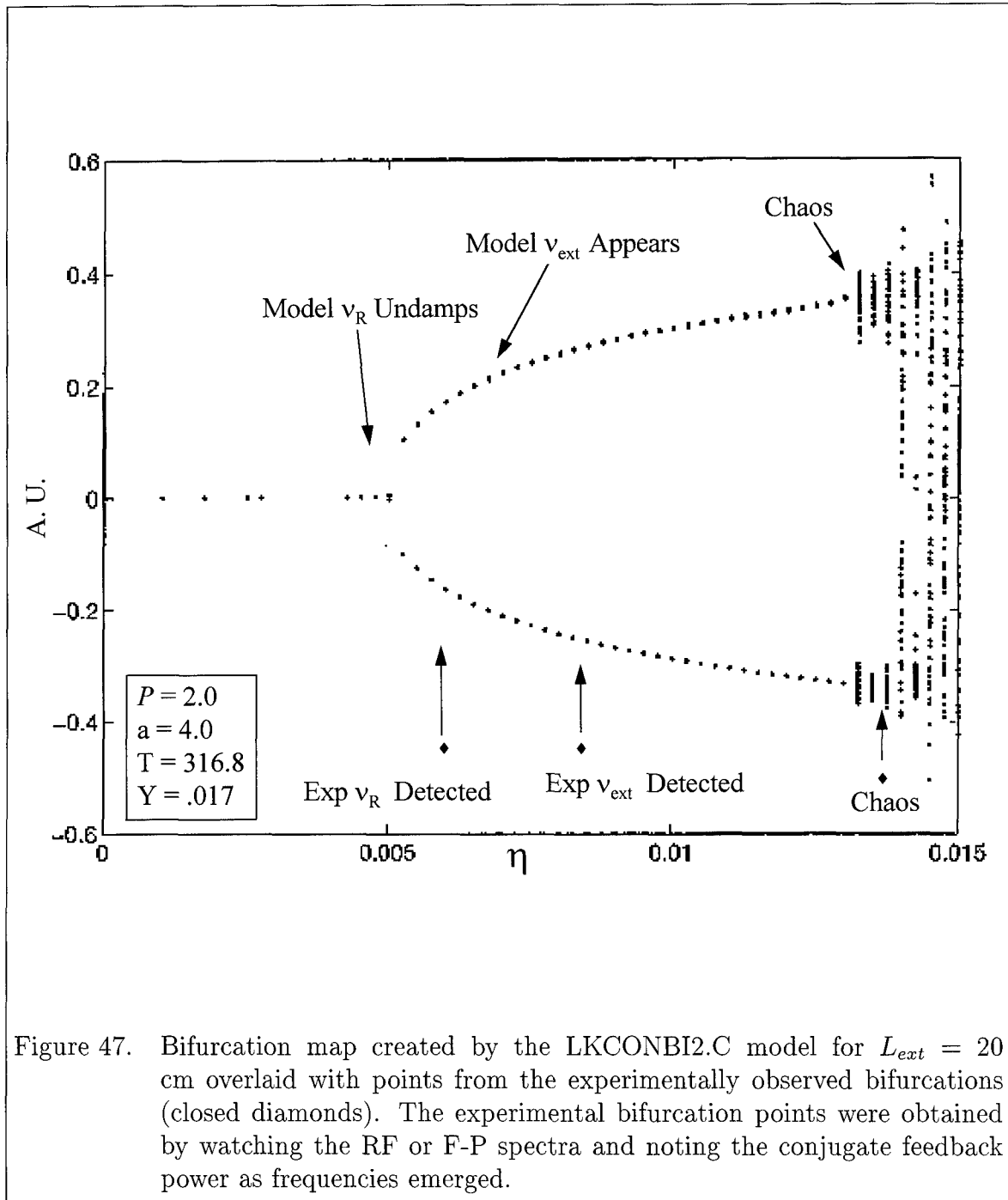


Figure 47. Bifurcation map created by the LKCONBI2.C model for  $L_{ext} = 20$  cm overlaid with points from the experimentally observed bifurcations (closed diamonds). The experimental bifurcation points were obtained by watching the RF or F-P spectra and noting the conjugate feedback power as frequencies emerged.

Table 8. Identification of key bifurcation events shown in Figure 47.

Key Event	$\eta^{model}$	$\eta^{exp}$
Relaxation Oscillation Emerges	0.0051	0.0063
External Cavity Frequency Emerges	0.0065	0.008
Full Chaos	0.013	0.014

This simple comparison is obviously not a complete validation of the LK-CONBI2.C computer model. Nevertheless it demonstrates good qualitative agreement between predicted results and experimental data. In order to evaluate the model quantitatively, experimental reconstruction of the bifurcation maps is essential.

## VII. *Conclusions and Recommendations*

Presented in this research is an examination of the nonlinear response of a laser diode subject to weak degenerate phase conjugate feedback. The development of chaos in the laser diode was investigated through numerical computer modeling to predict the laser output spectra and through experimental verification of the computer models using a BaTiO<sub>3</sub> crystal as the phase conjugate feedback mirror. Two methods of establishing the PCM were used in the experiments to compare the feedback effects due to self-pumping the BaTiO<sub>3</sub> crystal and by double phase conjugation.

It was shown that a phase conjugate mirror in either the self-pumped or double pumped configuration with BaTiO<sub>3</sub> has a frequency response sufficient to reflect the RF external cavity frequencies contained in the laser output. Although BaTiO<sub>3</sub> is inherently a slow crystal in forming the holographic grating needed to establish the phase conjugate mirror, once the grating is established it can support small perturbations in the laser output as the laser evolves into a chaotic state. Hence the BaTiO<sub>3</sub> PCM performs as “fast” as a normal dielectric mirror. In addition, the feedback parameter  $\kappa$  that couples the external cavity delay into the rate equation for the laser photon number can be modeled accurately as a time independent parameter.

The experimental data also verified model results using variations of the external cavity as the control variable. Through the use of experimental data it was clear that the model needed to be modified to include gain saturation of the laser medium to show accurately the dependency of the external cavity frequency on the length of the external cavity. Without including gain saturation, model predictions of  $\nu_{ext}$  for long external cavities grossly underestimated values obtained experimentally. Therefore, the electron-hole gain coefficient, initially assumed to vary linearly with  $\Delta N$ , actually has a more complex dependency. Furthermore, the inclusion of the gain saturation on the electron-hole population corrected the model for other

effects such as frequency locking between the relaxation oscillation and external cavity frequency, changes in the relaxation oscillation frequency, and feedback resonance of the external cavity. These phenomena were all verified experimentally using the self-pumped phase conjugate geometry.

The experimental and analytical results presented in this document provide valuable insight into areas of future research. As discussed earlier, there is excellent agreement between model predictions and experimental data for the case of degenerate phase conjugate feedback. The investigation of the onset of chaos from non-degenerate phase conjugate feedback would be most advantageous for a more robust computer model. Non-degenerate phase conjugate feedback can produce effects on the laser not possible with degenerate feedback or feedback from a normal dielectric mirror. The fold bifurcation, external cavity mode spacing of  $4L_{ext}$  and locking of the laser frequency to the pump frequency are all unique areas that need experimental verification for the models.

Moreover, it was discussed earlier that the LKCON2.C model was the only model verified experimentally due to the limitation of the data acquisition capacity in the experimental equipment. The LKCONBI2.C bifurcation model should also be experimentally verified for completeness. This will require a data acquisition system to include an ultra-fast photodiode with a cut-off frequency  $> 8$  GHz and a matching analog-to-digital (A/D) digitizer to record the amplitude time series for the bifurcation map. Also, an RF spectrum analyzer with at least a 6 GHz bandwidth is recommended to capture the external cavity frequency and the relaxation oscillation frequency in the same spectrum. This would allow comparison of the amplitudes of the two frequencies in addition to pinpointing the level of feedback when each frequency emerges while minimizing relative scale errors associated with separate equipment. These bifurcation points could not be adequately identified in the current experimental equipment since only  $\nu_{ext}$  was collected in the RF spectra. Although there was excellent agreement in the frequency content between the

RF and F-P spectra, the sensitivity and resolution of the F-P are less than the RF spectrum analyzer.

Two additional areas for proposed research include the experimental investigation of short cavities ( $\nu_{ext} > \nu_R$ ) and the experimental determination of the small signal gain parameter. The investigation of short cavities poses a challenge to engineer optics into an external cavity with lengths shorter than 5 cm. These short external cavities can also further validate the fast response of the PCM by driving the external cavity frequency higher than the relaxation oscillation. If indeed the phase conjugate return beam contains the same frequency content as the laser output, even for short cavities, then the BaTiO<sub>3</sub> PCM behaves nearly instantaneously.

One of the conclusions drawn from this research is that the small gain saturation term plays an important role in modeling nonlinear behavior due to phase conjugate feedback. The value of the gain saturation term used in this research was based on previous work by Simpson *et al* on a similar laser diode. A recommended area of future research is to investigate the gain saturation process in a single mode laser diode to fully understand the nonlinear effects on the gain due to feedback and improve the computer models.

In conclusion, the data presented in this research has increased the understanding of the onset of deterministic chaos in a semiconductor laser diode with phase conjugate feedback. As the theory and computer models describing nonlinear behavior matures, eventual control of the chaotic laser will be practical. Being able to control the output of a chaotic laser opens real possibilities for encoding and encrypting information in the chaos which could transition a once undesirable condition into a useful product.

## Appendix A. MathCad Templates

MathCad template to examine the frequency and feedback rate at the Hopf bifurcation point "Cap Omega" is the dimensionless frequency emerging from the Bifurcation and "omega" is the scaled frequency in GHz. "Eta is the dimensionless feedback rate at the Hopf point.

Constant Parameters:

Pumping:  $P := 2.0$

Speed of Light (cm/sec):  $c := 3 \cdot 10^{10}$

Alpha:  $\alpha := 4.0$

Photon Lifetime (sec):  $\tau_p := 4.166 \cdot 10^{-12}$

Carrier Lifetime (sec):  $\tau_N := 1.32 \cdot 10^{-9}$

Step Size of L increment:  $\Delta L := .01$

Max L:  $L_{\max} := 31$     Min L:  $L_{\min} := 20$

Number of steps taken:  $N := \frac{L_{\max} - L_{\min}}{\Delta L} \quad N = 1.1 \cdot 10^3$

External Cavity Length (cm):  $L := L_{\min}, L_{\min} + \Delta L .. L_{\max}$

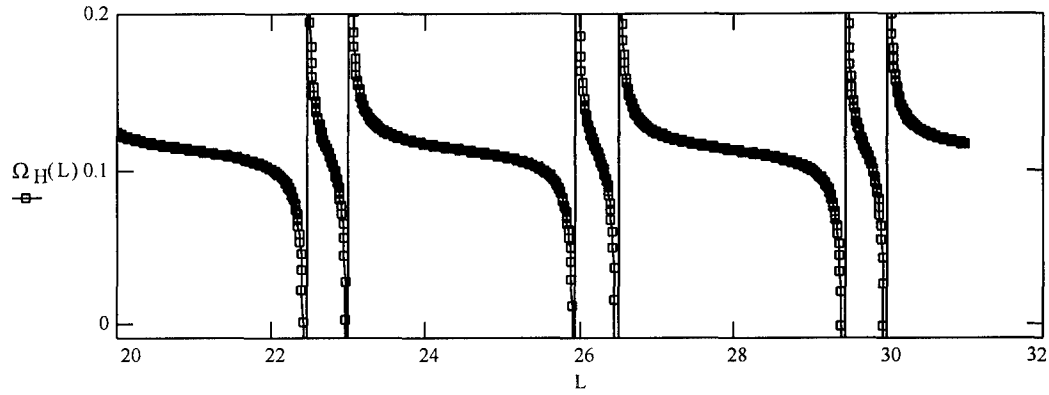
Array Index for saving:  $i := 0 .. N - 1 \quad j := 0 .. 1$

Other Definitions:

$$\varepsilon = \frac{\tau_p}{\tau_N} \quad T = \frac{\tau_N}{\tau_p} \quad \theta = \text{atan}(\alpha) \quad \tau(L) = \frac{2 \cdot L}{c \cdot \tau_p}$$

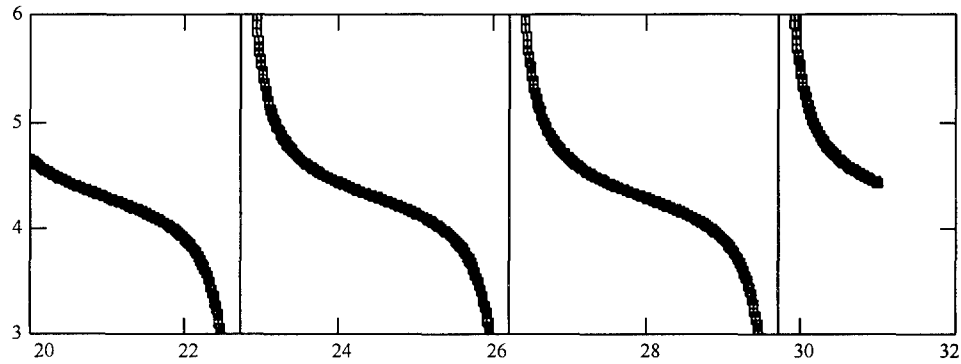
Solitary Relaxation Frequency:  $\omega_R := \sqrt{2 \cdot \frac{P}{T}}$      $\frac{\omega_R}{\tau_p \cdot 2 \cdot \pi} = 4.292 \cdot 10^9 \quad \text{Hz}$   
(dimensionless)

$$\Omega_H(L) := \omega_R - \frac{\varepsilon \cdot (1 + 2 \cdot P) \cdot \sqrt{1 + \alpha^2} \cdot \cos(\theta + \text{atan}(\alpha)) \cdot \sin(\omega_R \cdot \tau(L))}{4 \cdot \left( \sqrt{1 + \alpha^2} \cdot \cos(\theta + \text{atan}(\alpha)) \cdot \cos\left(\frac{\omega_R \cdot \tau(L)}{2}\right) - \cos(\theta) \right)}$$



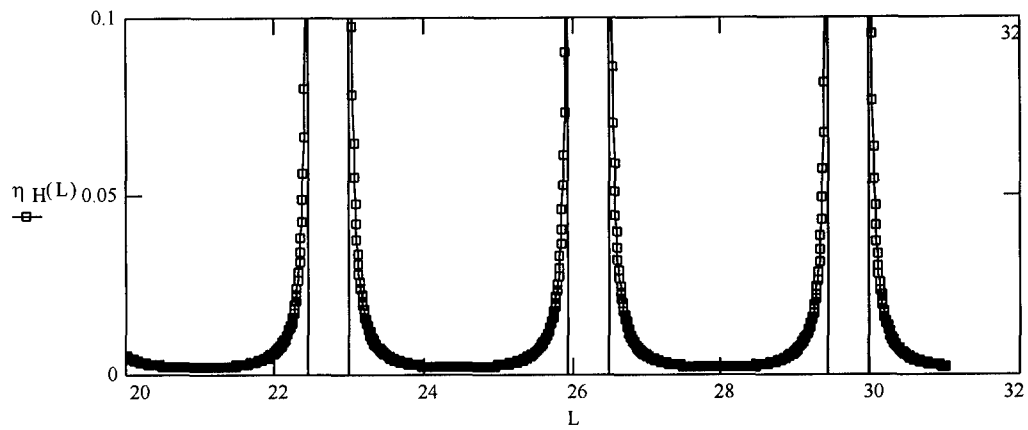
For the condition that alpha tends to infinity:

$$\omega_H(L) := \omega_R \cdot \left( 1 - \frac{1}{2} \cdot \frac{1 + 2 \cdot P}{2 \cdot P} \cdot \omega_R \cdot \tan\left(\frac{\omega_R \cdot \tau(L)}{2}\right) \right)$$



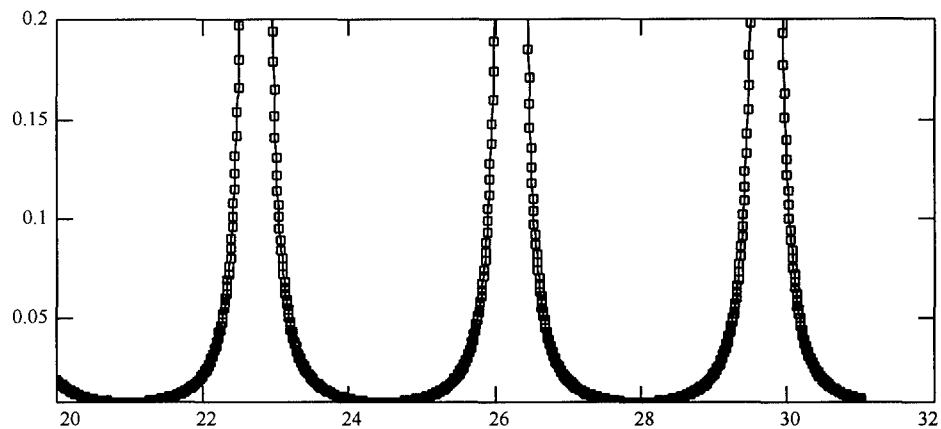
Feedback rate at the Hopf Point:

$$\eta_H(L) := \frac{\varepsilon \cdot (1 + 2 \cdot P)}{2 \cdot \left( \sqrt{1 + \alpha^2} \cdot \cos(\theta + \text{atan}(\alpha)) \cdot \cos\left(\frac{\omega_R \cdot \tau(L)}{2}\right)^2 - \cos(\theta) \right)}$$



Using the assumption that alpha tends to infinity, "Eta" reduces to:

$$\eta(L) := \frac{1 + 2 \cdot P}{2 \cdot P} \cdot \frac{\omega R^2}{2 \cdot \cos\left(\frac{\omega R \cdot \tau(L)}{2}\right)^2}$$



Now save the eta values:

$$ETA_{i,0} := L_{min} + \Delta L \cdot i \quad ETA_{i,1} := \eta(L_{min} + \Delta L \cdot i)$$

WRITEPRN(eta) := ETA

Constants:  $c = 3 \cdot 10^{10}$   $\tau_p = 1 \cdot 10^{-12}$

Laser Parameters: Measured Relaxation Freq:  $\nu_r = 3.72 \cdot 10^9$

Scaled Relaxation Freq:  $\omega_r = 2 \cdot \pi \cdot \nu_r \cdot \tau_p$   $\omega_r = 0.02337$

Alpha:  $\alpha = 4$

Pumping Term:  $P = 2$

External Cavity Length (cm):  $L_{ext} = 3.0$

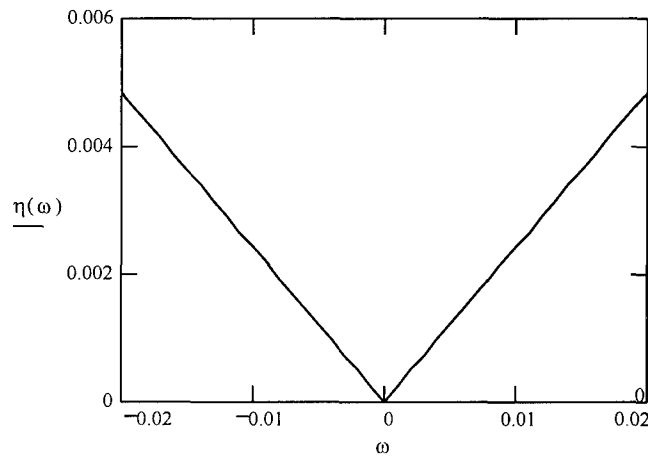
Scaled External Cavity Length:  $\tau = \frac{2 \cdot L_{ext}}{c \cdot \tau_p}$   $\tau = 200$

Calculated External Cavity Frequency:  $\nu_{ext} = \frac{c}{4 \cdot L_{ext}}$   $\nu_{ext} = 2.5 \cdot 10^9$

Range of values for omega:  $\omega = -.02, .019 \dots .02$

Fold bifurcation Lines  
which show the amount  
of feedback, eta:

$$\eta(\omega) = \frac{|\omega|}{\sqrt{1 + \alpha^2}}$$

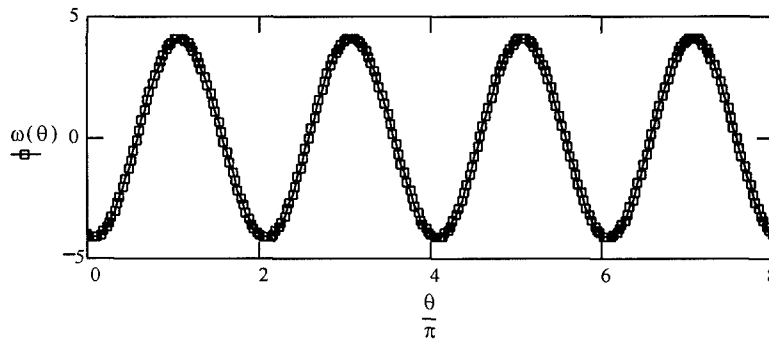


Graphical Solution to frequency and phase lock equation:

Range of values for Theta:  $\theta := 0, .1 .. 8 \cdot \pi$

Let eta = 1       $\eta := 1$

Phase lock equation:       $\omega(\theta) := -\eta \cdot \sqrt{1 + \alpha^2} \cdot \sin(\theta + \text{atan}(\alpha))$



## Appendix B. LKCONBI2.C Source Code

```
/*-----lkconbi2.c-----*/
/*---Performs bifurcations for the---Lang Kobayashi-----*/
/*--model of semiconductor equations with-----*/
/*---conjugate feedback-----*/
/* and gain saturation */
/*--This is a code for delay-differential equations-----*/
/*---with the appropriate scalings performed-----*/
/*-----10 Aug 95-----*/
/*--- Original LKCONBI.C program developed by */
/*-----Dr Gavrielides Phillips Laboratory */
/* Modified by G. Hengst 5 Dec 96 to read in */
/* default parameters so that the codes does not */
/* have to be re-compiled on every constant change */
/* Modified by G. Hengst 22 Apr 97 */
/* to include gain saturation effects */

#include <math.h>
#include <stdio.h>
#include <malloc.h>

/* ***** this section is now read in from LKCONBIF.CFG file */
/* #define BEGIN 0.0 */
/* #define END 500.0 */ /* 500.0 */
/* #define EXTIME 400.0 */ /* 400.0 */
/* #define NPOINTS 16000 */ /* 16000 */
/* #define KMAX 1 */
/* #define HTAMIN 0.00018 */ /* .00003 .0017 */
/* #define HTAMAX .001 */ /* .001 .0006 */
/* #define HTASTEP 100 */

/* #define tao 1428.57 */ /* 4000.0 */
/* #define pi 2.33 */ /* .75 */
/* #define alfa 4.0 */ /* 10.0 */
/* #define taoex 1095.23 */ /* 49.67 132.460/2.0 */
/* #define delta 0.0 */
/* #define phipcm 0.0 */
/* #define model 1 */ /* model=0 phase equation */
/* model=1 full model */
```

```
float BEGIN, END, Y, EXTIME;
int NPOINTS, KMAX;
float HTAMIN, HTAMAX, Y;
int HTASTEP;
float tao, pi, alfa, taoex, delta, phipcm, ext_length;
float carrier_life, photon_life;
int model, usernd;
```

```
void rk dumb();
void rk4();
float *vector();
void free_vector();
void nrerror();
float **matrix();
void free_matrix();
int init_stack();
int write_stack();
float ran1();
```

```
float **stack,*save;
float lastde=0.0,taupi;
FILE *outfile;
FILE *cfgfile;
int nstack,iseed=-872581;
struct given {
    int dim;
    float out;
} data;
```

```
/* main(argc,argv) */
main(void)
```

```
/*int argc;
```

```

char *argv[]; */

{
void derivs();
void exit();
float *ystar;
register int i;
float h,tau,tpi;
int dimen,j;

/*-----*/
/* This section has been commented out since
   the default output file is LKCONBIF.DAT

if (argc != 2)
    printf("Usage: Program OutputFile ..
Now exiting system...\n");
    exit(1)

if ((outfile=fopen(argv[1],"a+t"))==NULL
    outfile=fopen(argv[1],"at")
***** */

/* Input default values for constants from LKCONBIF.CFG */

cfgfile = fopen("lkconbif.cfg", "r");
/* open the config file for reading */

if (cfgfile == NULL){
printf("LKONBIF.CFG file not found...terminating \n");
abort();
}
fscanf(cfgfile, "%f", &BEGIN);
fscanf(cfgfile, "%f", &END);
fscanf(cfgfile, "%f", &EXTIME);
fscanf(cfgfile, "%i", &NPOINTS);
fscanf(cfgfile, "%i", &KMAX);
fscanf(cfgfile, "%f", &HTAMIN);
fscanf(cfgfile, "%f", &HTAMAX);
fscanf(cfgfile, "%i", &HTASTEP);

```

```

/*fscanf(cfgfile, "%f", &tao); */

fscanf(cfgfile, "%f", &pi);
fscanf(cfgfile, "%f", &alfa);
fscanf(cfgfile, "%f", &ext_length);
fscanf(cfgfile, "%f", &delta);
fscanf(cfgfile, "%f", &phipcm);
fscanf(cfgfile, "%e", &photon_life);
fscanf(cfgfile, "%e", &carrier_life);
fscanf(cfgfile, "%i", &model);
fscanf(cfgfile, "%f", &Y);
fscanf(cfgfile, "%i", &usernd);

tao = carrier_life/photon_life;
taoex = (2.0 * ext_length)/(3.0e10 * photon_life);

printf("\n BEGIN: %f",BEGIN );
printf("\n END: %f",END );
printf("\n EXTIME: %f",EXTIME );
printf("\n NPOINTS: %i", NPOINTS);
printf("\n KMAX: %i",KMAX );
printf("\n HTAMIN: %f", HTAMIN );
printf("\n HTAMAX: %f", HTAMAX);
printf("\n HTASTEP: %i",HTASTEP );
printf("\n tao: %f",tao );
printf("\n pi: %f",pi );
printf("\n alfa: %f", alfa );
printf("\n taoex: %f",taoex );
printf("\n delta: %f",delta);
printf("\n phipcm: %f", phipcm);
printf("\n photon_life: %e", photon_life);
printf("\n carrier_life: %e", carrier_life);
printf("\n Y: %f", Y);
printf("\n model: %i", model);
printf("\n Random: %i \n", usernd);

if (NPOINTS == 0){
    printf("Values not properly read into program...terminating \n");
    abort();
}

outfile = fopen("lkconbif.dat", "w");

```

```

/*-----*/

/*-----*/
data.dim=4;
if(model==0) tau=taoex*sqrt(2.0*pi/tao);
if(model==1) tau=taoex*sqrt(2.0*pi/tao);
printf("\n tau: %f \n", tau);

dimen=4;
taupi=tau;
tpi=4.0*atan(1.0);
/*   However final printed time is in units of tp   */

/*-----*/
h=(END-BEGIN)/(NPOINTS*KMAX);
nstack=init_stack(tau,h,dimen);
ystar=vector(1,data.dim);
save=vector(1,data.dim);

/*-----*/
/*-----initial conditions-----*/
/*-----*/

ystar[1]=0.10;          /*9.8;    .000645217;*/
ystar[2]=0.1;          /* 9.8;    0.0;   */
ystar[3]=0.01;         /*0.0;    -.014136; */
ystar[4]=0.0;

/*-----*/
/*-----rkdumb-----*/
/*-----*/

for(i=1;i<=HTASTEP;i++){
    data.out=HTAMIN+(float)(i-1)*
        (HTAMAX-(HTAMIN))/((float)(HTASTEP-1));
    rkdumb(ystar,data.dim,BEGIN,END,NPOINTS*KMAX,derivs);
    for(j=1; j<=data.dim;j++) ystar[j]=save[j];
    if(usernd == 1){
        if(model==0){
            ystar[1]=6.0*(1.0-2.0*ran1(&iseed));

```

```

ystar[2]=2.0*tpi*ran1(&iseed);
ystar[3]=6.0*(1.0-2.0*ran1(&iseed));
}
if(model==1){
ystar[1]=2.5*ran1(&iseed);
ystar[2]=4.0*tpi*ran1(&iseed);
ystar[3]=2.5*(1.0-2.0*ran1(&iseed));
}
/*printf("y1=%f y2=%f y3=%f", ystar[1], ystar[2], ystar[3]);*/
}
printf("Iteration # completed is now %d \n",i);

/*      if(i==1) break;      */
}

```

```

fclose(outfile);
free_vector(save,1,data.dim);
free_vector(ystar,1,data.dim);
free_matrix(stack,1,dimen,1,nstack+1);
}

```

```

#define IA 16807
#define IM 2147483647
#define AM (1.0/IM)
#define IQ 127773
#define IR 2836
#define NTAB 32
#define NDIV (1+(IM-1)/NTAB)
#define EPS 1.2e-7
#define RNMX (1.0-EPS)

```

```

float ran1(long *idum)
{
    int j;
    long k;
    static long iy=0;
    static long iv[NTAB];

```

```

float temp;

if (*idum <= 0 || !iy) {
    if (-(*idum) < 1) *idum=1;
    else *idum = -(*idum);
    for (j=NTAB+7;j>=0;j--) {
        k=(*idum)/IQ;
        *idum=IA*( *idum-k*IQ)-IR*k;
        if (*idum < 0) *idum += IM;
        if (j < NTAB) iv[j] = *idum;
    }
    iy=iv[0];
}
k=(*idum)/IQ;
*idum=IA*( *idum-k*IQ)-IR*k;
if (*idum < 0) *idum += IM;
j=iy/NDIV;
iy=iv[j];
iv[j] = *idum;
if ((temp=AM*iy) > RNMX) return RNMX;
else return temp;
}
#undef IA
#undef IM
#undef AM
#undef IQ
#undef IR
#undef NTAB
#undef NDIV
#undef EPS
#undef RNMX

```

```

void rkdummy(vstart,nvar,x1,x2,nstep,derivs)
int nvar,nstep;
float vstart[],x1,x2;
void (*derivs)();

```

```

{
    int i,k;
    float x,h,s;
    float *v,*vout,*dv,*vector();
    float wplus,wminus,amp,laste,amp1;
    void rk4(),nrerror(),free_vector();
    v=vector(1,nvar);
    vout=vector(1,nvar);
    dv=vector(1,nvar);
    for (i=1;i<=nvar;i++) {
        v[i]=vstart[i];
    }
    x=x1;
    h=(x2-x1)/nstep;
    for (k=1;k<=nstep;k++) {
        derivs(x,v,dv);
        rk4(v,dv,nvar,x,h,vout,derivs);
        if (x+h == x)
            nrerror("Step size too small in routine RKDUMB");
        x += h;
        s=(k+1)%KMAX;
        for (i=1;i<=nvar;i++) {
            v[i]=vout[i];
        }

        /* if(!s)
        fprintf(outfile,"%f %f %f %f\n",x,v[1],v[2],v[3]); */
    }
    for(i=1;i<=nvar;i++) save[i]=v[i];
    free_vector(dv,1,nvar);
    free_vector(vout,1,nvar);
    free_vector(v,1,nvar);
}

/*-----*/
/*-----rk4-----*/
/*-----*/

void rk4(y,dydx,n,x,h,yout,derivs)
float y[],dydx[],x,h,yout[];
int n;
void (*derivs)();
{

```

```

    int i;
    float xh,hh,h6,*dym,*dym,*dym,*dym,*vector();

    dym=vector(1,n);
    dym=vector(1,n);
    yt=vector(1,n);
    hh=h*0.5;
    h6=h/6.0;
    xh=x+hh;
    for (i=1;i<=n;i++) yt[i]=y[i]+hh*dydx[i];
    derivs(xh,yt,dym);
    for (i=1;i<=n;i++) yt[i]=y[i]+hh*dym[i];
    derivs(xh,yt,dym);
    for (i=1;i<=n;i++) {
        yt[i]=y[i]+h*dym[i];
        dym[i] += dym[i];
    }
    derivs(x+h,yt,dym);
    for (i=1;i<=n;i++)
        yout[i]=y[i]+h6*(dydx[i]+dym[i]+2.0*dym[i]);
    free_vector(yt,1,n);
    free_vector(dym,1,n);
    free_vector(dym,1,n);
}

/*-----*/
/*-----derivs-----*/
/*-----*/
void derivs(t,y,dy)
float t,y[],dy[];
{
    int i;
    float hta,eps,fix,zz,tpi,gain;
    i=write_stack(y);

    hta=data.out;
    eps=sqrt(tao/(2.0*pi));
    tpi=4.0*atan(1.0);
    gain=1.0/sqrt(1.0+Y*pi*(y[1]*y[1]-1.0));

    fix=stack[2][i]+y[2]-phipcm-2*delta*(t-taupi/2.0);

```

```

fix=fix-2.0*tpi*(float)(int)(fix/(2.0*tpi));
if(model==1){
    dy[1]=0.5*((2.0*y[3]+eps)*gain-eps)*y[1]+
           eps*hta*stack[1][i]*cos(fix);

    dy[2]= alfa*y[3]-eps*hta*(stack[1][i]/y[1])*sin(fix);

    dy[3]= (pi-(y[3]/eps)-pi*(1.0+(2.0*y[3]/eps))*
           gain*y[1]*y[1])/(2.0*pi);
    zz=(y[1]-1.0);
}
if(model==0){
    dy[1]=y[3]+hta*alfa*cos(fix)/sqrt(2*(pi/tao));
    dy[2]=y[3];
    dy[3]=-y[1]-(1+2*pi)*y[3]/sqrt(2*pi*tao);
    dy[4]=y[2];
    zz=y[1];
}

if(model==0){
if((t>=EXTIME)&&(lastde>=0.0)&&(dy[1]<=0.0)) fprintf(outfile,
"%f    %f    %f\n", data.out*alfa/(sqrt(2.0*pi/tao)), zz*alfa, t);
if((t>=EXTIME)&&(lastde<=0.0)&&(dy[1]>=0.0)) fprintf(outfile,
"%f    %f    %f\n", data.out*alfa/(sqrt(2.0*pi/tao)), zz*alfa, t);
fflush(outfile);
lastde=dy[1];
}

if(model==1){
if((t>=EXTIME)&&(lastde>=0.0)&&(dy[1]<=0.0)) fprintf(outfile,
"%f    %f    %f\n", data.out, zz, t);
if((t>=EXTIME)&&(lastde<=0.0)&&(dy[1]>=0.0)) fprintf(outfile,
"%f    %f    %f\n", data.out, zz, t);
fflush(outfile);
lastde=dy[1];
}

/*----Outputs phase-----*/
/*if((t>=EXTIME)&&(lastde>=0.0)&&(dy[2]<=0.0))

```

```

        fprintf(outfile,"%f  %f  %f\n",
                data.out*alfa/(sqrt(2*pi/tao)),y[2],t);
if((t>=EXTIME)&&(lastde<=0.0)&&(dy[2]>=0.0))
        fprintf(outfile,"%f  %f  %f\n",
                data.out*alfa/(sqrt(2*pi/tao)),y[2],t);
fflush(outfile);
lastde=dy[2]; */

return;
}
/*-----current-----*/

/*-----*/

int init_stack(t,step,dim)
float t,step;
int dim;
{
int i,j;
nstack=(int)(4.0*t/step);
stack=matrix(1,dim,1,nstack+1);

for(i=1;i<=dim;i++)
        for(j=1;j<=nstack;j++) stack[i][j]=0.0;
return nstack;
}

int write_stack(x)
float x[];
{
static int j=1;
stack[1][j]=x[1];
stack[2][j]=x[2];
if(j==nstack) j=0;
j++;
return j;
}

/*-----*/

void nrerror(error_text)

```

```

char error_text[50];
{
void exit();
printf("Numerical recipes run-time error...\n");
printf("%s\n",error_text);
printf("...now exiting to system  \n");
exit(1);
}

float *vector(nl,nh)
int nl,nh;

/* Allocates a float vector with range nl...nh */
{
float *v;
v=(float *)malloc((unsigned) (nh-nl+1)*sizeof(float));
if(!v) perror("allocation failure in vector()");
return v-nl;
}

void free_vector(v,nl,nh)
float *v;
int nl,nh;
/* Frees a float vector allocated by vector() */
{
free((char*) (v+nl));
}

float **matrix(nrl,nrh,ncl,nch)
int nrl,nrh,ncl,nch;
{
int i;
float **m;
/* Allocate pointers to rows */
m=(float **)malloc((unsigned) (nrh-nrl+1)*sizeof(float*));
if(!m) perror("Allocation failure 1 in matrix");
m-=nrl;
/* Allocate rows and set pointers to them */
for(i=nrl;i<=nrh;i++) {
m[i]=(float *)malloc((unsigned) (nch-ncl+1)*sizeof(float));
if(!m[i]) perror("allocation failure 2 in matrix");
m[i]-=ncl;
}
}

```

```

    }
    /* Return pointer to array of pointers to rows */
    return m;
}

void free_matrix(m,nrl,nrh,ncl,nch)
float **m;
int nrl,nrh,ncl,nch;
/* Frees a matrix allocated with matrix() */
{
int i;
for(i=nrh;i>=nrl;i--) free((char*) (m[i]+ncl));
free((char*) (m+nrl));
}
/*-----*/

```

### Appendix C. LKCON2.C Source Code

```
/*-----lkcon2.c-----*/
/*---Intergrates the conjugate Lang Kobayashi-----*/
/*--model of semiconductor equations. -----*/
/* including the effects of gain saturation */
/*--This is a code for delay-differential equations-----*/
/*---with the appropriate scalings perfomed-----*/
/*-----10 Aug 95-----*/
/*--- Original LICON.C program developed by */
/*-----Dr Gavrielides Phillips Laboratory */

/* ***** modified on 6 Dec 96 by Gordon T. Hengst */
/* constants moved to a config file so that the code does not */
/* have to be re-compiled for every constant change. */
/* modified on 22 April 97 to include the effects of gain */
/* saturation */

#include <math.h>
#include <stdio.h>
#include <malloc.h>

/*These #define statements are
replaced with variable statements */
/* #define BEGIN 0.0 */
/* #define END 500.0 */ /*2000.0 */
/* #define EXTIME 400.0 */ /*985.0*/
/* #define NPOINTS 32768 */
/* #define KMAX 1 */
/* #define HTAMIN .00018 */ /*.0017 */
/* #define HTAMAX .001 */ /*.0006 */
/* #define HTASTEP 100 */

/* #define inject .0006425 */
/* #define tao 1428.57 */
/* #define pi 2.33 */
/* #define alfa 4.0 */
/* #define taoex 1095.23 */ /*132.46*/
/* #define delta 0.0 */
/* +delta is injection below the slave frequency */
```

```

/* #define phipcm 0.0 */
/* #define model 1 */      /* model=0 phase equation */
                          /* model=1 full model */

float BEGIN, END, EXTIME;
int NPOINTS, KMAX;
float HTAMIN, HTAMAX;
int HTASTEP;
float inject, tao, pi, alfa, taoex, delta, phipcm, Y;
int model, usernd;

void rkdumb();
void rk4();
float *vector();
void free_vector();
void nrerror();
float **matrix();
void free_matrix();
int init_stack();
int write_stack();
float ran1();
void four1();

float **y=0,*xx=0;
float **stack,*save;
float lastde=0.0,taupi,time2,photon_life,
      carrier_life,ext_length,dir2;
FILE *outfile,*fourrf,*fourfm;
FILE *cfgfile;

int nstack,iseed=-872581,inti;
struct given {
    int dim;
    float out;
} data;

```

```

main(void)

{
void derivs();
void exit();
float *ystar;
register int i;
float h,tau,time,SCALE, tpi;
int dimen,j,n;

/*-----*/

fourrrf=fopen("fourrierrf.dat","wt");

if(fourrrf==NULL) {
    printf("fourrierrf.dat file has not been opened");
    exit (1);
}

fourrfm=fopen("fourrierfm.dat","wt");

if(fourrfm==NULL) {
    printf("fourrierfm.dat file has not been opened");
    exit (1);
}

/* *** Input default values from configuration file */

cfgfile = fopen("lkcon.cfg","r");
    /* open the config file for reading */
if (cfgfile == NULL){
    printf("LKCON.CFG file not found ... terminating \n");
    abort();
}

```

```

fscanf(cfgfile, "%f", &BEGIN);
fscanf(cfgfile, "%f", &END);
fscanf(cfgfile, "%f", &EXTIME);
fscanf(cfgfile, "%i", &NPOINTS);
fscanf(cfgfile, "%i", &KMAX);
fscanf(cfgfile, "%f", &HTAMIN);
fscanf(cfgfile, "%f", &HTAMAX);
fscanf(cfgfile, "%i", &HTASTEP);
fscanf(cfgfile, "%f", &inject);

/*fscanf(cfgfile, "%f", &tao); */

fscanf(cfgfile, "%f", &pi);
fscanf(cfgfile, "%f", &alfa);
fscanf(cfgfile, "%f", &ext_length);
fscanf(cfgfile, "%f", &delta);
fscanf(cfgfile, "%f", &phipcm);
fscanf(cfgfile, "%e", &photon_life);
fscanf(cfgfile, "%e", &carrier_life);
fscanf(cfgfile, "%i", &model);
fscanf(cfgfile, "%f", &Y);
fscanf(cfgfile, "%i", &usernd);

tao = carrier_life/photon_life;
taoex = (2*ext_length)/(3e10 * photon_life);

printf("\n BEGIN: %f",BEGIN );
printf("\n END: %f",END );
printf("\n EXTIME: %f",EXTIME );
printf("\n NPOINTS: %i",NPOINTS );
printf("\n KMAX: %i",KMAX );
printf("\n HTAMIN: %f", HTAMIN );
printf("\n HTAMAX: %f", HTAMAX);
printf("\n HTASTEP: %i",HTASTEP );
printf("\n inject: %f", inject);
printf("\n tao: %f",tao );
printf("\n pi: %f",pi );
printf("\n alfa: %f",alfa );
printf("\n taoex: %f",taoex );
printf("\n delta: %f",delta );
printf("\n phipcm: %f", phipcm);

```

```

printf("\n photon_life:  %e", photon_life);
printf("\n carrier_life:  %e", carrier_life);
printf("\n Y:  %f", Y);
printf("\n model:  %i", model);
printf("\n Random:  %i \n", usernd);

time2 = 1.0/photon_life;

if (NPOINTS == 0) {
  printf("Values not properly read into program ... terminating \n");
  abort();
}
outfile = fopen("lkcon.dat", "wt");

/*-----*/
data.dim=4;
if(model==0) tau=taoex*sqrt(2.0*pi/tao);
if(model==1) tau=taoex*sqrt(2.0*pi/tao);

printf("\n tau:  %f \n", tau);

dimen=4;
taupi=tau;
tpi=4.0*atan(1.0);
/*  However final printed time is in units of tp  */

/*-----*/

h=(END-BEGIN)/(NPOINTS*KMAX);
nstack=init_stack(tau,h,dimen);
ystar=vector(1,data.dim);
save=vector(1,data.dim);
xx=vector(1,NPOINTS+1);
y=matrix(1,data.dim,1,NPOINTS+1);

/*-----*/
/*-----initial conditions-----*/
/*-----*/
if(usernd ==0){
  /* use constant values */
  ystar[1]= 0.52667;      /*9.8;      .000645217;*/
  ystar[2]= 1.300658;   /* 9.8;      0.0;    */
}

```

```

ystar[3]= -0.265671;      /*0.0;      -.014136; */
ystar[4]=0.0;
    }
if(usernd ==1) {
ystar[1] = 2.5*ran1(&iseed);
    ystar[2] = 4.0*tpi*ran1(&iseed);
ystar[3] = 2.5*(1.0-2.0*ran1(&iseed));
}
/*-----*/
/*-----rkdumb-----*/
    data.out=inject;
    rkdumb(ystar,data.dim,BEGIN,END,NPOINTS*KMAX,derivs);
/*-----*/

/*--Use this part of code only to catch isolated solutions-----*/
/*
for(i=1;i<=HTASTEP;i++){
    data.out=HTAMIN+(float)(i-1)*
        (HTAMAX-(HTAMIN))/((float)(HTASTEP-1));

    inti=i;
    data.out=HTAMIN;
    ystar[1]=ran1(&iseed);
    ystar[2]=2.0*tpi*ran1(&iseed);
    ystar[3]=1.0-2.0*ran1(&iseed);
    printf("ys1=%f  ys2=%f  ys3=%f\n",
        ystar[1],ystar[2],ystar[3]);
    rkdumb(ystar,data.dim,BEGIN,END,NPOINTS*KMAX,derivs);
    save[2]=save[2]-2.0*tpi*(int)(save[2]/(2.0*tpi));
    for(j=1;j<=data.dim;j++) ystar[j]=save[j];
    ystar[1]=ran1(&iseed);
    ystar[2]=2.0*tpi*ran1(&iseed);
    ystar[3]=1.0-2.0*ran1(&iseed);
    printf("Iteration # completed is now %d\n",i);
    if(i==1) break;
}

*/
/*-----*/

if(model==0) SCALE=sqrt(tao/(2.0*pi));
if(model==1) SCALE=sqrt(tao/(2.0*pi));

for(i=1;i<=NPOINTS;i++)

```

```

        fprintf(outfile,"%f  %f  %f  %f\n",
                xx[i]*SCALE, y[1][i],y[2][i],y[3][i]);

time=(xx[1001]-xx[1000])*SCALE/time2;

/* ----- Fourier Transform of the Amplitude-----*/
free_vector(xx,1,NPOINTS+1);
xx=vector(1,2*NPOINTS+2);
if(model==1) {
    for (i=1;i<=2*NPOINTS-1;i=i+2) xx[i]=y[1][(i+1)/2];
    for(i=2;i<=2*NPOINTS;i=i+2) xx[i]=0.0;
}
if(model==0) {
    for (i=1;i<=2*NPOINTS-1;i=i+2) xx[i]=1.0+y[1][(i+1)/2];
    for(i=2;i<=2*NPOINTS;i=i+2) xx[i]=0.0;
}
four1(xx,NPOINTS,1);
for(i=NPOINTS+1;i<=2*NPOINTS-1;i=i+2) fprintf(fourrf,"%f  %f\n",
(float)(-(2*NPOINTS+1-i)/2)/((float)(NPOINTS)*time),
(xx[i]*xx[i]+xx[i+1]*xx[i+1])/((float)NPOINTS));
for(i=1;i<=NPOINTS-1;i=i+2) fprintf(fourrf,"%f  %f\n",
(float)((i-1)/2)/((float)(NPOINTS)*time),
(xx[i]*xx[i]+xx[i+1]*xx[i+1])/((float)NPOINTS));
fclose(fourrf);

/*---- Fourier Transform of the FM spectrum -----*/
if(model==1) {
    for(i=1;i<=2*NPOINTS-1;i=i+2)
        xx[i]=y[1][(i+1)/2]*cos(y[2][(i+1)/2]);
    for(i=2;i<=2*NPOINTS;i=i+2) xx[i]=y[1][i/2]*sin(y[2][i/2]);
}
if(model==0) {
    for(i=1;i<=2*NPOINTS-1;i=i+2)
        xx[i]=(1.0+y[1][(i+1)/2])*cos(y[2][(i+1)/2]);
    for(i=2;i<=2*NPOINTS;i=i+2) xx[i]=(1.0+y[1][i/2])*sin(y[2][i/2]);
}
four1(xx,NPOINTS,1);
for(i=NPOINTS+1;i<=2*NPOINTS-1;i=i+2)
    fprintf(fourfm,"%f  %f\n",
        (float)(-(2*NPOINTS+1-i)/2)/((float)(NPOINTS)*time),

```

```

        (xx[i]*xx[i]+xx[i+1]*xx[i+1])/((float)NPOINTS));
for(i=1;i<=NPOINTS-1;i=i+2) fprintf(fourfm,"%f  %f\n",
(float)((i-1)/2)/((float)(NPOINTS)*time),
        (xx[i]*xx[i]+xx[i+1]*xx[i+1])/((float)NPOINTS));
fclose(fourfm);

```

```

fclose(outfile);
free_vector(save,1,data.dim);
free_vector(ystar,1,data.dim);
free_matrix(stack,1,dimen,1,nstack+1);
}

```

```

#define SWAP(a,b)  tempr=(a) ; (a)=(b) ; (b)=tempr

```

```

void four1(data,nn,isign)
float data[];
int nn,isign;
{
int n,mmax,m,j,istep,i;
double wtemp,wr,wpr,wpi,wi,theta;
float tempr,tempi;
n=nn<<1;
j=1;
for(i=1;i<n;i+=2) {
    if(j>i) {
        SWAP(data[j],data[i]);
        SWAP(data[j+1],data[i+1]);
    }
    m=n>>1;
    while(m>=2 && j>m) {
        j-=m;
        m>>=1;
    }
    j+=m;
}
mmax=2;
while(n>mmax) {
    istep=2*mmax;
    theta=6.28318530717959/(isign*mmax);

```

```

wtemp=sin(0.5*theta);
wpr=-2.0*wtemp*wtemp;
wpi=sin(theta);
wr=1.0;
wi=0.0;
for(m=1;m<mmax;m+=2) {
    for(i=m;i<=n;i+=istep) {
        j=i+mmax;
        tempr=wr*data[j]-wi*data[j+1];
        tempi=wr*data[j+1]+wi*data[j];
        data[j]=data[i]-tempr;
        data[j+1]=data[i+1]-tempi;
        data[i]+=tempr;
        data[i+1]+=tempi;
    }
    wr=(wtemp=wr)*wpr-wi*wpi+wr;
    wi=wi*wpr+wtemp*wpi+wi;
}
mmax=istep;
}
}

```

```

#define IA 16807
#define IM 2147483647
#define AM (1.0/IM)
#define IQ 127773
#define IR 2836
#define NTAB 32
#define NDIV (1+(IM-1)/NTAB)
#define EPS 1.2e-7
#define RNMX (1.0-EPS)

```

```

float ran1(long *idum)
{
    int j;
    long k;
    static long iy=0;
    static long iv[NTAB];
    float temp;

```

```

    if (*idum <= 0 || !iy) {
        if (-(*idum) < 1) *idum=1;
        else *idum = -(*idum);
        for (j=NTAB+7;j>=0;j--) {
            k=(*idum)/IQ;
            *idum=IA*( *idum-k*IQ)-IR*k;
            if (*idum < 0) *idum += IM;
            if (j < NTAB) iv[j] = *idum;
        }
        iy=iv[0];
    }
    k=(*idum)/IQ;
    *idum=IA*( *idum-k*IQ)-IR*k;
    if (*idum < 0) *idum += IM;
    j=iy/NDIV;
    iy=iv[j];
    iv[j] = *idum;
    if ((temp=AM*iy) > RNMX) return RNMX;
    else return temp;
}
#undef IA
#undef IM
#undef AM
#undef IQ
#undef IR
#undef NTAB
#undef NDIV
#undef EPS
#undef RNMX

```

```

void rkdump(vstart,nvar,x1,x2,nstep,derivs)
int nvar,nstep;
float vstart[],x1,x2;
void (*derivs)();
{
    int i,k;

```

```

float x,h,s;
float *v,*vout,*dv,*vector();
float wplus,wminus,amp,laste,amp1;
void rk4(),nrerror(),free_vector();
v=vector(1,nvar);
vout=vector(1,nvar);
dv=vector(1,nvar);
for (i=1;i<=nvar;i++) {
    v[i]=vstart[i];
}
x=x1;
h=(x2-x1)/nstep;
for (k=1;k<=nstep;k++) {
    derivs(x,v,dv);
    rk4(v,dv,nvar,x,h,vout,derivs);
    if (x+h == x)
        nrerror("Step size too small in routine RKDUMB");
    x += h;
    s=(k+1)%KMAX;
    if(!s) xx[1+(k/KMAX)]=x;
    for (i=1;i<=nvar;i++) {
        v[i]=vout[i];
        if(!s) y[i][1+(k/KMAX)]=vout[i];
    }
/*    if(!s) fprintf(outfile,"%f %f %f %f\n",
        x,v[1],v[2],v[3]);
    if((!s)&&(x>EXTIME)) fprintf(outfile,"%d %f\n",
        inti,dir2);
    fflush(outfile);*/
}
for(i=1;i<=nvar;i++) save[i]=v[i];
free_vector(dv,1,nvar);
free_vector(vout,1,nvar);
free_vector(v,1,nvar);
}

/*-----*/
/*-----rk4-----*/
/*-----*/

void rk4(y,dydx,n,x,h,yout,derivs)
float y[],dydx[],x,h,yout[];

```

```

int n;
void (*derivs)();
{
    int i;
    float xh,hh,h6,*dym,*dym,*dym,*dym,*vector();

    dym=vector(1,n);
    dym=vector(1,n);
    yt=vector(1,n);
    hh=h*0.5;
    h6=h/6.0;
    xh=x+hh;
    for (i=1;i<=n;i++) yt[i]=y[i]+hh*dydx[i];
    derivs(xh,yt,dym);
    for (i=1;i<=n;i++) yt[i]=y[i]+hh*dym[i];
    derivs(xh,yt,dym);
    for (i=1;i<=n;i++) {
        yt[i]=y[i]+h*dym[i];
        dym[i] += dym[i];
    }
    derivs(x+h,yt,dym);
    for (i=1;i<=n;i++)
        yout[i]=y[i]+h6*(dydx[i]+dym[i]+2.0*dym[i]);
    free_vector(yt,1,n);
    free_vector(dym,1,n);
    free_vector(dym,1,n);
}

/*-----*/
/*-----derivs-----*/
/*-----*/
void derivs(t,y,dy)
float t,y[],dy[];
{
    int i;
    float hta,eps,fix,zz,tpi, gain;
    i=write_stack(y);

    hta=data.out;
    tpi=4.0*atan(1.0);
    eps=sqrt(tao/(2.0*pi));

```

```

gain=1.0/sqrt(1.0+Y*pi*(y[1]*y[1]-1.0));

fix=stack[2][i]+y[2]-hipcm-2*delta*(t-taupi/2.0);
fix=fix-2.0*tpi*(float)(int)(fix/(2.0*tpi));
if(model==1){
    dy[1]=0.5*((2.0*y[3]+eps)*gain-eps)*y[1]+
           eps*hta*stack[1][i]*cos(fix);

    dy[2]= alfa*y[3]-eps*hta*(stack[1][i]/y[1])*sin(fix);

    dy[3]= (pi-(y[3]/eps)-pi*(1.0+(2.0*y[3]/eps))*
            gain*y[1]*y[1])/(2.0*pi);
    zz=(y[1]-1.0);
}
if(model==0){
    fix=stack[2][i]+y[2]-hipcm-2*delta*(t-taupi/2.0);
    fix=fix-2.0*tpi*(float)(int)(fix/(2.0*tpi));
    dy[1]=y[3]+hta*alfa*cos(fix)/sqrt(2*pi/tao);
    dy[2]=y[3];
    dy[3]=-y[1]-(1+2*pi)*y[3]/sqrt(2*pi*tao);
    dy[4]=y[2];
    zz=y[1];
}
dir2=dy[2];

/*if((t>=EXTIME)&&(lastde>=0.0)&&(dy[1]<=0.0))
    fprintf(outfile,"%f  %f  %f\n",
            data.out*alfa/(sqrt(2*pi/tao)),zz,t);
if((t>=EXTIME)&&(lastde<=0.0)&&(dy[1]>=0.0))
    fprintf(outfile,"%f  %f  %f\n",
            data.out*alfa/(sqrt(2*pi/tao)),zz,t);
fflush(outfile); */

lastde=dy[1];

return;
}
/*-----current-----*/

/*-----*/

```

```

int init_stack(t,step,dim)
float t,step;
int dim;
{
int i,j;
nstack=(int)(4.0*t/step);
stack=matrix(1,dim,1,nstack+1);
for(i=1;i<=dim;i++)
    for(j=1;j<=nstack;j++) stack[i][j]=0.0;
return nstack;
}

int write_stack(x)
float x[];
{
static int j=1;
stack[1][j]=x[1];
stack[2][j]=x[2];
if(j==nstack) j=0;
j++;
return j;
}

/*-----*/

void nrerror(error_text)
char error_text[50];
{
void exit();
printf("Numerical recipes run-time error...\n");
printf("%s\n",error_text);
printf("...now exiting to system  \n");
exit(1);
}

float *vector(nl,nh)
int nl,nh;
/* Allocates a float vector with range nl...nh */
{
float *v;
v=(float *)malloc((unsigned) (nh-nl+1)*sizeof(float));

```

```

if(!v) nrerror("allocation failure in vector()");
return v-nl;
}

void free_vector(v,nl,nh)
float *v;
int nl,nh;
/* Frees a float vector allocated by vector() */
{
free((char*) (v+nl));
}

float **matrix(nrl,nrh,ncl,nch)
int nrl,nrh,ncl,nch;
{
int i;
float **m;
/* Allocate pointers to rows */
m=(float **)malloc((unsigned) (nrh-nrl+1)*sizeof(float*));
if(!m) nrerror("Allocation failure 1 in matrix");
m-=nrl;
/* Allocate rows and set pointers to them */
for(i=nrl;i<=nrh;i++) {
m[i]=(float *)malloc((unsigned) (nch-ncl+1)*sizeof(float));
if(!m[i]) nrerror("allocation failure 2 in matrix");
m[i]-=ncl;
}
/* Return pointer to array of pointers to rows */
return m;
}

void free_matrix(m,nrl,nrh,ncl,nch)
float **m;
int nrl,nrh,ncl,nch;
/* Frees a matrix allocated with matrix() */
{
int i;
for(i=nrh;i>=nrl;i--) free((char*) (m[i]+ncl));
free((char*) (m+nrl));
}
/*-----*/

```

## Bibliography

1. Agrawal, Govind P. "Line Narrowing in a Single-Mode Injection Laser Due to External Optical Feedback," *IEEE Journal of Quantum Electronics*, QE-20 (5): 468-471 (May 1984).
2. Agrawal, Govind P. and Jeffery T. Klaus. "Effect of Phase-Conjugate Feedback on Semiconductor Lasers," *Optics Letters*, 16(17): 1325-1327 (September 1991).
3. Alsing, P.M., V. Kovanis, A. Gavrielides, and T. Erneux. "Lang and Kobayashi Phase Equation," *Physical Review A*, 53 (5): 1-6 (May 1996).
4. Auyeung, John, D. Fekete, David Pepper and Amnon Yariv. "A Theoretical and Experimental Investigation of the Modes of Optical Resonators with Phase-Conjugate Mirrors," *IEEE Journal of Quantum Electronics*, QE-15 (10): 1180-1188 (October 1979).
5. Cronin-Golomb, Mark, Amnon Yariv, and Israel Ury. "Coherent Coupling of Diode Lasers by Phase Conjugation," *Applied Physics Letters*, 48 (19): 1240-1242 (May 1986).
6. Feinberg, Jack. "Self-Pumped, Continuous-Wave Phase Conjugation Using Internal Reflection," *Optics Letters*, 7 (10): 486-488 (October 1982).
7. Fisher, Robert A. *Optical Phase Conjugation*. Orlando, FL: Academic Press, Inc., 1983.
8. Garret, M. H., J. Y. Change, H. P. Jenssen, and C. Warde. "Self-Pumped Phase Conjugation and Four-Wave Mixing in 0°- and 45°-cut n-type BaTiO<sub>3</sub>:Co," *Optics Letters*, 18(6): 405-407 (March 1993).
9. Gavrielides, Athanasios. Nonlinear Optics Center, Phillips Laboratory, Kirtland AFB, NM. Personal Correspondence, 1996.
10. Gray, George R., David Huang, and Govind P. Agrawal. "Chaotic Dynamics of Semiconductor Lasers with Phase-Conjugate Feedback," *Physical Review A*, 49(3): 2096-2105 (March 1994).
11. Gray, George R., David H. KeTienne and Govind P. Agrawal. "Phase-Conjugate Feedback in Semiconductor Lasers," *SPIE*, 239: 713-722 (July 1995).
12. Hengst, Gordon T. "Nonlinear Interferometry: Optical Image Addition/Subtraction and Novelty Filters," MS Thesis, AFIT/GEO/ENP/90D-2. School of Engineering, Air Force Institute of Technology (AU), Wright-Patterson AFB OH, December 1990.
13. Hilborn, Robert C. *Chaos and Nonlinear Dynamics*. New York: Oxford University Press, Inc., 1994.

14. Kovanis, V., A. Gavrielides, T. B. Simpson, and J. M. Liu. "Instabilities and Chaos in Optically Injected Semiconductor Lasers," *Applied Physics Letters*, 67(19):2780-2782 (November 6, 1995).
15. Langley, L. N., K. A. Shore, and J. Mork. "Dynamical and Noise Properties of Laser Diodes Subject to Strong Optical Feedback," *Optics Letters*, 19(24):2137-2139 (December 15, 1994).
16. Liby, Bruce W. and David Statman. "Phase Delay in Phase-Conjugate External Cavity Lasers," *Optics Communications*, 101 (1): 79-84 (August 1993).
17. Liby, Bruce W. and David Statman. "Controlling the Linewidth of a Semiconductor Laser with Photorefractive Phase Conjugate Feedback," *IEEE Transactions on Quantum Electronics*, 32(5):835-838 (May 1996).
18. Li, Hua, Jun Ye, and John G. McInerney. "Detailed Analysis of Coherence Collapse in Semiconductor Lasers," *IEEE Journal of Quantum Electronics*, 29(9):2421-2432 (September 1993).
19. Moon, Francis C. *Chaotic and Fractal Dynamics*. New York: John Wiley & Sons, Inc., 1992.
20. Mork, Jesper, Bjarne Tromborg and Jannik Mark. "Chaos in Semiconductor Lasers with Optical Feedback: Theory and Experiment," *IEEE Journal of Quantum Electronics*, 28(1):93-108 (January 1992).
21. "Chaos-based Lasers May Yield Secure Communications," *Machine Design*,: 20 (July 1995).
22. Ritter, Alfred and Hartmut Haug. "Theory of Laser Diodes with Weak Optical Feedback I," *Journal of the Optical Society of America - B*, 10 (1):130-144 (January 1993).
23. Ritter, Alfred and Hartmut Haug. "Theory of Laser Diodes with Weak Optical Feedback II," *Journal of the Optical Society of America - B*, 10 (1):145-154 (January 1993).
24. Simpson, T. B., J. M. Liu, A. Gavrielides, V. Kovanis, and P. M. Alsing. "Period-Doubling Cascades and Chaos in a Semiconductor Laser with Optical Injection," *Physical Review A*, 51 (5):4181-4185 (May 1995).
25. Vahala, Kerry, Kazuo Kyuma, Amnon Yariv, Sze-Keung Kwong, Mark Cronin-Golomb, and Kam Y. Lau. "Narrow Linewidth, Single Frequency Semiconductor Laser with a Phase Conjugate External Cavity Mirror," *Applied Physics Letters*, 49(23):1563-1565 (December 8, 1986).
26. van Tartwijk, G. H. M., H. J. C. van der Linden, and D. Lenstra. "Theory of a Diode Laser with Phase-Conjugate Feedback," *Optics Letters*, 17(22): 1590-1592 (November 15, 1992).
27. van Tartwijk, G. H. M., and D. Lenstra. "Semiconductor Lasers with Optical Injection and Feedback," *Quantum Semiclassical Optics*, 7: 87-143 (1995).

28. Weiss, Chimon, Shmuel Sternklar, and Baruch Fischer. "Double Phase-Conjugate Mirror: Analysis, Demonstration, and Applications," *Optics Letters*, 12(2): 114-116 (February 1987).
29. Yamada, M. "Transverse and Longitudinal Mode Control in Semiconductor Injection Lasers," *IEEE Journal of Quantum Electronics*, 19: 1365-1380 (1983).
30. Ye, Jun, Hua Li and John McInerney. "Period-doubling Route to Chaos in a Semiconductor Laser with Weak Optical Feedback," *Physical Review A*, 47 (3): 2249-2252 (March 1993).
31. Yeh, Pochi. *Introduction to Photorefractive Nonlinear Optics*. New York: John Wiley & Sons, Inc., 1993.

## *Vita*

Major Gordon T. Hengst [REDACTED]

[REDACTED] graduated from Central Dauphin High School in 1981, and attended The Pennsylvania State University, graduating in 1985, with a Bachelor of Science in Electrical Engineering. He began active duty in the U. S. Air Force the same year, serving as an avionics engineer for the Avionics Laboratory, Wright-Patterson AFB, OH. In 1990, he received a Master of Science in Electrical Engineering from the Air Force Institute of Technology, specializing in nonlinear optics and phase conjugation. After graduation he was assigned to the Flight Test Branch, Phillips Laboratory, where he served as a flight test engineer and mission test director on-board the highly modified EC-135 Argus test aircraft. As a flight test engineer, Maj Hengst was responsible for transitioning laboratory atmospheric scintillation tests into flyable experiments for high altitude laser propagation tests. In 1994, he entered into the doctoral program at the Air Force Institute of Technology to study nonlinear laser physics.

REPORT DOCUMENTATION PAGE			Form Approved OMB No. 0704-0188	
Public reporting burden for this collection of information is estimated to average 1 hour per response, including the time for reviewing instructions, searching existing data sources, gathering and maintaining the data needed, and completing and reviewing the collection of information. Send comments regarding this burden estimate or any other aspect of this collection of information, including suggestions for reducing this burden, to Washington Headquarters Services, Directorate for Information Operations and Reports, 1215 Jefferson Davis Highway, Suite 1204, Arlington, VA 22202-4302, and to the Office of Management and Budget, Paperwork Reduction Project (0704-0188), Washington, DC 20503.				
1. AGENCY USE ONLY (Leave blank)	2. REPORT DATE August 97	3. REPORT TYPE AND DATES COVERED Doctoral Dissertation		
4. TITLE AND SUBTITLE Experimental Investigation of Nonlinear Dynamics in Single Mode Semiconductor Laser Diodes with Phase Conjugate Feedback			5. FUNDING NUMBERS	
6. AUTHOR(S) Gordon T. Hengst, Maj, USAF				
7. PERFORMING ORGANIZATION NAME(S) AND ADDRESS(ES) Air Force Institute of Technology, WPAFB OH 45433-6583			8. PERFORMING ORGANIZATION REPORT NUMBER  AFIT/DS/ENP/97-07	
9. SPONSORING/MONITORING AGENCY NAME(S) AND ADDRESS(ES) Phillips Laboratory (PL/LIDD) 3550 Aberdeen Ave Kirtland AFB, NM 87117-5776 Attn: Dr Gavrielides			10. SPONSORING/MONITORING AGENCY REPORT NUMBER	
11. SUPPLEMENTARY NOTES				
12a. DISTRIBUTION AVAILABILITY STATEMENT Approved for public release; distribution unlimited			12b. DISTRIBUTION CODE  A	
13. ABSTRACT (Maximum 200 words) The semiconductor laser diode offers a unique system to investigate nonlinear dynamics when optical feedback is applied. Although there is extensive research of laser diodes with optical feedback from normal dielectric mirrors, very little has been done experimentally to analyze the effects of degenerate phase conjugate feedback from a BaTiO3 crystal. This research experimentally investigated the dynamics of a single-mode laser diode with weak phase conjugate feedback using both the self-pumped and double phase conjugate geometries. The experimental results validated a mathematical model which numerically evaluates the Lang-Kobayashi coupled differential equations. The model simulated the nonlinear behavior of a laser diode subject to phase conjugate feedback and produced simulated RF and Fabry-Perot spectra of the laser output. Model and experimental results showed frequency locking between the relaxation oscillation and external cavity frequencies and changes in the relaxation oscillation as a function of cavity length. Resonant behavior in the feedback strength necessary to undamp the relaxation oscillation frequency as a function of the cavity length was also captured experimentally and numerically. Validation of the model and experimental results presented in this research significantly contribute to the understanding of the nonlinear behavior of a laser diode subject to optical feedback.				
14. SUBJECT TERMS Nonlinear dynamics, chaos, phase conjugate feedback, laser diode, fold bifurcation, hopf bifurcation			15. NUMBER OF PAGES 156	
			16. PRICE CODE	
17. SECURITY CLASSIFICATION OF REPORT Unclassified	18. SECURITY CLASSIFICATION OF THIS PAGE Unclassified	19. SECURITY CLASSIFICATION OF ABSTRACT Unclassified	20. LIMITATION OF ABSTRACT UL	